MONOCLONAL ANTIBODY KILLS HUMAN PLURIPOTENT STEM CELLS BY ONCOSIS VIA EXCESS REACTIVE OXYGEN SPECIES PRODUCTION

ZHENG JIYUN

(B.Eng. (Hons.), NUS)

A THESIS SUBMITTED

FOR THE DEGREE OF DOCTOR OF PHILOSOPHY

NUS GRADUATE SCHOOL FOR INTEGRATIVE SCIENCES AND ENGINEERING

NATIONAL UNIVERSITY OF SINGAPORE

2015

DECLARATION

I hereby declare that this thesis is my original work and it has been written by me in its entirety. I have duly acknowledged all the sources of information which have been used in the thesis.

This thesis has also not been submitted for any degree in any university previously.

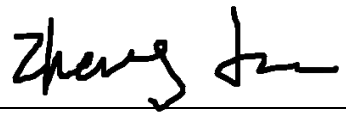

Zheng Jiyun

31 July 2015

ACKNOWLEDGEMENTS

I wish to express my sincere thanks to all people who have supported me in the past four years. First of all, I give my deepest appreciation to my supervisor, Dr. Andre Choo, who has continually and timely guided me throughout my Ph.D. study with patience, motivation and immense knowledge. I could not have imagined having a better mentor for my Ph.D. study. I thank my supervisor, Prof. Paul Matsudaira, for his insightful comments and encouragement, for offering me allowance to attend conference, and for his critical questions which incented me to widen my research from various perspectives.

Besides my supervisors, I would like to thank my TAC chair, Dr. Evelyn Yim, for providing me expertise in the research and the opportunity to do undergraduate teaching. I thank my fellow lab mates for the enlightening discussions and timely support on experiments. I thank my lunch mates for their patient waiting and packing lunch for me, and for all the fun we have had in the past four years.

I am grateful to the Bioprocessing Technology Institute (BTI) and NUS Centre for BioImaging Science (CBIS) for providing me with all the research facilities and materials, to NUS Graduate School for Integrative Science and Engineering (NGS) for providing me the scholarship and education allowance. Without their precious support, it would not be possible to conduct this research.

Last but not the least, I would like to thank my dearest family: my grandma, my parents, and my husband, for supporting me spiritually throughout writing this thesis and all aspects of my life in general.

TABLE OF CONTENTS

SUMMARY

Human pluripotent stem cells (hPSC), including human embryonic stem cells (hESC) and human induced pluripotent stem cells (hiPSC), have the ability to self-renew and under appropriate conditions differentiate into all three germ layers. The potential use of hPSC for regenerative medicine has been promising because of successful *in vitro* differentiation to lineage-specific cell types and more recently, approval for clinical trials. However, a major concern is the risk of teratoma formation from residual hPSC. Several strategies have been reported to eliminate residual hPSC, including cell sorting using specific antibodies, transgenic fluorescent markers, and physical properties such as cell adherence or density gradient centrifugation; and retrospective approaches with genetic manipulation like gene interference or introduction of "suicide gene". However, none is capable of completely precluding residual hPSC. Our group previously reported the first hESC-specific cytotoxic monoclonal antibody (mAb), mAb84. Subsequently, others reported the use of cytotoxic small molecules inhibiting oleate synthesis or anti-apoptotic factors. However, these small molecules may have non-specific effects on differentiated cell. More recently, we identified another hESC-specific cytotoxic mAb, TAG-A1 (A1). A1 is cytotoxic to hPSC but not differentiated cells and its cytotoxicity and killing kinetics on hPSC is comparable to mAb84. However, unlike mAb84 which is an IgM, A1 is an IgG and thus have better penetration efficiency into embryoid bodies (EB). Additional characterization revealed that A1 kills hPSC within 5 minutes in a dosage-dependent manner and must be minimally bivalent to exert its effect. A1 binds to an O-linked glycan epitope present on multiple antigens on hPSC with a saturation density of ~3 x

10^7 A1 molecules per hESC. In SCID mouse models, treatment of hESC *in vitro* or *in vivo* with A1 prevented/delayed teratoma formation up to 10 weeks post-injection unlike non-treated mice which formed grade 3 teratomas by week 6. Moreover, *in vitro* treatment with $F(ab)_2$_A1 also prevented/delayed teratoma formation, suggesting that killing is independent of the Fc region.

Mechanistically, A1 kills hPSC via oncosis and not apoptosis. Hallmarks of oncosis include rapid killing rate, cell and mitochondria swelling, and severe plasma membrane damage. By scanning electron microscopy, membrane pores were observed following A1 treatment and A1 was predominantly localised on fused debris of microvilli and damaged plasma membrane. Hence, we proposed that A1 kills via receptor dimerization-initiated signalling pathway where the microvilli are likely the signal initiating sites.

In addition, A1-treated hPSC exhibited microvilli degradation, homotypic adhesion, and actin re-organization. More importantly, excess reactive oxygen species (ROS), specifically superoxide, was produced upon A1 treatment and critical for inducing hPSC death. The source of ROS was nicotinamide adenine dinucleotide phosphate (NADPH) oxidase, most likely Nox2 isoform and this occurs downstream of microvilli degradation and homotypic adhesion, but upstream of massive actin re-organization, mitochondria impairment and plasma membrane damage. Taken together, we presented A1 as an effective tool to increase the safety of hPSC-based therapy and proposed for the first time a mechanistic model of antibody-induced oncosis on hESC revealing a previously unrecognized role for NADPH oxidase-derived ROS in mediating oncotic hESC death.

LIST OF TABLES

LIST OF FIGURES

LIST OF ABBREVIATIONS

hPSC	Human pluripotent stem cells
hESC	Human embryonic stem cells
hiPSC	Human induced pluripotent stem cells
EB	Embryoid bodies
RPE	Retinal pigment epithelium
mAb	Monoclonal antibody
SCID	Severe combined immunodeficient
A1	mAb TAG-A1
IgM	Immunoglobulin M
IgG	Immunoglobulin G
Fc	Fragment, crystallisable
ADCC	Antibody-dependent cell-mediated cytotoxicity
CDC	Complement-dependent cytotoxicity
Fab	Fragment antigen-binding
FGF-2	Fibroblast growth factor-2
PD	Parkinson's disease
FDA	Food and Drug Administration
SCD1	Stearoyl-coA desaturase
FAC	Fluorescence-activated cell sorting
MAC	Magnetic-activated cell sorting
SSEA-5	Stage-specific embryonic antigen-5
RA	Retinoic acid
PODXL	Podocalyxin
TK	Thymidine kinase
HPC	Hematopoietic progenitor cells
TNF	Tumor necrosis factor
FADD	Fas associated death domain
Apaf-1	Apoptosis protease activating factor
SEM	Scanning electron microscopy
TEM	Transmission electron microscopy
TUNEL	Terminal deoxynucleotidyl transferase mediated dUTP Nick End Labelling
PI	Propidium iodide
EGFR	Epidermal growth factor receptor
SHH	Sonic hedgehog
SCCHN	Squamous cell carcinoma of the head and neck
MAP	Mitogen activated protein
APO-1	Apoptosis antigen 1
NGcGM3	N-glycolyl GM3 ganglioside
HA	Homotypic adhesion
CM	Conditioned media
KO	Knockout

NEAA	Nonessential amino acids
FBS	Fetal bovine serum
ELISA	Enzyme-Linked ImmunoSorbent Assay
OPD	o-phenylenediamine dihydrochloride
DPI	Diphenyleneiodonium chloride
APO	Acetovanillone or Apocynin
MPA	Mycophenolic acid
HE	Dihydroethidium
IP	Immuno-precipitation
HAT	hypoxanthine-aminopterin-thymidine
ESIMR90	human fetal lung fibroblasts-derived iPS cells
MS	Mass spectrometry
ConA	Concanavalin A
B-GalNac	Benzyl-α-GalNac
LNFP1	Lacto-N-fucopentaose I
H1	Type-1 H
H2	Type-2 H
bgA	Type-1 A
bgB	Type-1 B
UV	Ultra-violet
SEM	Standard error of mean
OGT	O-GlcNAc
CDR	Complementarity determining regions
qRT-PCR	Quantitative real-time PCR
HSV	Herpes simplex virus
IM	Intramuscular
IV	Intravenous
FcRn	Neonatal Fc receptor
SOD	Superoxide dismutase
GEF	Guanine nucleotide exchange factor
GPCR	G-protein coupled receptor
RTK	Receptor tyrosine kinase
LMP	Lysosome membrane permeabilization
ROS	Reactive oxygen species
O^{2-}	Superoxide
NADPH	Nicotinamide adenine dinucleotide phosphate

1 CHAPTER 1 INTRODUCTION

1.1 Background

Human pluripotent stem cells (hPSC), namely human embryonic stem cells (hESC) and human induced-pluripotent stem cells (hiPSC), are characterized by their unique abilities to replicate indefinitely (self-renewal) and under the appropriate conditions differentiate into derivatives of all three germ layers (pluripotency)[1,2]. Mounting studies have reported the successful differentiation of hPSC into embryoid bodies (EB)[3] and several lineage-specific cell types, such as cardiomyocytes[4–6], hepatocytes[7–9], neurons[10–12], renal lineage[13], endothelial cells[14–19], osteoblasts[20,21], keratinocytes[22], and retinal pigment epithelium (RPE)[23,24]. Their successes demonstrate the great potential of hPSC in tissue engineering and regenerative medicine to treat various diseases such as diabetes, heart failure, Parkinson's disease, degenerative eye diseases, and skeletal tissue injuries. Since 2009, several clinical trials have been approved to transplant hESC-derived oligodendrocytes, RPE, or beta cells for the treatment of spinal cord-injured patients[25], Stargardt's Macular Dystrophy and Dry Age-Related Macular Degeneration[26], severe myopia[27] or diabetes[28], respectively. However, formation of teratomas or teratocarcinomas due to residual undifferentiated hPSC remains a major safety concern and can potentially impede the progress of hPSC-based therapies[29–31].

Previously, our group was the first to demonstrate the successful use of hESC-specific cytotoxic monoclonal antibody (mAb), mAb84, in preventing teratoma formation in severe combined immunodeficient (SCID) mice[32]. However, since mAb84 is an IgM pentamer, its relatively large molecule size

may impede its penetration efficiency into tumour mass. Subsequently, the variable genes of mAb84 was cloned and reformatted as a single-chain Fv dimer, scFv84-HTH. The recombinant scFv84-HTH retained the binding properties of mAb84 but more importantly had improved penetration[33]. However, to achieve the same level of cytotoxicity on hESC, the amount of scFv84-HTH required is 20 times more than mAb84. Nevertheless, since mAb84 and scFv84-HTH are either multivalent or bivalent, the author speculated that antibody cytotoxicity is associated with its valency. Interestingly, from a subsequent panel of mAbs raised against hESC, another hESC-specific cytotoxic antibody, mAb TAG-A1 (A1), was discovered by our group. Unlike mAb84, A1 is an IgG monomer hence the penetration issue may be alleviated.

Antibody-induced cell death has been widely used to eliminate undesired cells. Antibodies can induce cell death via various routes, including antibody-dependent cell-mediated cytotoxicity (ADCC), complement-dependent cytotoxicity (CDC), and direct cell death via apoptosis or oncosis. Previously, our group has demonstrated that mAb84 kills hESC via oncosis[34]. However, unlike ADCC, CDC, and apoptosis, the understanding about antibody-induced cell oncosis is limited.

1.2 Thesis objectives

As we discussed, A1 is potentially a better alternative to mAb84 in eliminating tumorigenicity for hPSC-based therapy especially if the differentiated cells are in an aggregated state. A1 was generated as part of the antibody discovery platform in BTI. My project aimed to characterize A1, benchmark it to mAb84 and investigate the mechanism of action for A1-induced cell death, so that to

facilitate the effective use of A1 in hPSC-based transplantation and to understand the regulation of hPSC death. Hence, there are three objectives for this thesis:

(1) *In vitro* characterization of A1

(2) *In vivo* characterization of A1

(3) Elucidation of A1-induced hESC death mechanism

1.2.1 *In vitro* characterization of A1

First, the specificity of A1 cytotoxicity will be determined against undifferentiated hESC, hiPSC and spontaneously differentiated hESC. Next, studies will be carried out to identify the antigen target of A1 on hESC. Many antigens on the cell surface are glycoproteins; hence the characterisation will include both the core proteins and post-translational modifications, namely O-glycosylation and N-glycosylation. Subsequently, A1 will be benchmarked to mAb84 in terms of amino acid sequences in variable regions, competitive binding on hESC, penetration efficiency into EB, dosage efficiency, and killing kinetics. We will also exam the stoichiometry between A1 and hESC, as well as the association between A1 cytotoxicity, bivalency and the Fc-domain.

1.2.2 *In vivo* characterization of A1

The ultimate goal of cytotoxic A1 is to eliminate residual undifferentiated hPSC from differentiated cells and therefore prevent teratoma formation. Hence this chapter will investigate whether A1 can prevent teratoma formation in SCID mouse models following *in vitro* or *in vivo* treatment of hESC with A1.

1.2.3 Elucidation of A1-induced hESC death mechanism

First, the mode of A1-induced hESC death, namely oncosis or apoptosis, will be determined by examining the features of A1 killing, via apoptosis assay and morphological observations under confocal microscopy, scanning electron microscopy and transmission electron microscopy. Subsequently, functional studies will be carried out to identify events that occur in A1-induced hESC death. Last but not the least, a mechanistic model of A1-induced hESC death will be proposed with the key mediator of the cell death pathway and delineated order of observed events.

1.3 Thesis organization

This thesis consists of seven chapters.

Chapter 1 describes the background and objectives of this research.

Chapter 2 is relevant literature review which covers (1) the potential of hPSC-based therapies and the major safety concern: teratoma formation; (2) current methods to prevent teratoma formation; (3) applications of cytotoxic antibody-induced cell death; (4) phases and modes of cell death, and (5) studies on cytotoxic antibody-induced cell death.

Chapter 3 provides the detailed materials and methods of this research.

Chapter 4 presents results on the *in vitro* characterization of A1.

Chapter 5 presents results on the *in vivo* characterization of A1.

Chapter 6 elucidates the mechanism of A1-induced hESC death.

Chapter 7 summaries the results of this research and discuss the direction of future works.

2 CHAPTER 2 LITERATURE REVIEW

2.1 Origin of human pluripotent stem cells (hPSC)

Human embryonic stem cells (hESC) and human-induced pluripotent stem cell (hiPSC) are the two sources of human pluripotent stem cells (hPSC). Human ESC are derived from the inner cell mass of an early stage human embryo[1]. They are pluripotent stem cells with unique abilities to replicate indefinitely (self-renewal) and under the appropriate conditions differentiate into derivatives of all three germ layers (pluripotency) (Figure 2-1). Thus, hESC can potentially be the single source of cells to provide replacement for the lost to damage or disease.

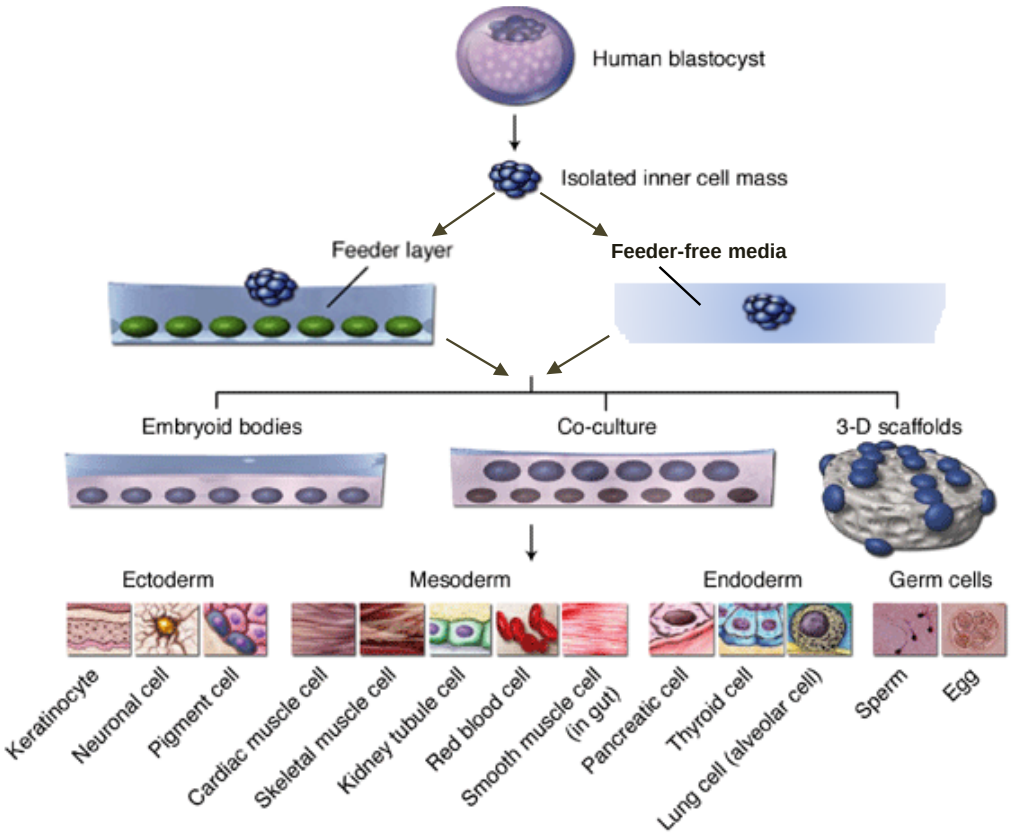

Figure 2-1: Derivation of a hESC line, and differentiation into various cell types[35].
An embryonic stem cell line is derived from the inner cell mass of an early-stage human blastocyst and cultured in the presence of feeder cells or in feeder-free media, which can be differentiated into cell types of all three germ layers and germ cells by using methods such as embryoid body formation, co-culture with somatic cells, and culture in three-dimensional scaffolds.

In 2007, an alternative source of hPSC, human induced-pluripotent stem cells (hiPSC) were generated by reprogramming human dermal fibroblasts with transient over-expression of four transcription factors: Oct3/4, Sox2, Klf4, and c-Myc[2]. Reprogramed cells have the ability to differentiate into derivatives of the three germ layers *in vitro* and in teratomas, and are similar to hESC in morphology, proliferation, surface antigens, gene expression, epigenetic status of pluripotent cell-specific genes, and telomerase activity[2,36].

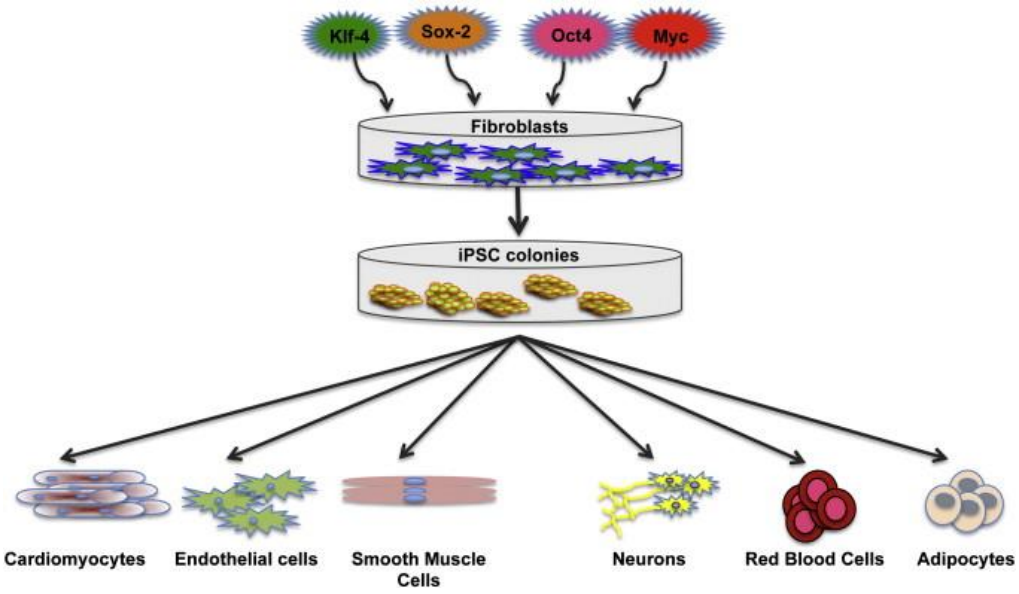

Figure 2-2: Reprogrammed hiPSC from differentiated somatic cells[37].
Human induced pluripotent stem cells (hiPSC) can be reprogrammed from differentiated somatic cells (fibroblasts) with retroviral over-expression of the four factors Oct4, Sox2, Klf4 and c-Myc, and potentially differentiate into all somatic cell types.

The generation of hiPSC might alleviate two concerns of hESC usage: immunogenicity upon transplantation[38] and ethical controversy in the destruction of human embryos for medical research[39]. However, to use hiPSC in humans, safety concerns regarding the usage of viruses for reprogramming and expression of oncogenes should be addressed.

2.2 Applications of human pluripotent stem cells

Differentiating hPSC into various types of lineage-specific derivatives for cell replacement therapies has attracted substantial interest from the scientific community over the last decade. The first success was reported about a decade ago for hESC-derived cardiomyocyte lineage. With improved differentiation protocols, a recent study demonstrated that hESC-derived cardiomyocytes can be produced at a clinical scale, cryopreserved with good viability and delivered via intra-myocardial to regenerate non-human primate hearts[6]. Their success holds a great promise for the treatment of human heart failure. Another promising hPSC-derived lineage is dopamine-producing neurons for the treatment of Parkinson's disease (PD). Recently, a preclinical assessment of hESC-derived midbrain dopamine neurons in a rat PD model showed long-term survival with functionality restoring long-distance, target-specific neurotransmission in the host brain, comparable to fetal neurons[10]. In another study, transplantation of autologous hiPSC-derived dopamine neurons provided functional recovery of motor deficits for at least 2 years in a non-human primate model[11]. These animal models provide a strong support for the clinical translation of hPSC-derived neurons. Researchers have also been seeking solutions from hPSC-based renal regeneration to overcome the prevalence of end-stage renal disease because there are no postnatal stem cells to replace lost nephrons. *In vitro* formation of a self-organizing kidney with nephron formation was recently achieved by directed differentiation of hESC under a fully chemically-defined monolayer culture condition[13].

On the other hand, hESC- or hiPSC-derived hepatocyte-like cells are predominantly used in the field of toxicology for drug discovery and

cytotoxicity screening in the early phase of pharmaceutical development[40]. For example, hiPSC-derived hepatocyte-like cells was used to host an *in vitro* assay of liver-stage malaria infection to allow the assessment of donor-specific drug response[8]. Current challenge is to control the maturity of hepatocytes while maintaining functional and stable hepatic functions, including high activity levels of the cytochrome P450 enzymes[9].

Encouragingly, several hPSC-derived lineages have been approved for clinical trials by the US Food and Drug Administration (FDA). In 2009, the first clinical trial of hPSC was approved for the transplantation of hESC-derived oligodendrocytes into spinal cord-injured patients[25]. With the observation of microscopic cysts, this trial was placed on clinical hold due to safety concern of teratoma formation. In 2013, Asterias bought over this project and the first interim result in Aug 2015 showed that the first patient has progressed well in the injury treatment and two other patients have been successfully dosed with the same stem cells[41,42]. With the publication of initial safety data, Asterias plans to expand the enrolment from 13 patients up to 40 patients in the Phase 1/2a clinical trial. Another two clinical trials involving hESC-derived retinal pigment epithelial (RPE) cells were approved in 2010 to establish the safety and tolerability of sub-retinal transplantation for the treatment of Stargardt's Macular Dystrophy and Dry Age-Related Macular Degeneration[26]. Preliminary results were promising as no signs of hyper-proliferation, tumorigenicity, ectopic tissue formation, or apparent rejection were observed after 4 months[43]. Subsequently, in 2013, transplantation of hESC-derived RPE cells for the treatment of severe myopia was approved for phase I/II clinical trials[27]. Most recently, a phase I clinical trial initiated by Viacyte using hESC-

derived beta cells delivered in immune-protective capsules was approved for the treatment of diabetes[28].

2.3 Tumorigenicity: the major safety concern of hPSC-based therapies

In any hPSC-based therapies, hPSC need to be differentiated into the desired lineage-specific derivatives under a controlled environment. However, since the differentiation is not 100% efficient, there are usually undifferentiated or partially differentiated hPSC remaining in the differentiated cell products, which poses the risk of tumorigenicity. Over the last decade, two prominent safety hurdles of hESC-based therapies are immunogenicity and tumorigenicity[29]. Progressively, immunogenicity of hESC can almost be resolved by one or combinations of methods, such as transplanting cells into immune-privileged sites, generating patient-specific hESC, producing HLA isotypes-matched hESC-line banks, and the use of autologous derivatives from hiPSC[31,38]. However, strategies to solve the tumorigenicity of hPSC remain elusive.

Briefly, tumorigenicity of hPSC refers to either the formation of teratomas (benign tumours) or teratocarcinomas (malignant tumours) in the differentiated cell products due to the presence of residual undifferentiated hPSC. Currently, *in vivo* teratoma formation is considered as the most definitive assay to evaluate hPSC pluripotency and determine the tumorigenicity of their therapeutic derivatives[44]. The purity of differentiated cell products is not trivial. A titration experiment of undifferentiated hPSC in severe combined Immunodeficient (SCID) mice demonstrated that as few as 2 colonies of undifferentiated hPSC or less than 250 single-cell undifferentiated hPSC could lead to teratoma formation[45].

Numerous studies have demonstrated the formation of teratomas[45–48] or teratocarcinomas[49–52] in SCID mice due to residual undifferentiated hESC after transplantation. The first report described engraftment of hESC-derived neural precursor cells into the sub-retinal space where formation of severe intraocular teratomas was observed after long-term survival[46]. Another study involving the transplantation of hESC-derived insulin expressing cells into mice also resulted in the failure of treatment for Type I diabetes due to teratoma formation[47]. Though teratomas are benign tumours, they can still exert a mass effect and transform to teratocarcinomas[53]. Teratocarcinomas are usually characterized as containing both undifferentiated malignant embryonal carcinoma cells and somatic tissues[50]. Formation of malignant germ cell–like tumours was reported in a study on *in vivo* differentiation of partially reprogrammed hiPSC in SCID mice[52]. Another study showed that hESC are prone to generate primitive, undifferentiated teratocarcinomas, instead of teratomas, in engrafted human fetal tissues, namely thymus, lung and pancreas, in SCID mice[49]. These observations raise urgent safety concerns about the therapeutic applications of hPSC.

2.4 Solutions: methods to prevent tumorigenicity of hPSC

Methods to eliminate residual hPSC fall into two categories: negative or positive cell sorting based on specific antibodies[54], transgenic fluorescent markers[55,56], or physical properties[57]; or genetic manipulation by gene interference[58] or introduction of "suicide gene"[59,60]. These methods are applied in three different stages[29,31]. First, in the pre-transplantation stage, hPSC can either be terminally differentiated into the desired cell types or undifferentiated cells can be removed from differentiated cells products by

various sorting techniques. Second, in the early post-transplantation stage, tumour progression can be interrupted with methods such as genetic manipulation or cytotoxic drugs. Third, in the late post-transplantation stage, detected tumours carrying an engineered "suicide gene" can be eliminated by drugs. Various methods to eliminate undifferentiated hPSC or tumour formation at different stages, as well as their advantages and disadvantages are summarized in Table 2-1.

In general, prospective removal in the pre-transplantation stage is considered to be superior to retrospective removal in the two later stages because of the risks of genetic modification and metastatic transformation[61]. In the pre-transplantation stage, undifferentiated hPSC are mostly purified by positive or negative cell sorting with marker-specific antibodies. Positive selection can provide a higher purity of cells than negative selection, though the yield is compromised. In a more recent development, our group, for the first time, demonstrated the specific killing of undifferentiated hESC by a cytotoxic monoclonal antibody (mAb), mAb84. Injection of hESC after treatment with mAb84 for 45 minutes *in vitro*, prevented teratoma formation in SCID mice[32]. Subsequently, similar methods using cytotoxic small molecules were also proposed[62,63]. A small molecule, PluriSIn#1, was reported to selectively eliminate hPSC while sparing a large array of progenitor and differentiated cells. PluriSIn#1 was reported to inhibit the biosynthesis of MUFA oleate by stearoyl-coA desaturase (SCD1), which is a vital process in hPSC. This consequently leads to the induction of ER stress, protein synthesis attenuation and eventually apoptosis[62]. Another group reported the hPSC-specific anti-apoptotic factor to remove residual hPSC based on a unique hESC signature of

pro- and anti-apoptotic gene expression profile[63]. However, according to the mechanism of action, both the dependence on SCD1 and anti-apoptotic profile might not be limited to hPSC. Therefore, it is unclear whether there will be any potential side effects on differentiated cells. Recently, our group continued to generate new panels of mAbs against hESC leading to the discovery of another hESC-specific cytotoxic antibody, mAb TAG-A1 (A1). Similar to mAb84, A1 holds the potential in preventing teratoma formation in hPSC application.

Table 2-1: Overview of methods to prevent hPSC tumorigenicity.

Stage	Principle	Advantages	Disadvantages	Examples	Ref
1. Pre-transplantation stage: terminally differentiate hPSC or selectively remove undifferentiated hPSC					
Induced differentiation of remaining undifferentiated cells	Extended differentiation or additional differentiated steps by chemical induction	Easy to perform, Inexpensive;	Differentiation efficiency is crucial, Unclear about the effect of chemicals on desired cell;	Direct hPSC differentiation to motor neuron progenitors in the presence of retinoic acid (RA) and sonic hedgehog (SHH)	23,64
Selection by marker-specific antibodies, cytotoxic antibodies or chemicals	Purification of desired cell or removal of undesired cells with specific antibodies or chemicals	High specificity with antibodies; High yield with chemicals;	Antibody and inhibitor specificity is crucial; High cost;	MACS or FACS of well-characterized surface markers, such as SSEA-5, or inducing hPSC death by cytotoxic mAb84, or small molecules	32,54,56,62,63
Selection by transgenic fluorescent marker	Purification of desired cell or removal of undesired cells with transgenic fluorescent marker	High specificity, High yield;	Genetic manipulation introduce another safety hurdle;	Genetic selection of sox1GFP-expressing neural precursors against undifferentiated hPSC or removal of Oct-4 GFP-expressing undifferentiated hPSC	55,65
Purification on physical properties	Division by differences in cell adherence or density gradient centrifugation	Easy to perform, Fast, Inexpensive;	Low specificity, Low yields;	Percoll density centrifugation enrich hESC-derived Cardiomyocytes	57,66
2. Early post-transplantation stage: interrupt tumour progression					
Prevention of tumour formation by cytotoxic drugs	Selectively targeting teratoma-forming cells with high proliferation rate	Easy to perform, Inexpensive, Fast;	Only active teratoma-forming cells can be targeted, Dormant cells cannot be eliminated;	Induction of apoptosis in undifferentiated cells expressing Oct-4/PAR-4 by ceramide analogues	67
Interruption of tumour formation by genetic engineering	Transfection with a fusion gene consisting a "suicide gene" and a bioluminescence reporter gen	Able to trace the kinetics of teratoma formation, Timely, High yields;	All cells carrying the "suicide gene" are eliminated, Genetically modified cells are prone to transformation;	Early detection and ablation of teratomas formation by applying ganciclovir to hESC carrying a bioluminescent reporter gene and thymidine kinase (TK)	68
3. Late post-transplantation stage: remove detected tumour					
Removal of detected tumour by genetic engineering	Transfection of hPSC with transgenic viral gene and induce cell death with specific drugs	High yields;	All cells carrying the "suicide gene" are eliminated, Genetically modified cells are prone to transformation	Removal of detected tumours by applying ganciclovir to hESC carrying thymidine kinase (TK)	59,60,69

2.5 Applications of cytotoxic antibodies

Applications of cytotoxic antibodies are diverse. Firstly, antibody-induced cell death can be used as a cell model to study molecular and cellular functions. In 1995, Bazil et al. generated mAb MEM-59, which recognizes the surface adhesion molecule CD43 on human hematopoietic progenitor cells (HPC) and directly kills HPC via cross-linking of CD43[70]. With MEM-59 induced-HPC death, CD43 was identified as a negative regulator of early hematopoietic events.

Secondly, cytotoxic antibodies can be used to identify novel pathways of cell death and to characterize cell death. Matsuoka et al. generated mAb RE2, which could induce a novel type of cell death in activated interleukin 2-dependent T cells[71]. Zhang et al. also found a cytotoxic antibody, anti-Porimin, targeting Jurkat cells[72]. In this study, they reported the very first cell surface receptor-mediated oncosis as well as some unique features of cellular response upon cell death, such as cell aggregate, plasma membrane permeabilization and membrane blebs.

Thirdly, as mentioned in the previous section, cytotoxic antibodies have been used intensively to eliminate undesired cells, such as the treatment of cancers. Rituximab, a mAb targeting the CD20 antigen on B-lymphocytes, was the first cytotoxic antibody approved to treat B-cell malignancies, such as non-Hodgkin's lymphoma, in combination with chemotherapy[73]. To overcome the rituximab-resistance in some patients, many next-generation anti-CD20 cytotoxic antibodies have been generated[74–76]. There are also other cytotoxic antibodies such as RAV12 that induces recurrent adenocarcinoma cell death[77] and anti-NeuGcGM3 antibodies that directly kill lung cancer cells[78,79].

Although all these antibodies can induce cell death, the modes of cell death and mechanism of action is different.

2.6 Phases and Modes of Cell Death

The terminology of cell death is complicated and sometimes confusing. One way to distinguish different types of cell death is to define it by cellular response in each phase of cell death. In general, cells undergo three phases upon lethal injuries[80]:

a) Reversible "pre-mortal phase";

b) Irreversible cell death, "point-of-no-return";

c) Post-mortal autolytic and degradative changes.

In the pre-mortal phase, there are two major modes of cell death: apoptosis and oncosis. In developmental biology, programmed cell death was introduced to describe that cells in a particular location are scheduled to die for embryologic development and organ differentiation. For a very long-time, programmed cell death has been used synonymously with apoptosis and oncosis has been considered as accidental cell death. However, this concept was proved not to be always true[81], where oncosis can also be a route of programmed cell death. In fact, with the pre-existence of relevant genetic information and cell death factors, every cell may experience "programmed" cell death upon an appropriate stimulus, whereas the route (apoptosis or oncosis) differs among cell types and the stimulus[80,82]. On the contrary, most of post-mortal cellular changes should be termed as "necrosis"[80], which is an ancient word describing cellular changes after cell death. A schematic view of the relationship between apoptosis, oncosis and necrosis has been proposed (Figure 2-3) [83].

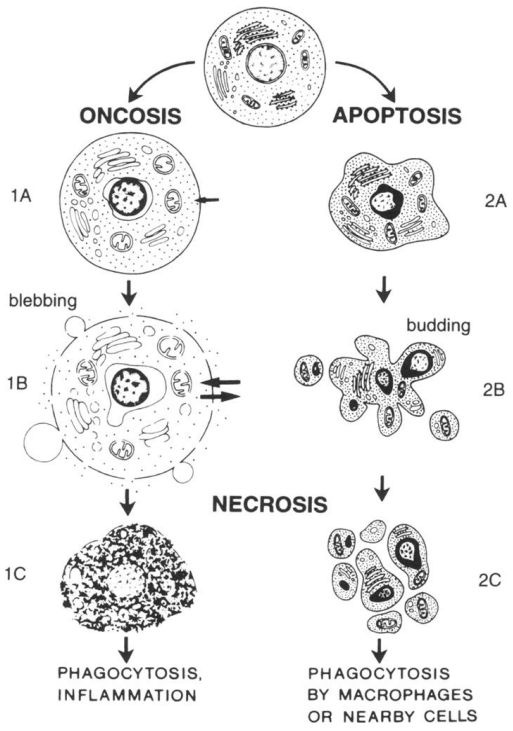

Figure 2-3: Schematic view of the relationship between apoptosis, oncosis and necrosis[83]. 1A: swelling; 1B: vacuolization, blebbing, and increased permeability; 1C: necrotic changes such as coagulation, shrinkage and karyolysis. 2A: Shrinkage and pyknosis; 2B: budding; 2C: necrotic changes such as break up into clusters of apoptotic bodies.

2.6.1 Apoptosis

Apoptosis was first proposed by Kerr et al. in 1972 to describe a pattern of controlled cell deletion. In the regulation of normal development and cell population, apoptosis was thought to play a complementary but opposite role to mitosis[84]. Dysregulation of apoptosis would result in many diseases such as cancer, Alzheimer's and autoimmune diseases[85,86]. The process of apoptosis is tightly controlled and organized. It usually begins with the activation of caspases 12 to 24 hours after a trigger event. In general, there are two major pathways to apoptosis activation: extrinsic caspase-8 activation via receptor-ligand binding, and intrinsic caspase-9 activation via mitochondria[87].

2.6.1.1 Ligand-receptor mediated apoptosis via caspase-8 activation

Apoptosis can be initiated by binding of a ligand to a surface receptor. Well-characterized pathways include death receptors from the tumour necrosis

factor (TNF) receptors superfamily, such as Fas (CD95) receptor. Upon ligand binding, Fas receptors form trimers and their clustered cytoplasmic death domains then recruit adaptor molecules such as Fas-associated death domain (FADD). FADD in turn recruits procaspases-8 and converts it into active caspase-8. Activated caspase-8 continues to convert procaspases-3 into effector caspase-3 and eventually apoptosis[88].

2.6.1.2 Mitochondria-mediated apoptosis via caspase-9 activation

Non-receptor mediated stimuli, such as radiation, hypoxia, hyperthermia, viral infections, and free radicals, can also trigger apoptosis via a mitochondria-mediated pathway. Stimuli cause mitochondrial impairment and release of sequestered pro-apoptotic protein, cytochrome c, into the cytosol. Cytochrome c in turn binds to apoptosis protease activating factor (Apaf-1) and procaspases-9 to form an apoptosome, which activates procaspases-9 to caspase-9 and subsequently converts procaspases-3 into effector caspase-3[89].

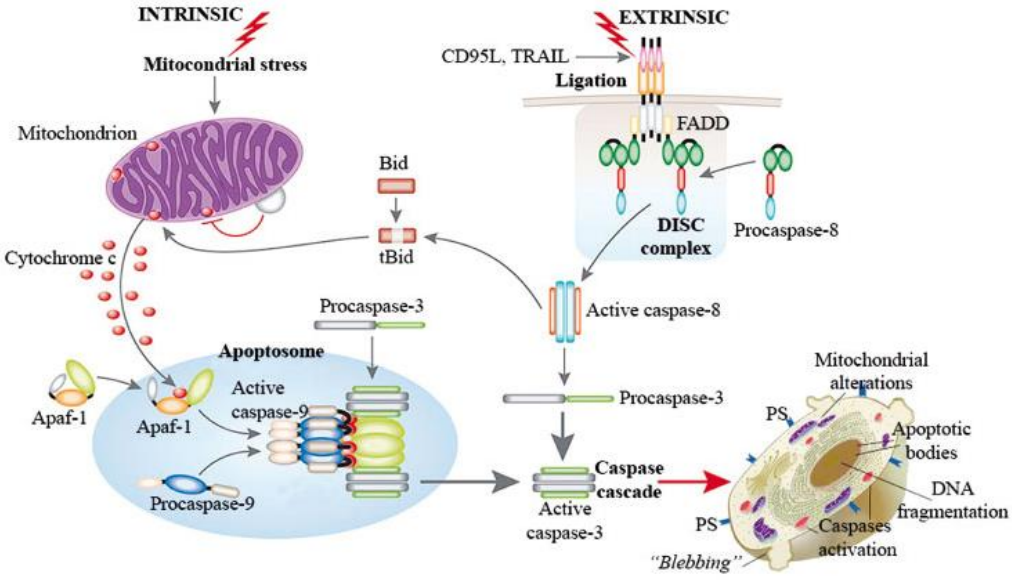

Figure 2-4: Extrinsic (ligand-receptor mediated) and intrinsic (mitochondria-mediated) apoptotic pathways[90].

Upon activation, caspases breakdown certain plasma membrane proteins and cytoskeleton proteins, which in turn leads to membrane budding. Organelles in the cytoplasm become tightly packed and chromatin undergoes condensation, known as pyknosis. Subsequently, the cell breaks apart into apoptotic bodies enclosing DNA fragments and cell organelles by intact plasma membrane[84,89]. Apoptotic bodies with phosphatidylserine expressed on the outer membrane are recognized and engulfed by the neighbouring cells, in particular, macrophages and endothelial cells. Eventually, cell debris is cleared out from the tissue to avoid inflammatory response[89].

Apoptosis can be recognized by a set of well-characterized hallmarks including morphological changes such as cellular shrinkage and budding of plasma membrane (apoptotic bodies), and biochemical changes such as activation of caspases, patterned DNA fragmentation and exposure of phosphatidylserine on the outer membrane surface[91]. Assays to identify the different hallmarks of apoptosis are summarized in Table 2-2.

Table 2-2: Hallmarks of apoptosis and their respective assays.

Hallmarks	Assays
Cell death time: hours	
Cell shrinkage and apoptotic body formation	Scanning/ transmission Electron microscope (TEM or SEM)
Caspase activation	Measure caspase activity
Phosphatidylserine externalization	Annexin V detection
DNA fragmentation	Terminal deoxynucleotidyl transferase mediated dUTP Nick End Labelling (TUNEL) assay

2.6.2 Oncosis

Oncosis was first proposed by Von Rechkling-hausen in 1910 to describe cell death with swelling and was subsequently used to describe ischemic cell death distinct from apoptosis[83]. Though oncosis is the older term, apoptosis has been better elucidated and used to represent programmed cell death. In the recent literature, there are increasing numbers of reports on oncosis, including bacteria-induced macrophage death, toxin or radiation-induced cell death, and cell death due to ischemic heart disease and stroke[92]. Compared to the understanding of apoptosis, the activation pathway of oncosis is still under investigation. Some studies have shown that failure in the ionic pumps of the plasma membrane and decreased levels of cellular ATP might be the cause of oncosis[82,83].

Upon stimulation, oncosis can be triggered within seconds to minutes followed by marked cell shape and volume alteration in the early stage[80]. It was characterized by several morphological and biochemical changes such as apparent swelling of cell and organelles, gross vacuolization, plasma membrane damage and cytoskeleton proteins degradation[80,83]. Buja et al. have postulated that plasma membrane damage in oncosis undergoes in three stages[82,93]. At stage 1, oncosis stimuli induce selective membrane injury leading to cell swelling without generalized increase in cell membrane permeability. At stage 2, plasma membrane damage becomes irreversible with non-selective membrane permeability to propidium iodide (PI) and trypan blue. At stage 3, the cell membrane eventually breaks down, leading to the necrotic phase. Based on the current understanding, the hallmarks of oncosis and the relevant assays for identification are summarized in Table 2-3.

Table 2-3: Hallmarks of oncosis and their respective assays.

Hallmarks	Assays
Rapid cell death (within minutes)	
Plasma membrane damage	Uptake of trypan blue/propidium iodide/dextran beads; Scanning electron microscope (SEM)
Apparent swelling of cell and organelles	Transmission electron microscope (TEM)
Cytoskeleton proteins degradation	Western Blot

2.7 Studies on Cytotoxic Antibody-Induced Cell Death

Besides antibody-dependent cell-mediated cytotoxicity (ADCC) and complement-dependent cytotoxicity (CDC), antibodies can induce direct cell death via apoptosis or oncosis. Some examples of antibody-induced direct cell death are summarized in Table 2-4 and will be discussed in greater detail in this section.

Table 2-4: Cytotoxic antibodies induced cell death.

Antibody	Target cell	Target antigen	Mode of cell death
Cetuximab	Multiple tumour cells	EGFR	Apoptosis
MEM-59	Hematopoietic progenitor cells	CD43	Apoptosis
Rituximab	Non-Hodgkin's lymphoma	CD20	Apoptosis
Anti-APO-1	B-cell lymphoblastoma	Fas receptor	Apoptosis
TRA-8	Primary hepatocellular carcinoma cells and liver cancer cells	DR5 receptor	Apoptosis
RE2	Interleukin 2-dependent T cell	n.d.	Oncosis
Anti-Porimin	Jurkat cell	Porimin	Oncosis
RAV12	Adenocarcinoma	RAAG12	Oncosis
Anti-NeuGcGM3 14F7	Breast carcinoma and melanoma cells	NeuGcGM3	Oncosis
Anti-NeuGcGM3 1E10	Lung tumour cells	NeuGcGM3	Oncosis
mAb84	Human embryonic stem cells	PODXL	Oncosis
GA101	Non-Hodgkin's lymphoma	CD20	Oncosis

2.7.1 Antibody-induced apoptosis

Antibodies can induce apoptosis via three different pathways. First, antibodies targeting growth factor receptors can antagonize ligand–receptor signalling and lead to cell apoptosis. In tumour cells, overexpression of growth factor receptors leads to uncontrolled cell proliferation. Antibodies have been developed to modulate growth factor signalling in tumours, such as cetuximab against epidermal growth factor receptor (EGFR), and trastuzumab (Herceptin) against HER2. The EGFR pathway is known to regulate cell survival and inhibit apoptosis through the PI3K/Akt pathway. Cetuximab binds to EGFR with high affinity and specificity and blocks ligand-binding induced tyrosine kinase-dependent phosphorylation and subsequent downstream signalling. Increased levels of the proapoptotic factor Bax as well as activity of caspases (caspase 3, 8, and 9) were reported in cetuximab-treated DiFi tumour cells[94]. In addition, cetuximab-mediated inactivation of anti-apoptotic protein, Bcl-2, was demonstrated in breast carcinoma[95] and squamous cell carcinoma of the head and neck (SCCHN)[96]. In trastuzumab-induced breast cancer cell apoptosis, inhibition of PI3K/Akt activity as well as down-regulation of Bcl-2 was observed[97].

Second, antibodies can induce apoptosis via antigen crosslinking. In 1995, mAb MEM-59 was reported to recognize a highly sialylated glycoprotein, CD43, and induce cytokine-dependent apoptosis in hematopoietic progenitor cells (HPC)[70]. Cytokine-induced proliferation of HPC was markedly suppressed by immobilized MEM-59 in a dosage-dependent manner. Apoptotic features including cellular shrinkage, DNA fragmentation, and membrane blebbing were observed. MEM-59 induced-apoptosis requires

crosslinking of at least three CD43 molecules and the presence of cytokines. However, it is unclear how signals leading to apoptosis were transduced upon crosslinking of CD43. Rituximab-induced apoptosis has been applied to improve the clinical efficacy in the treatment of non-Hodgkin's lymphomas since lacking of tumour-associated effector cells can lead to rituximab failure in treatments based on ADCC. Crosslinking of CD20 by rituximab upon binding can induce strong and sustained phosphorylation of mitogen activated protein (MAP) kinases, p38. Inhibition of p38 leads to significant reduction in rituximab-induced apoptosis[98]. DNA fragmentation, phosphatidylserine exposure, and increase in caspase-3 activity were detected[73]. However, the precise mechanism how CD20-crosslinking leads to phosphorylation remains to be elucidated.

Third, apoptosis can be triggered upon agonist antibodies binding to surface receptors that transduce proapoptotic signals, such as death receptors of tumour necrosis factor (TNF) receptor family[99]. In 1989, a mAb, anti-APO-1, was reported to induce rapid apoptosis of human B-cell lymphoblastoma cells by selectively binding to apoptosis antigen 1 (APO-1), later identified as Fas receptor[100]. Subsequently, another mAb, TRA-8, was developed as an agonist of the DR5 receptor to induce apoptosis in primary hepatocellular carcinoma cells and liver cancer cells[101]. Binding of anti-APO-1 to Fas receptor and TRA-8 to DR5 receptor triggers the activation of procaspases and the subsequent apoptosis (Figure 2-5).

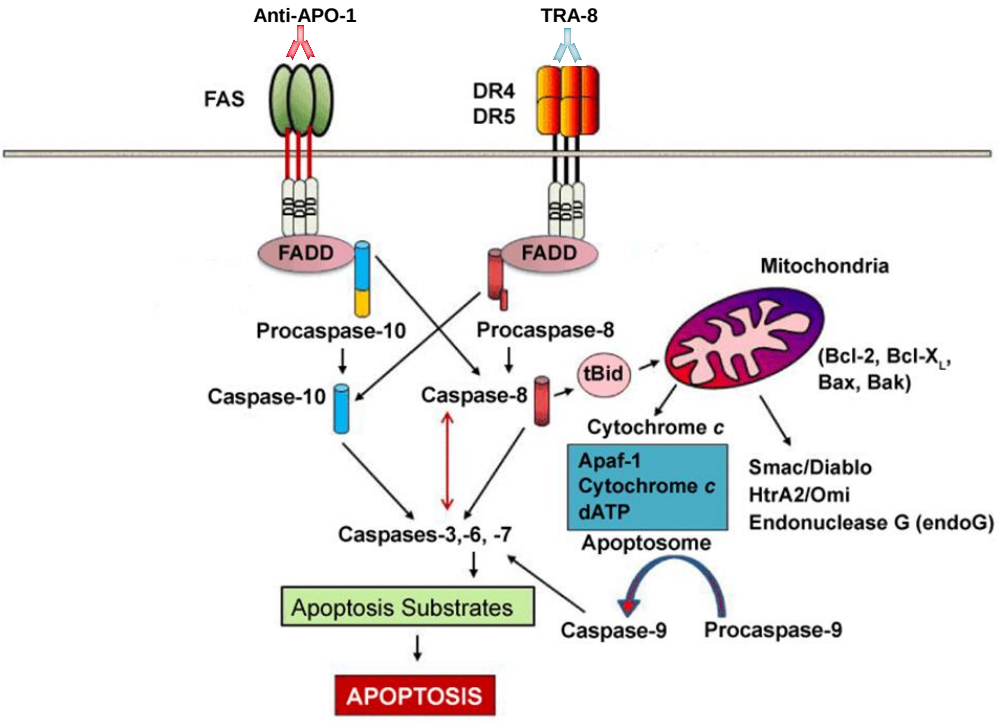

Figure 2-5: Antibody-induced apoptosis via TNF receptor activation[102].

2.7.2 Antibody-induced oncosis

Pathways of antibody-induced oncosis remain to be elucidated. Nevertheless, the mechanism of action has been better understood with increasing studies to characterize the features of antibody-induced oncosis.

In 1995, mAb RE2 (IgG) was reported to directly kill interleukin 2-dependent T cells in a non-apoptotic, complement-independent manner[71]. Cross-linking of cell surface molecules is required for RE2 cytotoxicity since Fab_RE2 has no cytolytic activity whereas cross-linked Fab RE2 by anti-rat immunoglobulin can recapitulate the cytotoxicity (Figure 2-6A). RE2 cytotoxicity is temperature dependent with higher cytotoxicity at 37^{o}C than 4^{o}C, and no cytotoxicity at 0^{o}C (Figure 2-6A). Involvement of cytoskeleton-dependent active progress was postulated since treatment with cytochalasin D (actin polymerization inhibitor) completely blocked RE2 cytotoxicity (Figure

2-6B). Under scanning electron microscopy, giant holes (>1 μm) were observed on cell plasma membrane (Figure 2-6C). In fact, cell swelling upon RE2 treatment was also apparent.

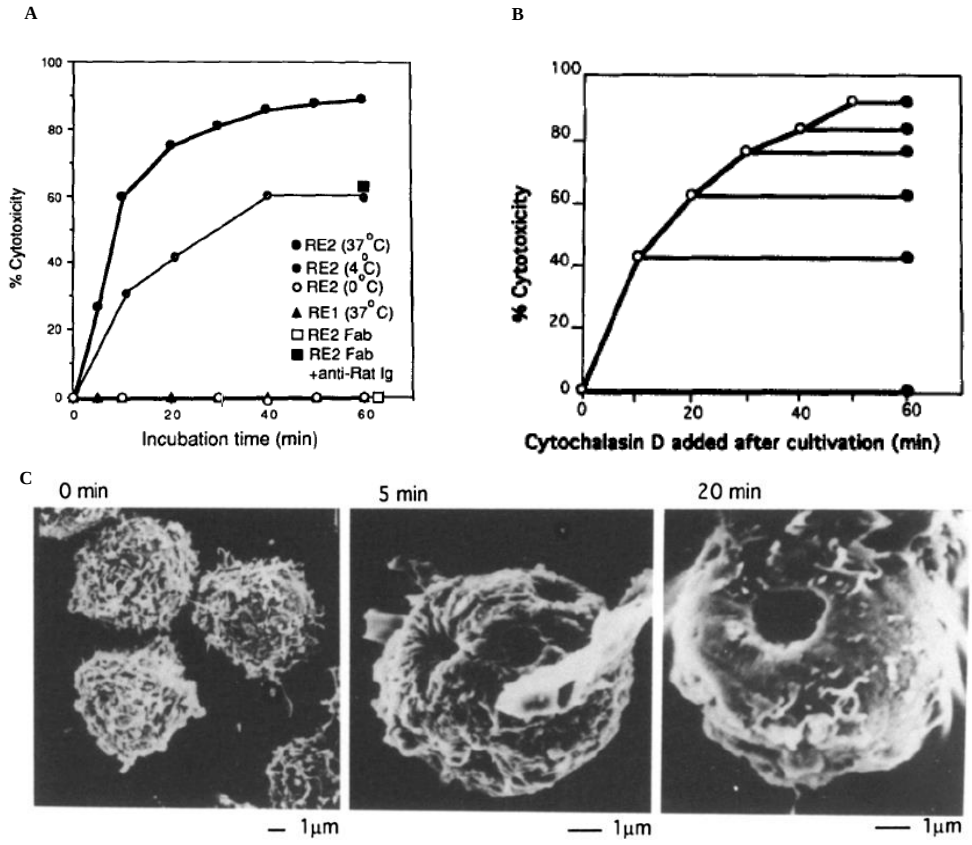

Figure 2-6: RE2-induced T cell oncosis[71].
(A) Kinetics of cytotoxicity effect (measured by trypan blue) of RE2 mAb on T cell clone at different temperatures, and in different formats. (B) Effect of cytochalasin D on cytotoxicity of RE2 at various times when cytochalasin was added (o) and at the end of the assay (•). (C) Giant pore formation on cell membrane.

In 1998, by immunizing mice with apoptotic cells, mAb anti-Porimin (IgM) was generated and found to directly kill Jurkat cells within 20 minutes of incubation in an oncosis-like manner[72]. Anti-Porimin binds to a 110-kDa type I transmembrane protein with extensive O- and N-linked glycans, designated as Porimin (pro-oncosis receptor inducing membrane injury). Porimin was localised on the plasma membrane surface of Jurkat cells under immuno-TEM (Figure 2-7B). Increase in membrane permeability of anti-Porimin-treated

Jurkat cells was detected by propidium iodide uptake. Oncosis features, such as cell aggregate and rapid pore formation on the cell membrane were visualized under SEM (Figure 2-7A).

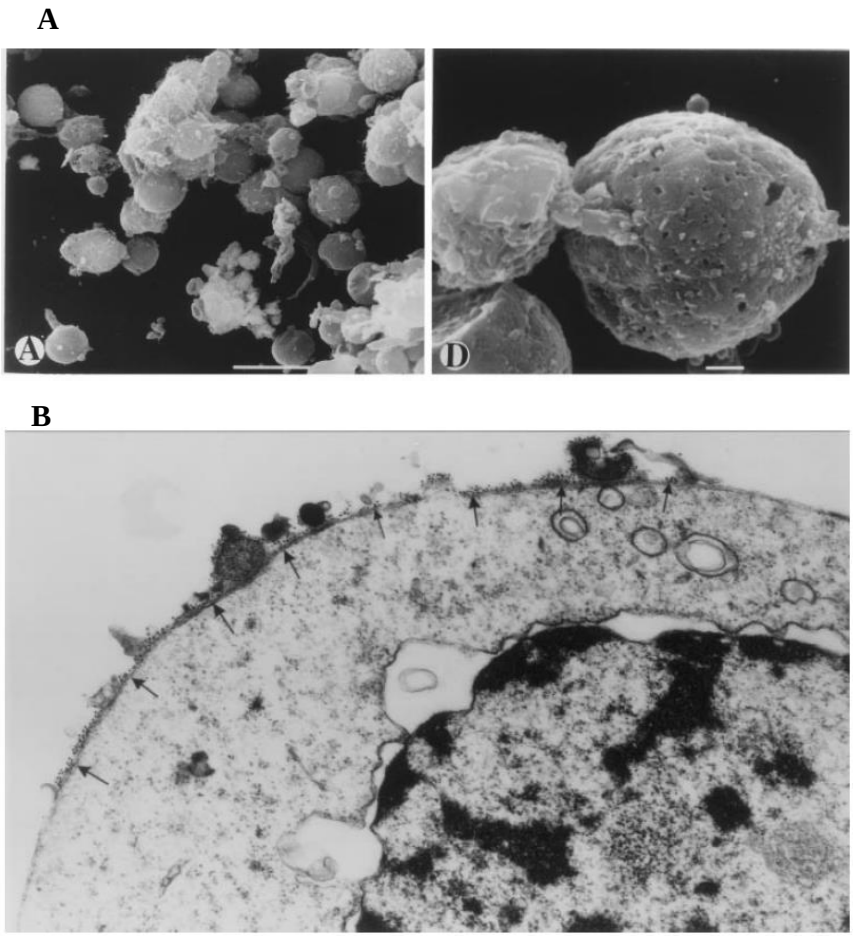

Figure 2-7: Anti-Porimin-induced Jurkat cells oncosis[72].
(A) Cell aggregate and pore formation on plasma membrane were observed in anti-Porimin-treated Jurkat cells. (B) Localisation of the Porimin receptor (arrows) on the surface of plasma membrane of the cell.

In 2007, chimeric antibody RAV12 (IgG_1) was generated based on mAb KID3 to induce oncosis in adenocarcinoma tumour cells [77]. RAV12 was demonstrated to recognize N-linked carbohydrate antigen (RAAG 12) on multiple antigens, which is heavily expressed in adenocarcinoma tumours (Figure 2-8A). Moreover, by analysing the tumour-associated glycans, the

authors concluded that RAV12-binding site on RAAG12 consists minimally of Galβ1-3GlcNAcβ1-3Gal.

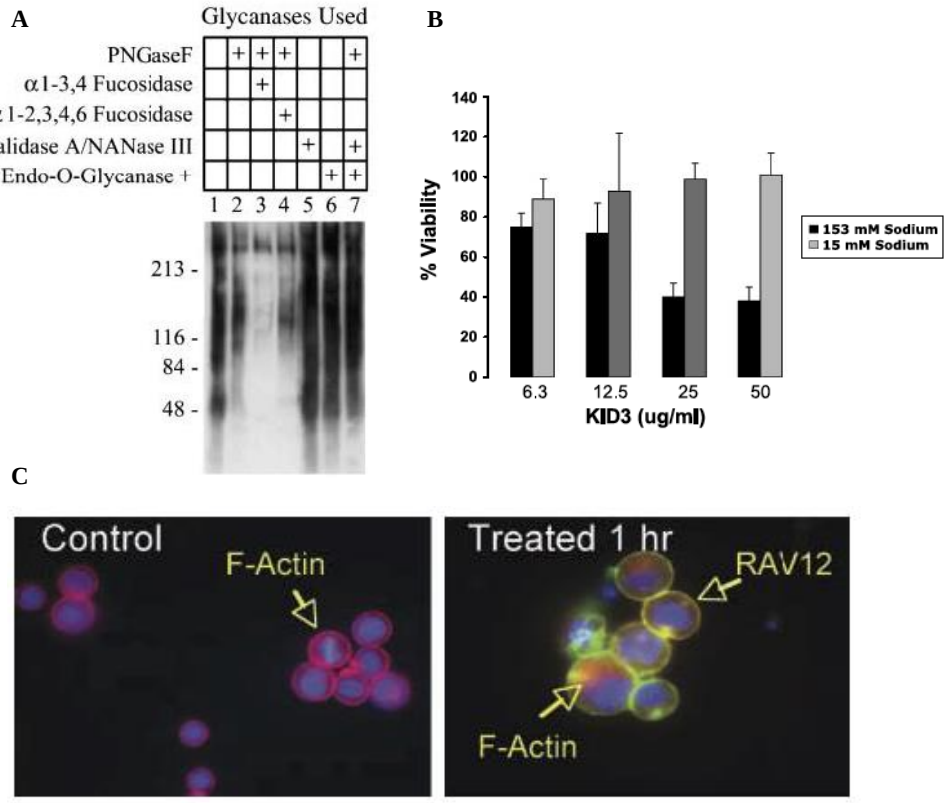

Figure 2-8: RAV12-induced COLO 205 colon tumour cells oncosis[77].
(A) RAV12 recognizes RAAG12, an N-linked carbohydrate epitope on multiple proteins. (B) Reduced extracellular sodium protects COLO 205 cells from KID3 cytotoxicity. (C) RAV12 treatment rapidly induces cell swelling and disrupts actin cytoskeleton.

Intriguingly, similar to RE2, RAV12-mediated cytotoxicity also required cross-linking of surface antigens as cross-linking Fab_RAV12 with a secondary antibody restored the lost cytotoxicity when RAV12 was presented as a monovalent Fab_RAV12. Attenuation of KID3-induced cell death was correlated to the reduced extracellular sodium concentration (Figure 2-8B), which supports the previously suggested role of membrane ion channel failure in oncosis. Rapid cell swelling and disruption of F-actin cytoskeleton were observed upon 1 hour RAV12 treatment (Figure 2-8C).

In 2008, mAb 14F7 (IgG_1) against N-glycolyl GM3 ganglioside (NGcGM3) was reported to induce L1210 murine tumour cell death via oncosis. Similar to previous studies, cellular swelling and membrane pore formation were observed under SEM. Only the bivalent $F(ab)_2$_14F7 and not the monovalent Fab_14F7 retained the cytotoxic capacity of the whole mAb (Figure 2-9A), indicating cross-linking of target antigens is required for the cytotoxicity. In addition, by depleting cellular ganglioside and subsequently incorporating exogenous ganglioside, the authors demonstrated that expression of NGcGM3 ganglioside at the plasma membrane is necessary but not sufficient for 14F7-induced cell death (Figure 2-9B). Re-arrangement of actin cytoskeleton was again identified in this study. Cytochalasin B treatment inhibited 14F7 cytotoxicity in a dosage-dependent manner (Figure 2-9C). Moreover, a linker protein that mediates actin cytoskeleton to the plasma membrane, ezrin, was shown to have increased phosphorylation upon 14F7 treatment (Figure 2-9D). Similar to 14F7, a subsequent study identified another anti-NGcGM3 mAb, 1E10 (IgG_1), to kill non-small cell lung cancer cells via oncosis[78].

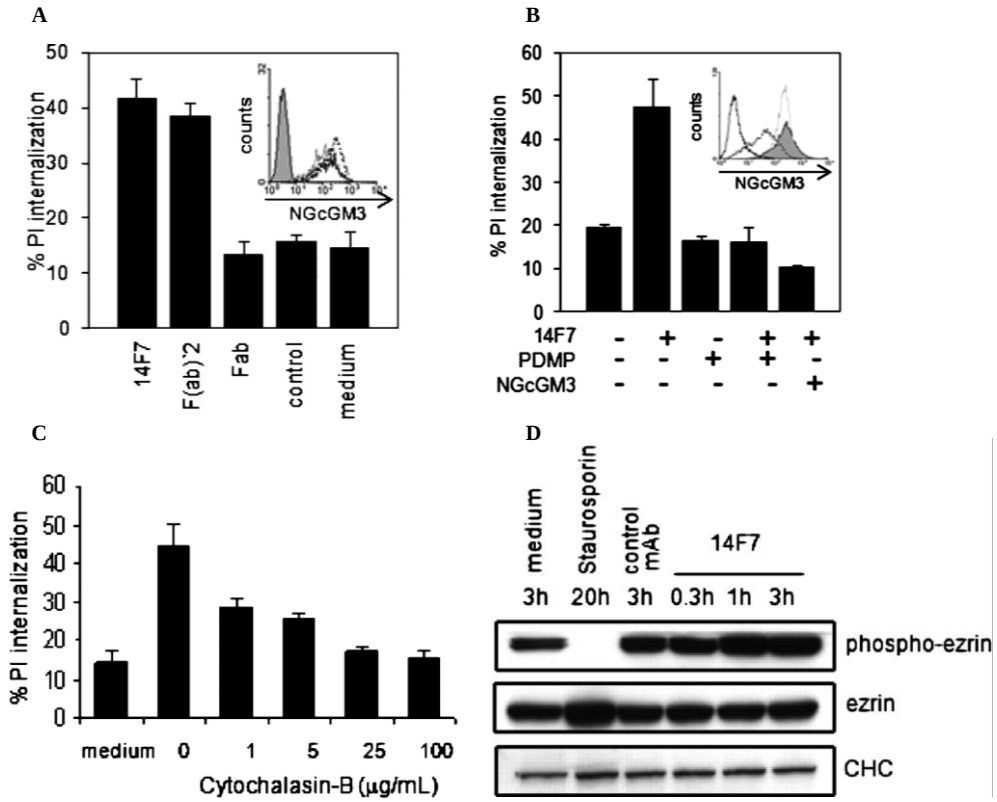

Figure 2-9: Anti-NGcGM3 14F7-induced L1210 murine tumour cell oncosis[79].
(A) $F(ab)_2$_14F7 but not Fab_14F7 retained the cytotoxic capacity of the whole mAb. (B) Expression of NGcGM3 ganglioside at the plasma membrane is necessary but not sufficient for 14F7-induced cell death. D-PDMP depletes cellular ganglioside. NGcGM3 in the figure represents exogenous NGcGM3. (C) Treatment of cytochalasin B inhibits 14F7 cytotoxicity. (D) 14F7 treatment leads to increased level of phosphor-ezrin.

Previously, our group has also investigated mAb84 (IgM)-induced human embryonic stem cell (hESC) oncosis[34]. Oncotic features including rapid cell death, formation of cell aggregates, and membrane pore formation were observed. Role of actin cytoskeleton re-organization was confirmed by the degradation of actin cytoskeleton-associated proteins: talin, α-actinin, and paxillin, as well as co-localisation of paxillin with mAb84 at the peripheral membrane. mAb84 binds to a highly glycosylated protein, podocalyxin (PODXL). Aggregation of PODXL was detected at the plasma membrane under immuno-SEM (Figure 2-10A). Hence, it was proposed that mAb84 binding clusters PODXL upon reduction of cytoskeleton-associated proteins,

which in turn leads to pore formation throughout the plasma membrane (Figure 2-10B). Subsequent studies with antibody fragments of mAb84 suggested that mAb84 cytotoxicity is affected by the valency and the linker construction of the antibody[33].

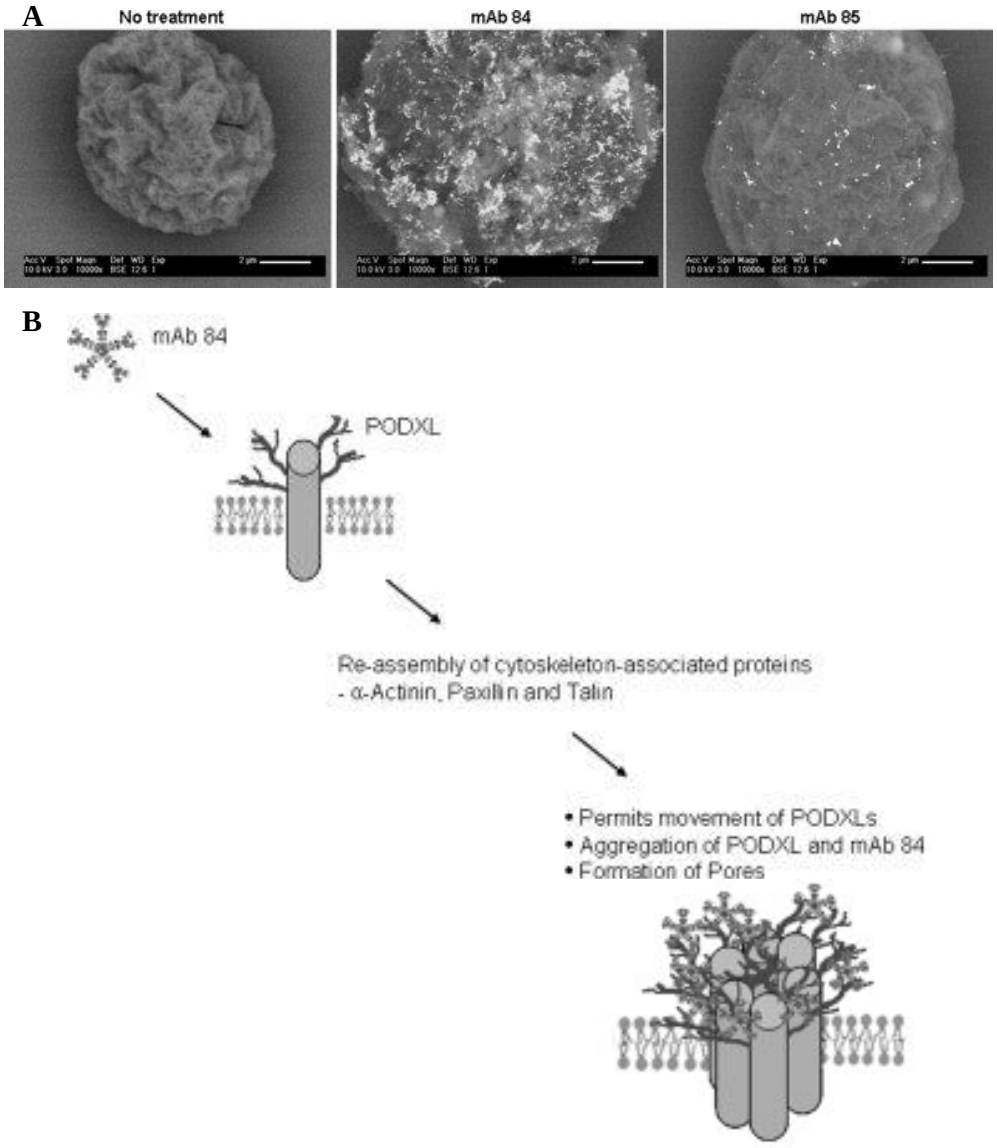

Figure 2-10: mAb84-induced human embryonic stem cell (hESC) oncosis[34].
(A) Aggregation of antigens upon incubation with mAb84 was observed under immuno-SEM. (B) Proposed model for mAb84-mediated oncosis.

Recently, studies on type II anti-CD20 antibody, GA101 (IgG), have provided more insights to understand antibody-induced oncosis[74–76]. Consistent with previously reported antibody-induced oncosis, GA101-induced B lymphoma

cell death featured cell aggregate/homotypic adhesion (HA), actin re-organization, and membrane pore formation. Under TEM, early stage of HA revealed that the initial cell-cell contact was established by microvilli (Figure 2-11).

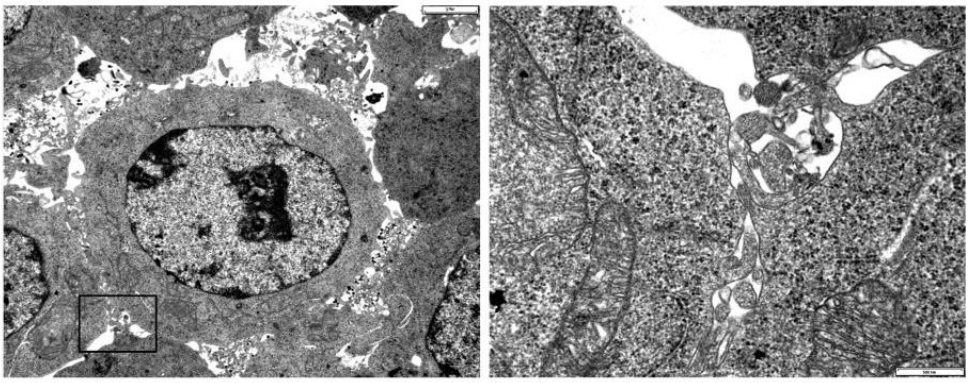

Figure 2-11: Involvement of microvilli in GA101-induced B lymphoma cells homotypic adhesion[74].

Upon GA101 treatment, lysosomal membrane impairment (Figure 2-12A) and the subsequent release of cathepsin (Figure 2-12B) was discovered[75]. Moreover, excess production of ROS was revealed to be essential for GA101 cytotoxicity (Figure 2-12C&D)[76].

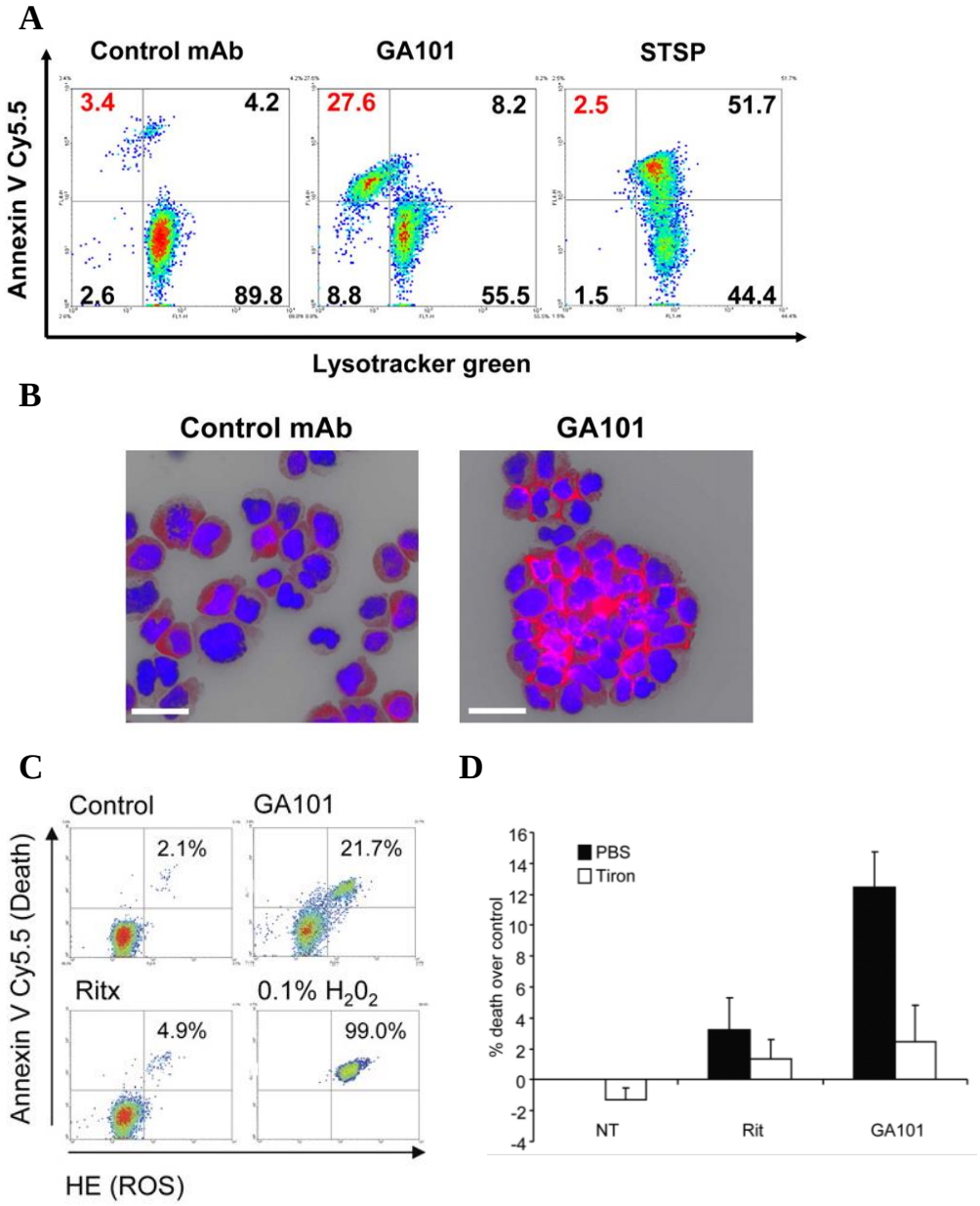

Figure 2-12: GA101-induced B lymphoma cell oncosis[75,76].
(A) Lysosomal membrane impairment detected by lysotracker green was correlated with annexin V measured cell death. (B) GA101 treatment induced the release of lysosomal enzyme, cathepsin. (C) GA101-induced ROS production was detected by dihydroethidium (HE) staining, and correlated to cell death. (D) ROS scavenger, Tiron, can partially block GA101 cytotoxicity.

In conclusion, all the published examples of antibody-induced oncosis exhibit similar hallmarks namely rapid cell death, cell swelling, membrane pore formation and cytoskeleton protein reduction. In addition, studies so far have revealed more features including the involvement of glycan epitopes, cross-

linking of antigens, formation of cell aggregate/homotypic adhesion, lysosomal membrane impairment, and ROS production. However, a more detailed mechanistic pathway remains to be elucidated.

2.8 Summary

Human pluripotent stem cells (hPSC) hold great potential in regenerative medicine and tissue engineering. However, the risk of teratoma formation due to residual undifferentiated hPSC in hPSC-derived products has become the major safety hurdle for hPSC-based therapies. Currently, there are no available methods to completely preclude teratoma formation. Cytotoxic mAbs such as mAb84 and A1 can be used to directly eliminate residual undifferentiated hPSC from differentiated cell products. Two major modes of cell death, namely apoptosis and oncosis, were reviewed in this chapter. Moreover, studies on antibody-induced cell death were discussed. In this thesis, to facilitate the application of A1, we aimed to characterize A1 benchmarking to mAb84 and investigate the mechanism of A1-induced hPSC death.

3 CHAPTER 3 MATERIALS AND METHODS

3.1 Cell culture

3.1.1 Human embryonic stem cells (hESC)

Human embryonic stem cell line, HES-3 was obtained from ES Cell International (ESI, Singapore, http://escellinternational). The cells were cultured at 37^{o}C, 5% CO_2 on matrigel-coated culture dishes supplemented daily with conditioned media (CM) from immortalized mouse feeders, ΔE-MEF[103]. The media used for culturing hESC was KNOCKOUT (KO) media which contained 85% KO–DMEM (DMEM, Dulbecco's modified Eagle's medium) supplemented with 15% KO serum replacer, 1 mM L-glutamine, 25 U/ml penicillin, 25 U/ml streptomycin, 1% non-essential amino acids (NEAA), 0.1 mM 2-mercaptoethanol, and 5 ng/mL of recombinant human fibroblast growth factor-2 (FGF-2) (Invitrogen, Carlsbad, CA, http://www.invitrogen.com). To passage hESC, briefly, once the culture reached confluency, the cells were mechanically cut with cell cutter (Invitrogen) into small square cell sheets, scraped from the culture dish using cell scraper and transferred to a fresh matrigel-coated culture dish. Culture dishes were pre-incubated with matrigel (Becton Dickinson and Company, Franklin Lakes, NJ, http://www.bd.com) at 4^{o}C overnight or at room temperature for at least 4 hours. Cells are passaged at a ratio of 1:6 or 1:8 depending on the confluency.

3.1.2 Human induced pluripotent stem cells (hiPSC)

Human iPSC, ESIMR90, reprogrammed from fetal lung fibroblast[104], were cultured as above described for hESC; with the exception that 100 ng/ml instead of 5 ng/ml of FGF-2 was supplemented to the CM.

3.1.3 Spontaneous differentiation of hESC

To induce hESC differentiation *in vitro*, hESC were mechanically cut and harvested as clumps and cultured as embryoid bodies (EB) for 7 days in EB media (80% KO-DMEM, 20% fetal bovine serum (FBS), 25 U/ml penicillin, 25 μg/ml streptomycin, 2 mM L-glutamine, 0.1 mM NEAA, and 0.1 mM 2-mercaptoethanol) on non-adherent suspension culture dishes (Corning). Subsequently, EB were dissociated with trypsin, plated on gelatinized culture dishes[105] and passaged every 7 days at a 1:4 ratio. EB media was replaced once every two days.

For benzyl-α-GalNac experiment, EB were harvested on day 7 and day 14 for mRNA extraction. For penetration studies, EB were harvested on day 5 or day 6. Alternatively, hESC differentiation was induced by FGF-2 starvation. Here, FGF-2 was not supplemented to daily harvested CM.

3.1.4 Mouse embryonic fibroblast and conditioned media (CM)

Monolayers of immortalized mouse embryonic fibroblast, ΔE-MEF, were grown to confluency in T-flasks and treated with 10 μg/ml mitomycin-C for 3 hours. Following treatment, cells were detached with 0.25% trypsin, seeded onto culture dishes at a density of 8×10^4 cells/cm^2 and incubated overnight to facilitate adhesion. Feeders were then equilibrated in fresh KO media and CM was collected every 24 hours. The CM was clarified by filtration (0.22 μm) and supplemented with an additional 5 ng/ml of FGF-2 prior to addition to hESC cultures.

3.2 Penetration studies into EB

Purified A1 and mAb84 were conjugated to FITC (Fluorescein) using LYNX Rapid conjugation kit (AbD Serotec) according to the manufacturer's

instructions. Briefly, 150 μg of A1 or mAb84 were incubated with Fluorescein solution overnight at room temperature and stopped with the provided quencher. Conjugation efficiency was verified with immuno-fluorescent staining on hESC. Spontaneously differentiated EB spheres were washed with 1% BSA/PBS- and incubated with either 20 μg of FITC-conjugated A1 or FITC-conjugated mAb84 at 4℃ for 4 hours. After incubation, excess antibodies were washed off with 1% BSA/PBS- and EB were pelleted for cryo-embedding and sectioning.

EB were placed into embedding mould covered with dry ice and 2-methylbutane. After removing any excess liquid around the EB, O.C.T. (optimal cutting temperature, water-soluble glycols and resins) compound were added into the mould to cover the EB. Subsequently, the mould was placed into dry ice/methyl butane mixture to freeze the O.C.T. Frozen blocks were either sectioned 5 minutes after frozen or stored at -80 ℃ for future sectioning. Each block was sectioned into 10 μm thick slides and kept at -80 ℃ for future imaging.

3.3 SDS-PAGE and Western Blot

In general, protein lysates were obtained in two ways. For attached hESC on culture plate, cells were scraped off from the surface of the dish in 2% Triton-100/PBS- and lysed for 30 minutes in a centrifuge tube or falcon tube on a rotor. Alternatively, after A1 treatment, cells in suspension were pelleted and lysed in 2% Triton-100/PBS- for 30 minutes in a centrifuge tube on a rotor. Protein lysates were collected in supernatant after 30 minutes centrifugation at 10,000xg. Protein quantification was performed with Pierce protein quantification kit using standards from BSA Protein Assay (Bio-Rad

Laboratories) and read by 96-well Plate Reader (Sunrise Absorbance Reader, TECAN).

Protein lysates (20 μg/well) were separated by SDS-PAGE (NuPAGE 4-12% gradient gel, Invitrogen) under reducing (15% β-mercaptoethanol) or non-reducing conditions followed by western blotting, silver staining or Coomassie staining. For western blotting, resolved proteins were transferred onto PVDF membrane (Millipore) at 100 V for 90 minutes and immunoblotted with appropriately diluted antibodies in PBS- containing 2.5% BSA and 0.05% Tween-20, followed by HRP-conjugated antibodies (1:10000 dilution, DAKO) or near-infrared fluorescence antibodies (1:1000 dilution, Li-cor). Protein bands were detected with either chemiluminescence from chemical reaction with ECL Prime (Amersham) using Medical X-ray processor 2000 (Kodak) or Odyssey fluorescence scanner (Li-cor) respectively. Silver staining was performed using SilverQuest silver staining kit (Invitrogen) according to the manufacturer's protocol and the protein bands corresponding to that on the western blotting membrane were manually excised for mass spectrometry analysis. For Coomassie staining, the gel with resolved proteins was removed from the SDS-PAGE (NuPAGE 4-12% gradient gel, Invitrogen) cassette and stained in sufficient amount of Coomassie stain solution (1 g Coomassie R250, 100 ml acetic acid, 400 ml methanol and 500 ml ddH_2O) for 1 hour. After staining, the gel was washed and hydrated with ddH_2O twice followed by overnight distaining in sufficient amount of distain solution (200 ml methanol, 100 ml acetic acid and 700 ml ddH_2O). Gel with visible protein bands was scanned by Odyssey fluorescence scanner (Li-Cor) for further analysis.

For cytoskeleton reduction assay, hESC were incubated with A1 for 45 minutes, pelleted and lysed with NP40 buffer consisting of 150 mM sodium chloride, 1% IGEPAL (Sigma-Aldrich) and 50 mM Tris with pH 8.0. The antibodies used for immuno-blotting were anti-β-GAPDH, anti-α-actinin, anti-paxillin, anti-talin and anti-vinculin (Millipore).

For Nox families, antibodies used for immuno-blotting were rabbit polyclonal to Nox1, anti-Nox2/gp91phox antibody, and anti-Nox3 antibody (Abcam).

For periodate treatment experiment, after transferring the resolved proteins to PVDF membrane, the membrane was incubated with 2 mM sodium metaperiodate at 37^{o}C for 45 minutes. The membrane was then washed twice with 0.1 M bicarbonate buffer and incubated with 1 mM sodium borohydride at room temperature for 30 minutes. Thereafter, the membrane was washed twice with PBS- and immunoblotted with the appropriately diluted antibodies in PBS- containing 2.5% BSA and 0.05% Tween-20, followed by near-infrared fluorescence antibodies (1:1000 dilutions, Li-cor). Protein bands were detected with Odyssey fluorescence scanner (Li-cor).

3.4 Immuno-precipitation (IP)

Protein lysates in 2% Triton-100/PBS- were used for immuno-precipitation on the automated MEA system (PhyNexus Inc). Briefly, A1 (~100 μg) was directly captured onto Protein G PhyTip® columns (5 μl resin bed, PhyNexus Inc). After washing away the unbound proteins with PBS-, clarified cell lysate was passed through the column functionalized with A1. The column was further washed with PBS- after which bound proteins were eluted at low pH with Elution Buffer (200 mM NaH_2PO_4/140

mM NaCl, pH2.5) and neutralized immediately with 1 M Tris-Cl pH 9.0. The eluate was stored temporarily at 4^{o}C or -20^{o}C for further analysis.

3.5 Mass Spectrometry Analysis

The excised silver-staining gel bands were soaked overnight at 4^{o}C in washing solution (2.5 mM ammonium bicarbonate in Acetonitrile) followed by 20 minutes incubation at 37^{o}C after a change in washing buffer. The gel was then subjected to in-gel proteolysis with trypsin following reduction and s-alkylation of cysteine residues with iodoacetamide. Extracted peptides were subjected to analysis using mass spectrometry on an Orbitrap Velos LC/MS (Thermo Scientific). In Orbitrap Velos, peptide ions are injected tangentially into the electric field between the electrodes and trapped because their electrostatic attraction to the inner electrode is balanced by centrifuge force. Ions of a specific mass-to-charge ratio move in rings that oscillate along the central spindle. The frequency of these harmonic oscillations is independent of the ion velocity and is inversely proportional to the square root of the mass-to-charge ratio (*m/z* or *m/q*). By sensing the ion oscillation, peptide sequence can be determined. Protein IDs were identified by mapping against the Homo sapiens subset of the Uniprot database. Antigen candidates were selected with the following filter setting: match score above 4, peptide coverage above 5, unique number of peptides above 1, and membrane proteins.

3.6 Removal of Sialic Acid and N-linked Glycans

Antigens immunoprecipitated by A1 (as described above) were then treated with sialidase and PNGase F to remove sialic acid and N-linked glycans respectively (New England Biolabs). Removal of terminal sialic acid is also

necessary to expose certain N-linked or O-linked glycans[106]. IP eluate (40 µg) was first denatured in 1x glycoprotein Denaturing Buffer (New England Biolabs) at 95^{o}C for 10 minutes. Denatured proteins were then incubated with 1 µl sialidase at 37^{o}C overnight. Subsequently, 1x G7 Reaction Buffer (New England Biolabs) and 10% NP-40 (New England Biolabs) was added and incubated with 2 µl of PNGase F at 37^{o}C overnight. Digested proteins were subsequently resolved on SDS-PAGE and transferred to Western blot before the removal of O-linked glycans by β-elimination.

3.7 Removal of O-linked Glycan

After sialidase and PNGase F treatment, proteins were separated by SDS-PAGE and transferred to PVDF membrane as described above. Removal of O-linked glycans was achieved by β-elimination. Briefly, PVDF membrane with resolved proteins was incubated with 5 mM NaOH at 42^{o}C overnight.

3.8 Fragmentation of A1

Papain digestion of IgG produces Fab fragments in the presence of reducing agent. In the experiments, 50 µl of 2 mg/ml purified IgG A1 in PBS- was incubated with 100 µl of 0.1 mg/ml papain (Sigma-Aldrich) in freshly made digestion buffer (PBS- containing 0.02 M EDTA, 0.02 M cysteine) for 1 hour in a 37 ℃ water bath. After which, the mixture was removed from the water bath and the digestion reaction terminated by adding 20 µl of 0.3 M iodoacetamide in PBS- and vortexing. The reaction mixture was then dialyzed using VIVASPIN 500 (Sartorius Stedim Biotech) with membrane pore size of 30 kDa. F(ab)2 fragments of A1 were produced using IdeS Protease (Promega). Purified A1 was mixed with IdeS Protease in the ratio of 1 µg of

antibody to 1 unit of IdeS Protease in digestion buffer. Mixture was incubated at 37 ℃ for 45 minutes. The efficiency of enzyme digestion as well as the size of different fragments was verified on SDS-PAGE with Coomassie blue staining and/or western blotting.

3.9 Stoichiometry assay between A1 and hESC

Stoichiometry assay was performed to investigate the number of A1 molecules bound per hESC under saturated binding or unsaturated binding conditions. Briefly, different amounts of A1 (0 μg -12 μg) were incubated with 2 x 10^5 hESC at 4^{o}C for 45 minutes. After incubation, unbound A1 in the supernatant were separated from A1 bound to hESC by centrifugation. The concentration of unbound A1 in the supernatant was measured by ELISA (Enzyme-Linked ImmunoSorbent Assay) and used to calculate the mass of unbound A1. Subsequently, the number of A1 molecules per hESC was estimated based on the equation below (Figure 3-1). At the same time, the cell viability in the pellet was estimated by PI uptake via flow cytometry.

$$n_{A1} = \frac{\frac{m_{A1-total} - m_{A1-unbound}}{M_{A1}} \times N_A}{n_{hESCs}}$$

Figure 3-1: Equation to calculate the number of A1 molecules per hESC from the mass of unbound A1.

3.10 Enzyme-Linked ImmunoSorbent Assay (ELISA)

ELISA was performed to estimate the concentration of unbound A1 in the supernatant after binding with hESC. Capture antibody (goat anti-human IgG1, heavy-chain specific, 5 μg/ml in bicarbonate buffer, 100 μl, Sigma) was coated onto 96-well plate (NUNC MaxiSorp) and incubated for 2 hours at 37^{o}C. The plate was then washed three times with 0.1% Tween/PBS- and

blocked by 3% BSA/PBS- for 1 hour at 37°C. After washing, serial diluted standard antibody (human Fc, chimeric IgG_1 A1 with known concentration) and serial diluted unbound A1 (human Fc, chimeric IgG_1 A1 with unknown concentration) were added to the plate correspondingly. After 1-hour incubation at 37°C, the plate was washed again and incubated with secondary antibody (goat anti-human IgG, Fc specific, peroxidase conjugated, 1:5000 in bicarbonate buffer, Sigma) for 1 hour at 37°C. Subsequently, unbound secondary antibodies were washed away and o-phenylenediamine dihydrochloride (OPD, Pierce) was used as the soluble substrate for development of the colorimetric assay. Due to the enzyme (peroxidase) reaction with H_2O_2, an oxidized product will be formed which reacts with the colourless, chromogenic substrate (OPD) to form an orange coloured product. After 4 minutes, the reaction was stopped by denaturation of the enzyme with hydrochloric acid (100 µl, 3 M). The absorbance value of the oxidized product was read by the 96-well Plate Reader (Sunrise Absorbance Reader, TECAN) at 492 nm with a reference wavelength of 620 nm. Absorbance values of all samples were normalized against the blank value and the relative absorbance of the standards were then plotted against their corresponding concentrations to generate a standard curve. Based on the equation of regression line, the concentration of unbound A1 was calculated.

3.11 Antibody and inhibitors treatment

For mAb treatment experiments, single-cell suspension were harvested and resuspended in 1% BSA/PBS-. Cells (2×10^5) were treated with 5 µg of A1, PBS- as buffer control, for 45 minutes at 4℃ in the volume of 100 µl, and then proceed for flow cytometry analysis.

In sugar blocking assay, 5 μg of A1 was pre-incubated with nine different sugars in the concentration of 2 mM in PBS- (Type-1 H (H1), Type-2 H (H2), Lacto-N-fucopentaose I (LNFP1), Type-1 A (bgA), Type-1 B (bgB), LewisA, LewisB, LewisX and LewisY, Dextra Laboratories Ltd) separately prior to the addition to hESC.

For other inhibitor assays, where appropriate, hESC were pre-incubated with the actin polymerization inhibitors: Latrunculin A (4 μg, Sigma-Aldrich), cytochalasin B (4 μg, Sigma-Aldrich), and cytochalasin D (4 μg, Sigma-Aldrich) for 5 minutes before mAb treatment; or the ROS scavengers: Tiron (4,5-Dihydroxy-1,3-benzenedisulfonic acid disodium salt monohydrate, 50 mM, Sigma-Aldrich) or Tempol (4-Hydroxy-2,2,6,6-tetramethylpiperidine 1-oxyl, 120 mM, Sigma-Aldrich) for 1 hour before mAb treatment; or the NADPH oxidase inhibitors: DPI (Diphenyleneiodonium chloride, 240 μM, Sigma-Aldrich) or Apo (Acetovanillone or Apocynin, 40 mM, Sigma-Aldrich), or MPA (Mycophenolic acid, 3.12 mM, Sigma-Aldrich) for 1 hour before mAb treatment. For in-culture glycan inhibitor treatment, tunicamycin (5 μg/ml, Sigma-Aldrich) and Benzyl 2-acetamido-2-deoxy-α-D-galactopyranoside (Benzyl-α-GalNac, 4 mM, Sigma-Aldrich) were spiked into hESC culture in 6-well flat-bottom plate (Falcon) 4 days after passaging. After 24-hour treatment, hESC were harvested for flow cytometry analysis to check pluripotency, down-regulation of glycosylation as well as A1 binding and killing of hESC. Besides Tiron and Tempol, all other inhibitors were reconstituted in DMSO. Therefore, for negative control, hESC were treated with the same volume of DMSO as the inhibitors treatment.

3.12 SCID mouse teratoma model: *in vitro* treatment

HES-3 were cultured at 37^{o}C, 5% CO_2 on matrigel-coated culture dishes supplemented daily with CM from immortalized mouse feeders, ΔE-MEF. On day 5, the cells were pre-washed 3 times with PBS- and incubated with PBS- for 1.5-2 hours at 37^{o}C, 5% CO_2. Subsequently, cells were harvested into single-cell suspension by gentle pipetting. Single-cell suspension (5 x 10^6 cells/per mouse in 30 μl fresh KO media were mixed with 125 μg of IgG_1 A1 (30 μl in HEPES), and matrigel (30 μl), and immediately injected into the quadriceps of the right hind leg of a female SCID mouse. As a negative control, cells were mixed with 30 μl of HEPES. As an isotype control, cells were mixed with 125 μg of IgG_1 A19 (30 μl in HEPES). To demonstrate the cytotoxicity is independent of ADCC, the single-cell suspension of hESC (5 x 10^6 cells/per mouse in a 30 μl KO media) were mixed with $F(ab)_2$_A1 digested from 125 μg IgG_1 A1 (30 μl in HEPES). Each condition has 3 SCID mice. Animal experiments were performed in accordance with NIH and NACLAR guidelines. Teratoma formation was monitored visually and measured by caliper using a previously established grading system[34]: grade 0 = no visible teratoma (6.32 mm average maximal hind leg diameter), grade 1 = teratoma just detectable (10.55 mm average), grade 2 = teratoma obvious (13.2 mm average), and grade 3 = teratoma impedes locomotion (14.52 mm average).

3.13 SCID mouse teratoma model: *in vivo* treatment

Cell on day 5 were harvested via the same method as described above. Single-cell suspension of hESC (5 x 10^6 cells/per mouse in a 30 μl KO media) were mixed with matrigel (30 μl) and directly injected into the quadriceps of the right hind leg of a female SCID mouse. Subsequently, 125 μg of A1 (30 μl in

HEPES) were injected at approximately the same site to "hunt" previously injected hESC. Similar to *in vitro* treatment, mice in another condition were injected with $F(ab)_2$_A1 digested from 125 μg IgG_1 A1 (30 μl in HEPES). Each condition has 3 SCID mice.

3.14 Light and fluorescence microscopy imaging

Light and fluorescence imaging of cryo-sectioned slides in penetration studies, detection of ROS production and homotypic adhesion upon A1 treatment were performed using an Olympus IX71 inverted microscope (Olympus). Detection of ROS production and homotypic adhesion upon A1 treatment was performed in 96-well plates (CellStar). Fluorescence imaging of F-actin and G-actin upon A1 treatment was acquired using Spinning Disk Confocal (PerkinElmer) in μ-Dish$^{35\ mm\ high}$ (ibidi). F-actin was labelled with Alexa Fluor 488 Phalloidin (Life Technologies), nucleus was stained by Hoechst blue (Life Technologies), and G-actin was labelled with Deoxyribonuclease I, Alexa Fluor 594 Conjugate (Life Technologies).

3.15 Transmission Electron Microscopy

Cells after treatment were fixed with 4% paraformaldehyde and 2.5% glutaraldehyde in 0.1 M cacodylate buffer (pH 7.3) for a first 15 minutes at room temperature and then overnight with fresh fixatives at 4^{o}C; and post-fixed by 1% OsO_4 in 0.1 M cacodylate buffer (pH 7.3) for 1-2 hours at 4^{o}C. Fixed cells were dehydrated in a graded series of ethanol from 30% to 100% and propylene oxide. Subsequently, dehydrated cells were embedded in Spurr resin (SPI-CHEM, Low Viscosity Spurr Kit). Silver to gold ultra-thin sections were cut with ultra-microtome (Leica Ultracut UCT) and stained in 1% uranyl

acetate for 15 minutes and lead citrate for 10 minutes. Stained sections were examined with a transmission electron microscope (JEOL JEM 2010F TEM, 200kV, FEG).

3.16 Scanning Electron Microscopy

After A1 treatment, unbound A1 were washed away and cells were primarily fixed by 4% paraformaldehyde and 2.5% glutaraldehyde in PBS- (pH 7.3) for 15 minutes at room temperature. Fixed cells were then washed and resuspended with deionized water and loaded onto poly-L-lysine-coated coverslips (20 mm in diameter). Cells were allowed to settle down for 10-15 minutes. Subsequently, cells were fixed with 4% paraformaldehyde and 2.5% glutaraldehyde (pH 7.3, in PBS-) for 3-5 hours. Fixed cells were dehydrated in a graded series of ethanol from 30% to 100%. Subsequently, dehydrated cells were dried by Critical Point Dryer (Tousimis Autosamdri-815) and surface coated with Platinum (40 seconds, 40 mA, JEOL JFC-1600 Fine Coater). Coated samples were examined with a scanning electron microscope (Helios NanoLab DualBeam, FEI) and cell morphology was observed under secondary electron mode. For ROS depletion experiment, cells were firstly pre-incubated with ROS scavenger Tiron prior to A1 treatment. For immuno-SEM, cells were primarily fixed with only 4% paraformaldehyde for 15 minutes. After primary fixation, un-reacted aldehyde was blocked away with 100 mM glycine. After 3 times wash with 1% BSA/PBS-, cells were incubated with 100 μl gold-conjugated secondary antibody (25 nm, goat anti-human, IgG, EMS) for 1 hour. Cells were then washed and fixed with 4% paraformaldehyde and 2.5% glutaraldehyde in PBS- (pH 7.3) for 2 hours before loaded to poly-L-lysine-coated coverslips (10 mm in diameter). After dehydration and critical point

drying as describe above, cells on coverslips were surface coated with carbon. Coated samples were examined with a scanning electron microscope (JEOL JSM-6701F, FEG). Cell morphology was observed under secondary electron mode, gold particles were detected under backscatter mode, and a combined mode is available to overlay cell morphology with gold particles.

3.17 Induction of apoptosis via Ultra-violet (UV) irradiation

Confluent hESC cultures were exposed to 200 mJ of UV using a UV cross-linker (UV Stratalinker 1800, Stratagene) to induce apoptosis[34]. After UV exposure, the cells were maintained at 37^{o}C/5% CO_2 for 20 hours before harvesting for apoptotic assays.

3.18 Caspases assay

Guava Caspase3/7-FAM kit and Caspase9-SR kit (Millipore) were used to measure caspase 3/7/9 activity. The Guava Caspase Assays employ a FLICA (Fluorescent Labelled Inhibitor of Caspase) reagent that specifically identifies active caspases. Each FLICA is comprised of three subunits: an active site binding peptide to confer specificity (DEVD for caspase 3/7, and LEHD for caspase 9); a covalent crosslinking agent (FMK); and a green (FAM) or orange-red fluorescent probe (SR). In this assay, the membrane integrity and cell viability were simultaneously evaluated using 7-AAD. Cells (non-treated, UV-treated, A1-treated) were resuspended in 100 µl PBS- at a concentration of 2 x 10^6 cells/ml and incubated with 10 µl of caspase reagent for 1 hour at 37^{o}C in a CO_2 incubator. At the end of incubation, cells were washed twice with provided washing buffer, resuspended in 200 µl of 7-AAD working solution and incubated for 10 minutes at room temperature. After incubation,

cells were washed twice and analysed by flow cytometer (Guava EasyCyte, Millipore).

3.19 TUNEL assay

TUNEL assay measures the extent of DNA fragmentation upon cell death[107]. APO-DIRECT TUNEL Kit (Millipore) was used. UV-treated hESC was used as a positive control since UV crosslinking is reported to induce apoptosis in hESC[34]. Cells (non-treated, UV-treated, A1-treated) were fixed in 1% paraformaldehyde in PBS- (pH 7.4) at a concentration of 1-2 x 10^6 cells/ml and the suspension was placed on ice for 30-60 minutes. After cells were washed twice with PBS-, they were resuspended in 70% ethanol at a concentration of 1-2 x 10^6 cells/ml and incubated for 1 hour on ice. Subsequently, cells were washed three times and resuspended in 50 μl of staining solution (10 μl of TdT reaction buffer, 0.75 μl of TdT enzyme, 8 μl of fluorescein-dUTP and 32.25 μl of distilled H_2O). Cells were then incubated for 1 hour at 37^{o}C and resuspended every 15 minutes. After incubation, cells were washed with rinsing buffer, resuspended in 0.5 ml of the Propidium Iodide/RNaseA solution, incubated in the dark for 30 minutes at room temperature, and analysed by flow cytometer (FACScan, Becton Dickinson FACS Calibur).

3.20 Detection of ROS

ROS production was detected with HE staining (Dihydroethidium, Sigma-Aldrich). HE is a cell-permeable fluorogenic probe that reacts with ROS to form ethidium. Ethidium intercalates within double-stranded DNA in the nucleus and emits red fluorescence. Cells after pre-incubation with ROS

scavengers and A1 treatment were resuspended in 200 µl 1% BSA/PBS- with 25 µM HE and incubated for 30 minutes in the dark at room temperature. After incubation, the intensity of red fluorescence was directly analysed on a Guava InCyte Flow Cytometer (Merck Millipore) with detection emission in the Red-HLog channel. Alternatively, 2 x 10^5 hESC were pre-incubated with 30 µM carboxy-H2DCFDA (Life Technologies) in 100 µl 1%BSA/PBS- for 10 minutes at 37℃, and transferred into a flat-bottomed 96-well plate (BD Science). Carboxy-H2DCFDA is oxidized in the presence of ROS to carboxy-DCF, which emits green fluorescence. Cells were imaged before and after treatment with 5 µg of A1.

3.21 Assessment of homotypic adhesion formation

Human ESC (2 x 10^5) were pre-incubated with 50 mM Tiron or PBS- in 100 µl 1% BSA/PBS- in a flat-bottomed 96-well plastic plate (BD Science) for 1 hour at 4^oC. After pre-incubation, cells were treated with 5 µg of A1 or $F(ab)_2$_A1 or Fab_A1 or PBS- for 45 minutes at 4^oC. Subsequently, cells were viewed using light microscopy imaging.

3.22 Flow cytometry analysis-cytotoxicity assay

Cytotoxicity of A1 or digested A1 fragments after papain treatment on hESC, or spontaneously differentiated hESC, or hESC after pre-treatment with inhibitors was evaluated using propidium iodide (PI) exclusion assays via flow cytometry analysis. PI (1.25 mg/ml) were directly added into cell suspension after treatment with A1 or digested A1 fragments and analysed on a Guava InCyte Flow Cytometer (Merck Millipore) with detection emission in the Red-HLog channel or on a FACScan (Becton Dickinson FACS Calibur) with

detection emission in the FL-3 channel. To demonstrate the correlation between ROS production and cell death, cells were stained with 25 μM HE as previously described for 10 minutes first and together with 1.5 pM Sytox green dead-cell stain (Life Technologies) for another 20 minutes. After incubation, cells were analysed on a Guava InCyte Flow Cytometer (Merck Millipore) with detection emission in the Red-HLog channel for HE and Green-HLog channel for Sytox green. All incubations were performed at 4^{o}C unless otherwise indicated.

3.23 Flow cytometry analysis-binding assay

To evaluate the pluripotency-associated markers of hESC, cells at a concentration of 2 x 10^{6} cells/ml were incubated with mAb to Oct3/4 (2.5 μg, Santa Cruz) or mAb to Tra-1-60 (Millipore) in 100 μl 1% BSA/PBS- for 30 minutes. Cells were then washed with cold 1% BSA/PBS-, and further incubated for 15 minutes with FITC-conjugated goat anti-mouse secondary antibody (1:500 dilutions, DAKO) or APC-Conjugated rabbit anti-mouse secondary antibody (1:500 dilution, DAKO). After incubation, cells were again washed and resuspended in 1% BSA/PBS- for analysis on a FACScan (Becton Dickinson FACS Calibur) with detection emission in the FL-1 channel for FITC signal and FL-4 channel for APC signal, or on a Guava InCyte Flow Cytometer (Merck Millipore) with detection emission in the Green-HLog channel for FITC signal and Red2-HLog channel for APC signal. As controls, cells were only incubated with secondary antibody (FITC-conjugated antibody or APC-conjugated antibody). To evaluate the binding of A1 to hESC or hESC after pre-treatment with inhibitors, cells were incubated with goat anti-human FITC secondary antibody (1:700 dilutions, DAKO) for

15 minutes and washed twice before Flow cytometry analysis. To evaluate the binding of papain or IdeS protease digested A1 fragments or undigested A1 to hESC, cells were incubated with anti-human Fc specific primary antibody conjugated with biotin (1:2000 dilutions, Sigma-Aldrich) for 30 minutes and followed by 15 minutes incubation with FITC-conjugated streptavidin (1:100 dilutions, DAKO), or cells were incubated with kappa-light chain specific FITC-conjugated antibody (1:100 dilutions, Sigma-Aldrich). To evaluate the down-regulation of N-glycosylation after tunicamycin treatment, hESC or hESC after tunicamycin treatment was incubated with biotin-conjugated Concanavalin A (4 μg/ml in DMSO, Vector Labs) for 30 minutes. After washing, cells were incubated with streptavidin-FITC (1:100 dilutions, DAKO) for 15 minutes before Flow cytometry analysis. All incubations were performed at 4^{o}C unless otherwise indicated.

3.24 Measurement of NADPH oxidase activity

Human ESC with or without A1 treatment were washed and pelleted with 2 x 10^6 cells in a micro-centrifuge tube for NADP/NADPH Assay (Abcam). Total NADP/NADPH was extracted from each sample according to the manufacturer's protocol. NADPH was obtained by decomposing the NADP component with heat. To quantify the concentration of total NADP/NADPH or NADPH, a standard curve was generated with provided NADPH standards. The average absorbance of the duplicates for each standard or sample was determined and normalized against the mean absorbance value of the blank. Based on the trend line equation of the standard curve, the concentration of total NADP/NADPH or NADPH of the samples was obtained. The concentration of NADP was obtained by subtracting the concentration of

NADPH from that of total NADP/NADPH. Therefore, the ratio of NADP/NADPH was obtained.

3.25 Knockdown of Nox2/gp91 and Nox3 using small interfering RNA

Human ESC maintained either with daily change of CM or mTeSR (StemCell Technologies), were passaged weekly by cutting into small clumps. On the day of transfection, healthy and exponentially growing cells (70%-90% confluence on day 5 after passaging) were fed with mTeSR (8 ml/6 cm plate) 6-8 hour prior to transfection. Cells were then incubated with ROCK Inhibitor Y-27632 (Calbiochem, 10 μM) for 1 hour. These steps are necessary to preserve cell viability after transfection. At the same time, transfection solution was prepared. 80 pmol to 120 pmol of target siRNA or scramble siRNA (Silencer Select, Life Technologies) or 5 μl of Lipofectamine RNAimax were mixed separately in OPTI-MEMI (Invitrogen) in the volume of 50 μl; and incubated at room temperature for 5 minutes. The contents of the two tubes were combined by gentle pipetting and incubated at room temperature for 30-50 minutes. The resulting transfection solution (100 μl) was used to resuspend the cell pellet produced after Accutase dissociation. After incubation, cells were then dissociated into single-cell suspension using Accutase (STEMCELLPRO) (3 ml/6 cm plate, 18 minutes at 37^{o}C), and neutralized by 4 ml of mTeSR. Cells were then pelleted by centrifugation (25xg, 3 minutes). Cells (1×10^{6} to 2×10^{6}) were equally allocated to each condition. Cell pellet was resuspended in 100 μl of siRNA/Lipofectamine transfection solution and incubated at room temperature for 10-15 minutes. At the end of the incubation, 1.5 ml of pre-warmed fresh growth media (mTeSR containing ROCK inhibitor at a final concentration of 10 μM) was added and

the suspension was transferred into a Matrigel-coated well of a six-well plate, followed by overnight incubation at 37^{o}C, 5% CO_2. Transfected cells were maintained with daily change of mTeSR and harvested for various assays 4-5 days after transfection. Knockdown efficiency was assessed by western blotting and qRT-PCR.

3.26 RNA extraction, reverse transcription, and qRT-PCR

Total mRNAs were extracted from cell pellets using RNeasy® MiniKit (Qiagen) according to the manufacturer's instructions. Then, cDNAs were produced using Oligo dT (Life Technologies) and M-MLV reverse transcription kit (Promega) according to the manufacturer's protocol. Quantitative real-time polymerase chain reaction (qRT-PCR) was performed using Fast SYBR green (Applied Biosystems) or TaqMan Fast Advanced Master Mix (Life Technologies) with 7500 Fast Real time PCR system (Applied Biosystems). For Nox2 and Nox3 knockdown experiment, TaqMan Gene Expression Assay containing specific primers and probes was used (Nox2: Hs00166163_m1, Nox3: Hs01098883_m1, and GAPDH: Hs02758991_g1). For markers of pluripotency, endoderm, mesoderm and ectoderm, specific primers sequences are listed in Table 3-1.

Table 3-1: Sequences of specific primers used in qRT-PCR for markers of pluripotency, endoderm, mesoderm and ectoderm.

	Gene name	Primer sequences (F)	Primer sequences (R)
Pluripotency	Oct4	F: 5'-GGCCGCAGCTTACACATGTT-3'	R: 5'-AACGACCATCTGCCGCTTT-3'
	Nanog	F: 5'-GAAAAACAACTGGCCGAAGAAT-3'	R: 5'-GGTGCTGAGGCCTTCTGC-3'
Endoderm	AFP	F: 5'-TCCCTCCTGCATTCTCTGATG-3'	R: 5'-CCTGAGCTTGGCACAGATCC-3'
	GATA6	F: 5'-GCGGCTTGGATTGTCCTGT-3'	R: 5'-TGCGCCATAAGGTGGTAGTTG-3'
Mesoderm	Hand1	F: 5'-TTCTTCGAATCGTGGTGGTTT-3'	R: 5'-CAGGAAGTGCAGCGACAAAA-3'
	Nkx2.5	F: 5'-TCCCCTGGATTTTGCATTCA-3'	R: 5'-AGGATCACTCATTGCACGCTG-3'
Ectoderm	Pax6	F: 5'-CCAGCTTCACCATGGCAAAT-3'	R: 5'-GGCAGCATGCAGGAGTATGAG-3'
	Msx1	F: 5'-GCCATGTCTCCTGCATAGCTT-3'	R: 5'-CGCTTTTCTTGCCTGGTGTC-3'

3.27 Mitochondrial membrane permeability assay

The membrane-permeable JC-1 dye (Molecular Probes) was used to assess mitochondrial membrane permeability. JC-1 dye accumulation in mitochondria is potential-dependent. JC-1 monomers emit green fluorescence (~529 nm) whist JC-1 aggregates emit red fluorescence (~590 nm). Mitochondrial depolarization is indicated by a decrease in the red/green fluorescence intensity ratio. After A1 treatment, cells with or without Nox2 knockdown were washed and incubated with JC-1 dye (1:100 dilutions) at 37^{o}C for 30 minutes. After incubation, red and green fluorescence changes were monitored with flow cytometry analysis.

3.28 Statistics

Error bars represent the standard error of mean (SEM) of at least 3 independent experiments unless otherwise stated. Significance in difference between the experimental groups was calculated using unpaired, 2-tailed t test. The degree of statistical significance was represented by the number of asterisks displayed on the figures determined by P values as follows: * < .05, ** < .01, *** < .001.

4 CHAPTER 4 *IN VITRO* CHARACTERIZATION OF A1

4.1 Discovery of mAb TAG-A1 (A1)

A panel of monoclonal antibodies (mAb) against hESC surface markers was generated by immunizing BALB/c mice with undifferentiated hESC (Figure 4-1). Briefly, viable undifferentiated hESC were injected into BALB/c mice over a period of 5 weeks. Serum was drawn from immunized mice and screened for the presence of antibodies that bind to hESC. The positive mice were then sacrificed to harvest the spleens. The spleenocytes were subsequently fused with Sp2/0 myeloma cells and colonies of hybridomas were isolated after hypoxanthine-aminopterin-thymidine (HAT) selection. Specificity of the mAbs produced from the hybridomas was first screened against hESC lines including hES-3, hES-2, and hES-4. Secondary screening was performed for positive clones to determine the cross reactivity of these mAbs with other cells lines, namely human fibroblast (IMR90), mouse feeders (ΔE-MEF), mouse embryonic stem cells (mESC), human embryonic carcinoma (EC) cells (Ntera, 2102Ep, NCCIT), and other human cell lines (HEK-293, HeLa). Thus, a panel of mAbs specifically against hESC surface markers was shortlisted. From this panel of mAbs, mAb TAG-A1 (A1) was identified to selectively bind to and kill undifferentiated hESC. This property is similar to a previously described mAb, mAb84. However unlike mAb84 which is an IgM, A1 is an IgG. Since mAb A1 is a mouse mAb, to avoid immune response when used in humans, chimeric A1 with human Fc was produced. The antibody genes encoding the variable region of the mAb was amplified by PCR and cloned into a mammalian expression vector containing the human IgG1 constant regions. The vector was then transfected into CHO

cells for expression of the chimeric mAb. For this project, all experiments were performed with chimeric A1.

This chapter reports the *in vitro* characterization of A1 and where relevant, benchmarking it to mAb84. The specificity of A1 cytotoxicity was first determined against undifferentiated hESC, hiPSC and spontaneously differentiated hESC via embryoid body (EB) formation or FGF-2 starvation. Subsequently, the antigen target of A1 on hESC was investigated. Next, A1 was characterized by determining its dosage efficiency, killing kinetics, nucleic acid and amino acid sequences in the variable regions, competitive binding, and penetration efficiency into EB, benchmarking to mAb84. Last but not the least, the binding stoichiometry between A1 and hESC, as well as the association between A1 cytotoxicity and its structure e.g. bivalency vs monovalency and the Fc-domain were examined.

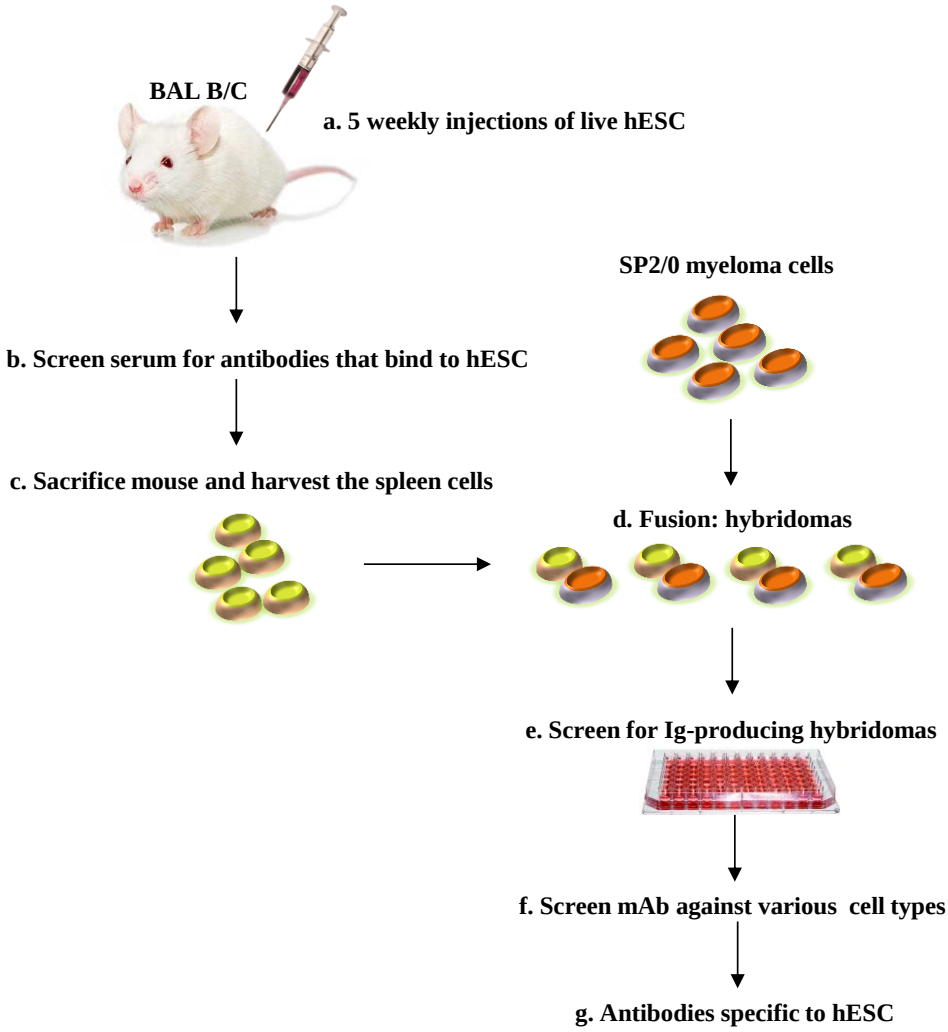

Figure 4-1: Generation of monoclonal antibodies against hESC surface markers by hybridoma formation.

4.2 A1 binds to and kills undifferentiated hPSC

To investigate the reactivity of A1 to undifferentiated hPSC, hESC or hiPSC were treated with A1 for 45 minutes at 4^{o}C. After incubation, A1 binding and killing were analysed by flow cytometry analysis. A1 showed strong binding to both undifferentiated hESC and hiPSC derived from human fetal lung fibroblasts (ESIMR90) (Figure 4-2A). Cell viability was estimated via the uptake of a cell impermeable dye, propidium iodide (PI), which binds to nucleic acids in cells with compromised plasma membrane and emits a red fluorescence. Increased PI uptake indicates cell death (Figure 4-2B). In-house

mAb8 (IgG_1) was used as an isotype control which binds to hESC without cytotoxicity. Upon A1 treatment, both hESC and hiPSC had a significant decrease in cell viability (Figure 4-2C).

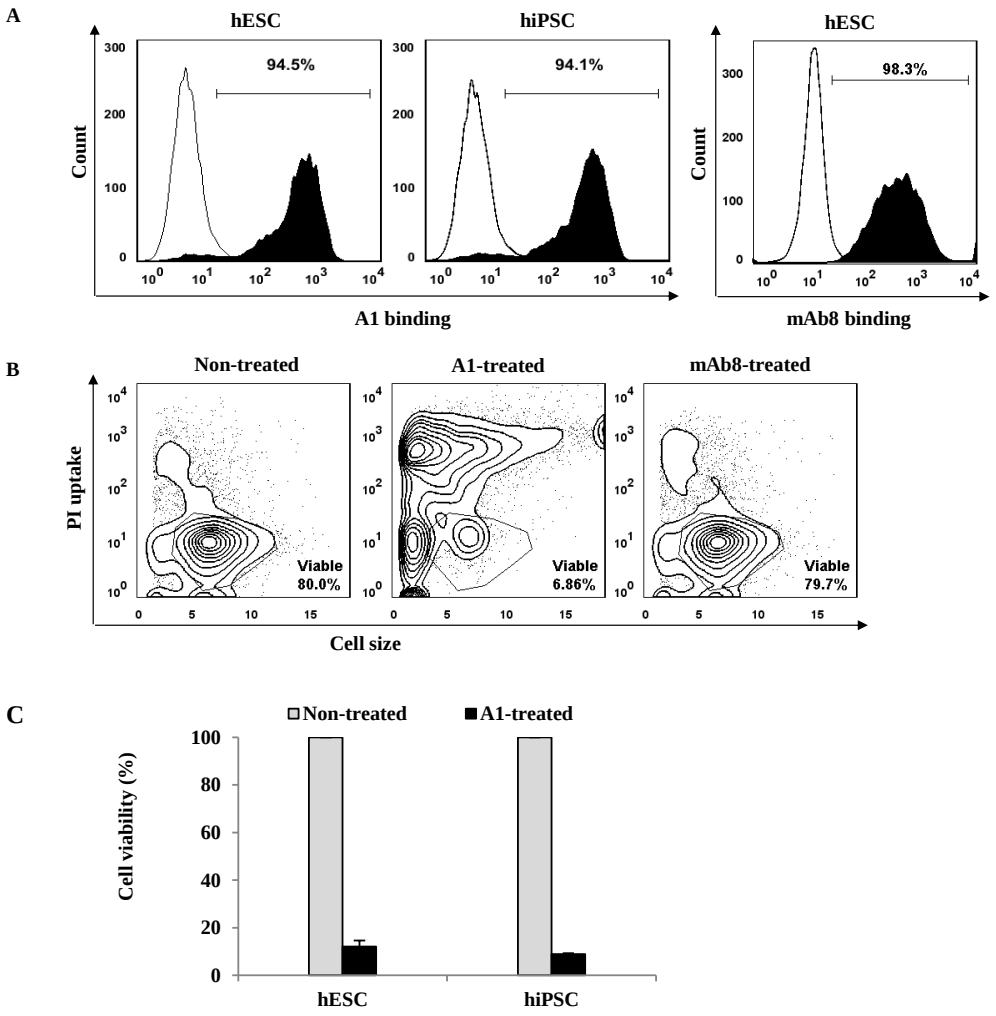

Figure 4-2: A1 binds to and kills both undifferentiated hESC and hiPSC.
Either hESC or hiPSC (2 x 10^5 in 100 µl) were treated with 5 µg of A1 or mAb8 for 45 minutes at 4°C. (A) A1 showed strong binding to both hESC (HES-3) and hiPSC (ESIMR90). mAb8 also binds to hESC. Binding of mAbs was assessed with FITC-conjugated secondary antibody by flow cytometry analysis. Representative histograms are shown. Open histogram represents non-treated cells and shaded histogram represents A1-treated cells. Gated area represents positive mAb binding. (B) Upon A1 treatment, hESC viability dropped from 80.0% to 6.86%. mAb8 binding on hESC did not change hESC viability. Cell viability was assessed via PI uptake by flow cytometry analysis. Gated population represents viable cells. (C) A1 kills both hESC (HES-3) and hiPSC (ESIMR90). Data are represented as mean ± SEM.

4.3 A1 cytotoxicity is specific to undifferentiated hPSC

To remove undifferentiated hPSC from differentiated cell products, the specificity of A1 is crucial. To determine if A1 binding and cytotoxicity is

only specific to the undifferentiated phenotype, hESC were induced to spontaneous differentiate either by EB formation or FGF-2 starvation.

4.3.1 A1 binding and cytotoxicity on differentiated hESC via EB formation

EB are three-dimensional aggregates derived from undifferentiated hESC. Homophilic binding of highly expressed Ca^{2+}-dependent adhesion molecule E-cadherin facilitates EB formation. Cells within EB undergo spontaneous differentiation and cell specification along the three germ lineages: endoderm, ectoderm, and mesoderm[108].

Human ESC-derived EB at different stages of spontaneous differentiation (day 2, day 5, day 8, and day 15) were harvested for flow cytometry analysis. By co-staining undifferentiated hESC and differentiating cells with A1 and pluripotency marker antibody, anti-TRA-1-60, we found that A1 binding on cells was down-regulated along with the loss of cell pluripotency (Figure 4-3A). At the same time, cell viability upon A1 treatment was assessed via PI uptake. We observed a complete loss of A1 cytotoxicity on differentiating cells from day 5 onwards (Figure 4-3B), indicating that A1 cytotoxicity might be an earlier indicator of cell differentiation than the expression level of pluripotency marker, Tra-1-60.

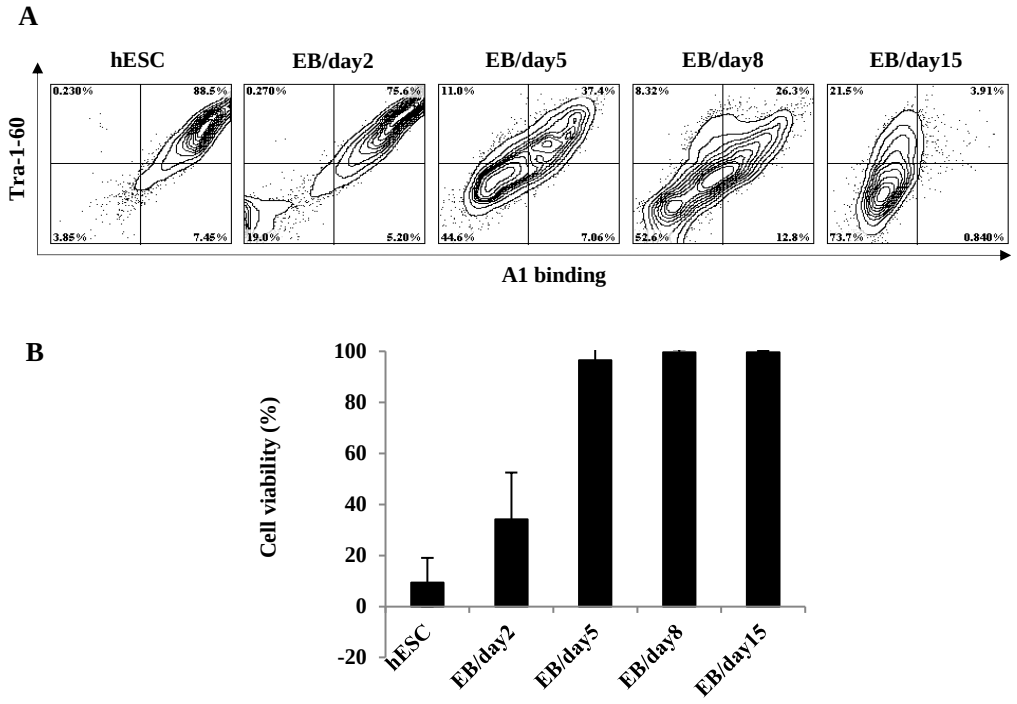

Figure 4-3: A1 loss binding and cytotoxicity on hESC-derived EB.
Cells (2 x 10^5 in 100 µl) were treated with 5 µg of A1 for 45 minutes at 4°C. (A) Loss of A1 binding is correlated with loss of pluripotency on spontaneously differentiated EB. Cells were dual-stained with A1 and antibody to pluripotency marker, anti-Tra-1-60. Representative scatter plots are shown. (B) A1 cytotoxicity on undifferentiated hESC and hESC-derived EB at different stages of spontaneously differentiated. Cell viability was assessed via PI uptake by flow cytometry analysis. Data are represented as mean ± SEM.

4.3.2 A1 binding and cytotoxicity on differentiated hESC via FGF-2 starvation

Alternatively, since FGF-2 is important for maintaining hESC pluripotency[84], hESC were induced to differentiate via FGF-2-starvation. A similar trend was observed though down-regulation of A1 binding and cytotoxicity was much slower (Figure 4-4). Taken together, we conclude that the binding and cytotoxicity of A1 is only specific to undifferentiated hESC. The ability of A1 to selectively kill undifferentiated hPSC is beneficial for the use of A1 to remove residual undifferentiated hPSC from differentiated cell products prior to therapeutic applications.

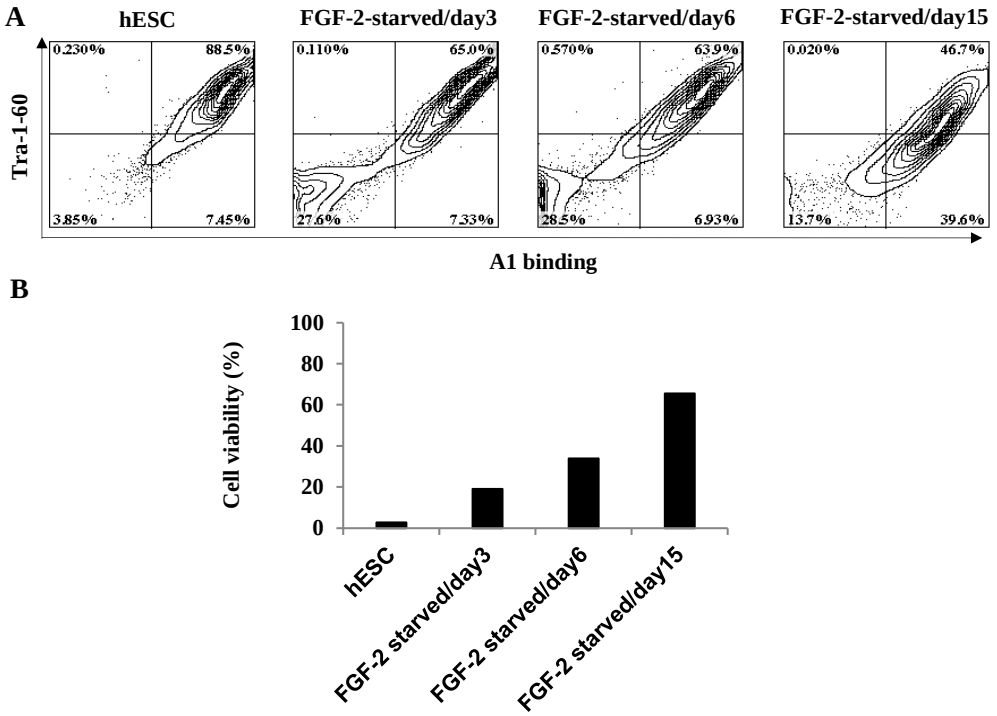

Figure 4-4: A1 loss binding and cytotoxicity on differentiated hESC via FGF-2 starvation.
Cells (2 x 10^5 in 100 µl) were treated with 5 µg of A1 for 45 minutes at 4°C. (A) Loss of A1 binding is correlated with loss of pluripotency on FGF-2-starved cells. Cells were dual-stained with A1 and antibody to pluripotency marker, anti-Tra-1-60. Representative scatter plots are shown. (B) A1 cytotoxicity on undifferentiated hESC and differentiated cells at different stages of FGF-2 starvation. Cell viability was assessed via PI uptake by flow cytometry analysis. Data are represented as mean ± SEM.

4.4 A1 cytotoxicity on hESC is dosage-dependent

Next, flow cytometry analysis was performed to investigate the effect of dosage on the cytotoxicity of A1, benchmarking to mAb84. The concentration of A1 was titrated over the range of 0.78-10 µg for 2 x 10^5 hESC in a volume of 100 µl for 45 minutes incubation at 4°C. Cell viability was assessed by PI uptake. We found that A1 has a dosage-dependent cytotoxicity towards hESC up to 5 µg (Figure 4-5), similar to mAb84. Further increase in mAb concentration (up to 10 µg) did not result in addition enhancement of cytotoxicity. There was no cell survived upon re-plating the cells back in CM and incubated over 48 hours, indicating the remaining 20% cells were dead as well.

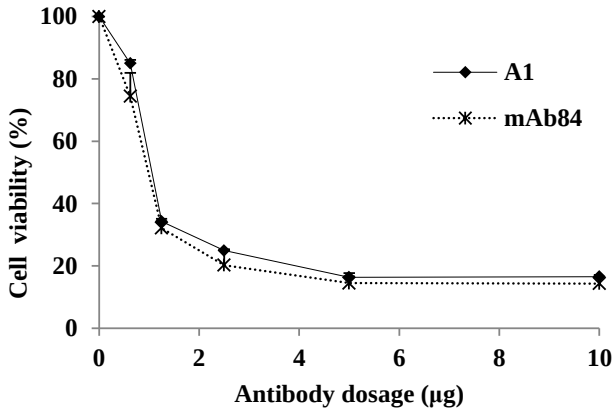

Figure 4-5: A1 cytotoxicity on hESC is dosage-dependent.
Human ESC (2 x 10^5 in 100 µl) were treated with different amount of A1 or mAb84 for 45 minutes at 4°C. Cell viability was assessed via PI uptake. Data are represented as mean ± SEM.

4.5 Kinetics of A1 killing on hESC

Next, we examined the kinetics of A1 killing. In this time course study, cells (2 x 10^5 in 100 µl) were treated with 5 µg of A1 or mAb84 at 4°C. PI uptake was measured after the first minute of incubation and every 5 minutes thereafter. A1 killing of hESC occurred rapidly with an 80% drop in hESC viability within 1 minute of A1 treatment (Figure 4-6). Extended incubation did not lead to further decrease in cell viability. There was no cell survived upon re-plating the cells back in CM and incubated over 48 hours, indicating the remaining 20% cells were dead as well.

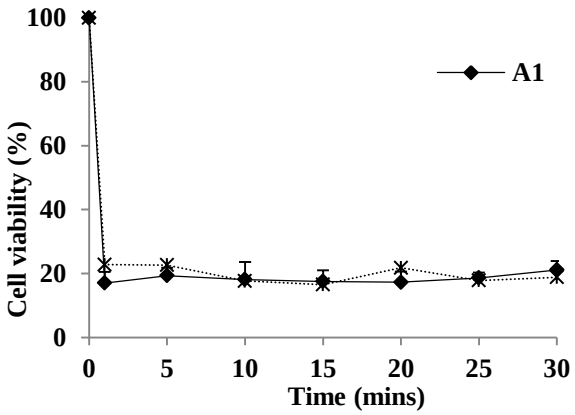

Figure 4-6: A1 kill hESC rapidly within 5 minutes of incubation.
Human ESC (2 x 10^5 in 100 µl) were treated with 5 µg of A1 or mAb84 for different time periods at 4°C. Cell viability was assessed via PI uptake. Data are represented as mean ± SEM.

4.6 Kinetics of A1 killing on hESC is not dosage-dependent

Based on the result of A1 kinetics study shown in Figure 4-6, A1 killing occurs at a very fast rate. In an attempt to slow down the rate of cell killing to facilitate time-lapse imaging, we investigated if the dosage of mAb affected the kinetics of A1 killing. Cells were treated with various dosages of A1 and cell viability was estimated at 10-minute intervals. Surprisingly, regardless of the dosage of A1, most of the cell killing was achieved within the first 10 minutes of incubation (Figure 4-7A). The assay was repeated however only focusing on the first 10 minutes with the middle three A1 dosages. Cell viability was assessed at 2-minute intervals. Most of the killings were still achieved within the first minute (Figure 4-7B). Therefore, it is difficult to slow down the killing process by reducing antibody dosage, as it only reduced the killing efficiency.

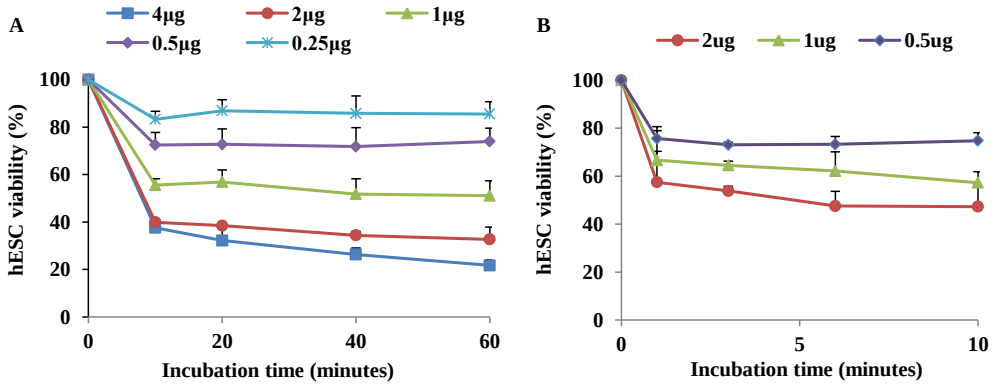

Figure 4-7: kinetics of A1 cytotoxicity on hESC is not dosage-dependent.
(A) Cells (2 x 10^5 in 100 µl) were treated with various dosages of A1 from 0.25 µg to 4 µg at 4°C and cell viability was assessed by PI uptake at every 10 minutes. (A) Cells (2 x 10^5 in 100 µl) were treated with various dosages of A1 from 0.5 µg to 2 µg at 4°C and cell viability was assessed by PI uptake at every 2 minutes. Data are represented as mean ± SEM.

4.7 Identification of A1 antigen target on hESC

Identification of the antigen target is not only important for the characterization of a mAb, but also crucial for understanding the interaction

between the mAb and the target cell. Therefore, to characterize A1 and study A1-induced hPSC death, we examined its target antigen on hESC.

4.7.1 A1 binds to glycoproteins on hESC

Target antigens were enriched from total hESC lysate by immuno-precipitation (IP) using A1 as the capture mAb. When the IP eluate was resolved on SDS-PAGE and immunoblotted with A1 after western blotting, it revealed a smear from 35-200 kDa (Figure 4-8A), whereas the antigen of mAb84 is a single protein band identified as PODXL[37]. The corresponding bands on a silver-stained gel were excised and analysed by mass spectrometry (MS). By mapping MS results with Uniprot Protein Database, strong antigen candidates were selected and can be divided into four protein groups (Figure 4-8B): cell adhesion proteins, cytoskeleton-associated proteins, ATPase proteins and transporter proteins. Intriguingly, over 70% of the antigen candidates are glycoproteins.

Glycoproteins are proteins with oligosaccharide chains (glycans) covalently attached to polypeptide side-chains via post-translational modification. A smeared antigen band and high percentage of glycoproteins in the MS result suggest that A1 is recognizing glycans on target antigens. Hence, to investigate whether A1 binding on hPSC is dependent on glycans, immuno-precipitated antigens were resolved by gel electrophoresis, western blotted and treated with sodium periodate to open existing sugar rings[109] followed by immunoblotting with A1. Comparing to the non-treated control, A1 binding to the entire smear was abolished after periodate-treatment of the blot (Figure 4-8A). This demonstrated that A1 binds to surface glycans on the target antigens.

A

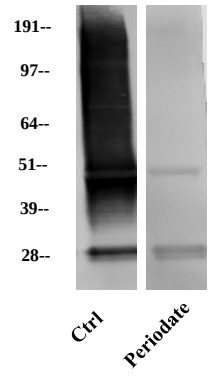

B

	Glycoproteins	Non-glycoproteins
Cell adhesion proteins	PODXL, integrin α-6/α-5/α-1, integrinβ-1/β-5, SorLA-1, CD44, Protocadherin-1, Na/H exchanger, CD166, Neuroligin-4, Laminin γ-1, Neuroplastin, CD239, CD326, CD56, CD36, Cell adhesion molecule 1, CD111, CD113, Calsyntenin-1	Tubulin-specific chaperone D, Catenin α-1/β -1/Δ-1,
Cytoskeleton-associated proteins	Trans-Golgi network integral membrane protein 2, Prominin-1, Syndecan-1, Plexin-B2, CD100, Leucine-rich repeat neuronal protein 1	KIF 11/12, Dynamin-2, Alpha-actinin-1, NHERF-1, TCP-1-epsilon, TCP-1-delta, Filamin B
ATPase proteins	Na/K-transporting ATPase α-1/α-2/α-3/β-3, ATP5F1, CD340, E-NPP 1, Tyrosine-protein kinase Kit, CD331	SR Ca(2+)-ATPase 2, LACS 3, Hexokinase-1, V-ATPase subunit A, CTP synthase 1, PFK-A
Transporter proteins	CD98, GLUT-3, GLUT-2, GLUT-1, Sodium bicarbonate cotransporter 3, MRP46, K-Cl cotransporter 4, LTC4 transporter, Zinc transporter ZIP14, MOAT-C, MOAT-B, NPC1, SLC12A4, SLC5A6, Potassium-chloride transporter 9	MCT-1, Alpha-adaptin C, Beta-1-adaptin, Beta-COP, Alpha-COP, Gamma-2-COP, Exportin-2

Figure 4-8: A1 binds to multiple glycoproteins on hESC.
(A) A1 binds to glycans on multiple target antigens on hESC. Affinity purified A1 antigens from hESC lysate were resolved on SDS-PAGE, transferred to PVDF membrane, subjected to sodium periodate treatment and immunoblotted with A1. (B) Protein IDs were identified by mapping peptides from mass spectrometry analysis against the Homo sapiens subset of the Uniprot database. Antigen candidates were selected with the following filter settings: match score above 4, peptide coverage above 5, unique number of peptides above 1, and location of protein: membrane.

4.7.2 A1 recognizes O-linked glycans on target antigens

Glycans are attached to proteins via glycosylation. In general, there are two major types of glycosylation, namely, N-glycosylation and O-glycosylation. N-glycosylation attaches glycans to the nitrogen of asparagine or arginine side-chains[110], whilst O-glycosylation attaches glycans to the hydroxyl oxygen of serine, threonine, tyrosine, hydroxylysine, or hydroxyproline side chain[111]. O-glycosylation usually occurs at a later stage during protein synthesis. In

addition, sialic acid, a monosaccharide with nine-carbon backbone, is typically found to be terminating branches of N-linked glycans and O-linked glycans[112]. Next, the type of glycans that A1 recognizes was investigated. Affinity enriched A1 antigens were sequentially digested with sialidase, N-glycosidase F (PNGase F) and β-elimination. Sialidase can effectively hydrolyse the glycosidic linkage of terminal sialic residues in glycoproteins[113]. Removal of terminal sialic acid can expose N-linked and O-linked glycans. PNGase F releases N-linked glycans by cleaving the link between asparagine and N-acetylglucosamines[114]. β-elimination removes O-linked glycans attached on serine and threonine residues from glycoproteins in the reduced form[115]. Samples were taken from each enzymatic digestion and immunoblotted with A1. Based on Figure 4-9, A1 recognizes non-sialylated glycans since sialidase treatment did not alter A1 binding (lane 1 vs lane 2). A1 did not bind to antigens in the size range of 35-50 kDa and 60-90 kDa upon β-elimination treatment alone (as highlighted in dashed gate from lane 5 to lane 8), indicating A1 recognizes O-linked glycans on these antigens. Upon both PNGase F and β-elimination treatment, A1 also did not bind to antigens in the size range of 90-200 kDa (as highlighted in dotted gate at lane 7 and 8). However, since certain O-linked glycans can only be removed upon N-deglycosylation[115], it was insufficient to conclude whether N-linked glycans are also associated with A1 binding to hPSC.

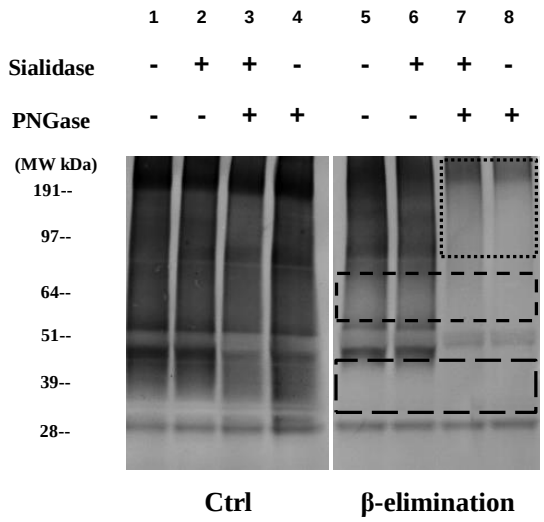

Figure 4-9: A1 recognizes O-linked glycans on target antigens from hESC lysate.
Affinity purified A1 antigens from total hESC lysate were treated sequentially with sialidase and PNGase F, resolved on SDS-PAGE, transferred to PVDF membrane, subjected to β-elimination, and immunoblotted with A1. Dotted gate represents loss of A1 binding upon both PNGase F and β-elimination treatment; dashed gate represents loss of A1 binding upon β-elimination treatment alone.

To verify whether A1 is also recognizing N-linked glycans and whether binding to O-linked glycans is associated with A1 killing on hESC, two glycosylation inhibitors, namely tunicamycin[116] and Benzyl-α-GalNac (B-GalNac)[117], were used to inhibit N-glycosylation and O-glycosylation respectively in hESC culture. Tunicamycin blocks the formation of protein N-glycosidic linkages by inhibiting the transfer of N-acetylglucosamine 1-phosphate to dolichol monophosphate[116]. B-GalNac is an O-GlcNAc (OGT) transferase inhibitor which blocks the incorporation of glucosamine into O-linked glycans[117].

Four days after passaging, hESC in culture were spiked with optimized amount of inhibitors in CM and incubated for 24 hours. For the negative control, hESC were fed with CM or CM with the same volume of DMSO as the inhibitors. After incubation, hESC were harvested in single-cell suspension for flow cytometry analysis. Firstly, the removal of N-linked glycans and O-

linked glycans upon inhibitor treatment were verified. Concanavalin A (ConA), a lectin which binds specifically to N-linked glycans[118], was used to verify the removal of N-linked glycans from hESC upon tunicamycin treatment. Tra-1-60 is a pluripotency marker of hESC. Since the epitope of Tra-1-60 antibody is attached on an O-linked glycan core, Tra-1-60 antibody was used to verify the removal of O-linked glycans from hESC upon B-GalNac treatment[119].

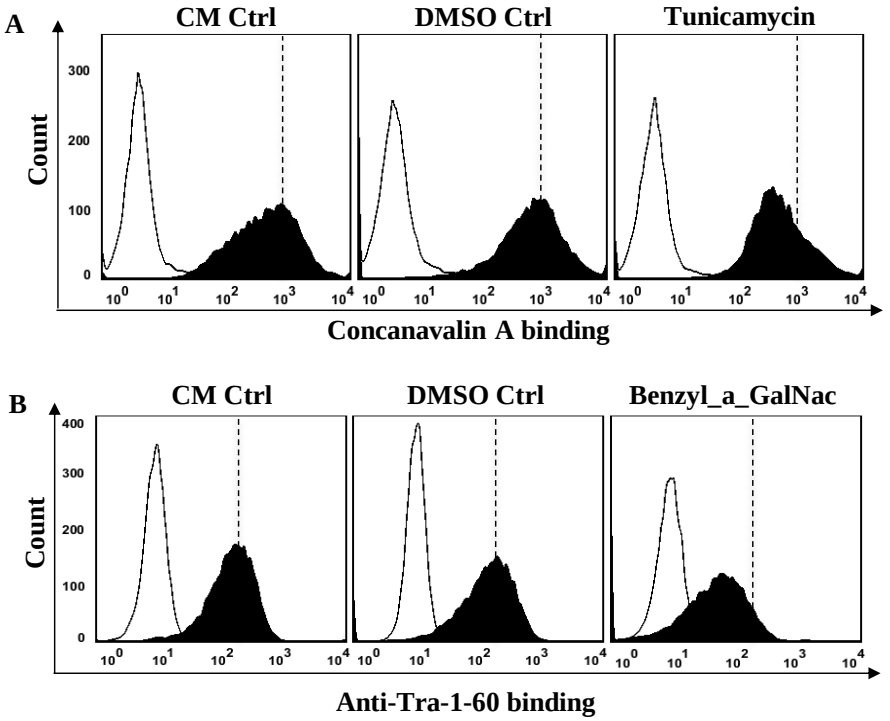

Figure 4-10: Partial inhibition of N-glycosylation and O-glycosylation by tunicamycin and Benzyl-α-GalNac treatment.
Benzyl-α-GalNac (4 mM, 24 hours) and tunicamycin (5 μg/ml, 24 hours) were used to inhibit O-glycosylation and N-glycosylation in hESC culture respectively. (A) Tunicamycin treatment partially blocked N-glycosylation in hESC culture. Upon tunicamycin treatment, down-regulation of N-glycosylation was detected by a decreased binding of Concanavalin A (ConA), a lectin which binds specifically to N-linked glycans[118]. (B) Benzyl-α-GalNac treatment partially blocked O-glycosylation in hESC culture. Upon Benzyl-α-GalNac treatment, down-regulation of O-glycosylation was detected by a decreased binding of anti-Tra-1-60 antibody which binds to O-linked glycan epitopes on hESC[119]. Lectin or antibodies bound to cells were detected with a FITC-conjugated streptavidin or anti-mouse antibody. Representative histograms are shown. The shaded histogram represents staining with the negative control and open histograms represent staining with primary antibodies.

In Figure 4-10, it was observed that both the binding of ConA and Tra-1-60 antibody to inhibitor-treated hESC were down-regulated compared to the

negative controls, suggesting both N-glycosylation and O-glycosylation were partially inhibited with the inhibitor treatments.

Since there is a decrease in anti-Tra-1-60 antibody binding to hESC, we continued to confirm this decrease was not due to loss of hESC pluripotency after inhibitor treatment. Among the most frequently monitored hESC pluripotency markers (Tra-1-60[119], SSEA4[120], Oct3/4), only the antibody to Oct3/4 is not recognizing a glycan epitope on hESC. Therefore, the expression level of Oct3/4 was examined upon inhibitor treatment. There is no significant change in the binding of Oct3/4 antibody to either tunicamycin or B-GalNac treated hESC compared to the CM control or the DMSO control (Figure 4-11), indicating that inhibitor treatment did not inhibit pluripotency marker (Oct3/4) expression.

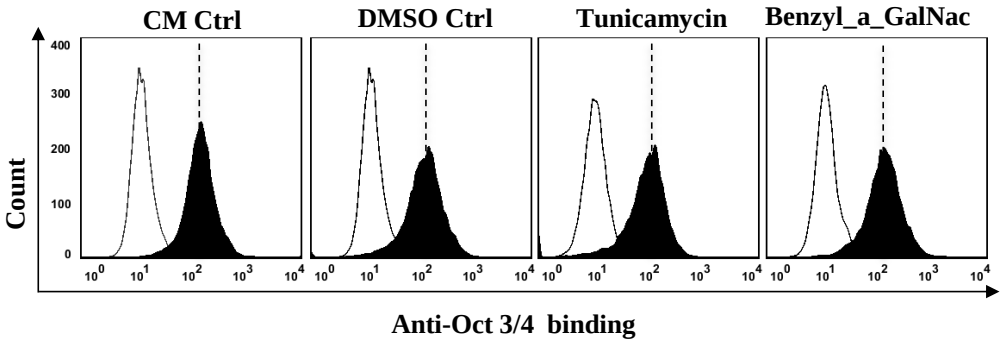

Figure 4-11: Expression of pluripotency marker, Oct3/4, was verified upon inhibitors treatment.
Cells in different treatment conditions were stained with mAb to Oct3/4 or PBS- control. Antibodies bound to cells were detected with a FITC-conjugated anti-mouse antibody. The shaded histogram represents staining with the negative control and open histograms represent staining with primary antibodies. Upon either tunicamycin treatment or B-GalNac treatment, the binding histograms of Oct3/4 antibody are comparable to these of negative controls, representing no change in hESC pluripotency upon inhibitors treatment.

With successful partial inhibition of both N- and O-glycosylation on hESC while maintaining hESC pluripotency, we proceeded to investigate the binding and killing of A1 on hESC. After 24 hours of treatment with the inhibitors,

hESC were harvested as single-cell suspension (2 x 10^5 in 100 μl) and treated with 5 μg of A1 or PBS- for 45 minutes at 4°C. A1 binding and killing on hESC were assessed by flow cytometry analysis. It was observed that A1 binding to hESC was down-regulated upon B-GalNac treatment, but not tunicamycin treatment, indicating A1 only binds to O-linked glycans on hESC, but not N-linked glycans (Figure 4-12). This finding further confirmed the previous conclusion from PNGase and β-elimination experiment.

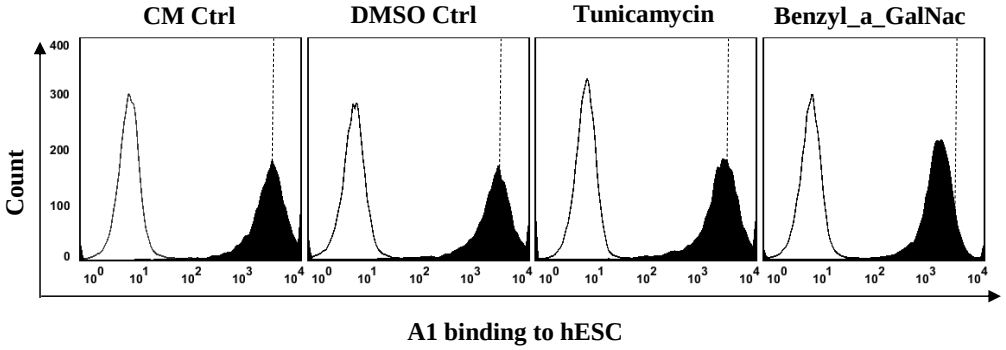

Figure 4-12: A1 binding to hESC was down-regulated upon B-GalNac treatment
Benzyl-α-GalNac (4 mM, 24 hours) and tunicamycin (5 μg/ml, 24 hours) were used to inhibit O-glycosylation and N-glycosylation in hESC culture respectively. Cells in different treatment conditions were incubated with A1 or PBS-. Binding of A1 was assessed with FITC-conjugated secondary antibody by flow cytometry analysis. Representative histograms are shown. Open histogram represents no treatment control and shaded histogram represents antibody-treated cells. Upon B-GalNac treatment, the binding histograms of A1 shifted towards to the left compared to these of negative controls and tunicamycin treatment, representing A1 binding is only down-regulated when O-glycosylation is inhibited.

At the same time, cell viability upon B-GalNac treatment was significantly higher than the CM-control, DMSO-control and tunicamycin treatment (Figure 4-13), indicating binding to O-linked glycans is essential for A1 to elicit cytotoxicity on hESC.

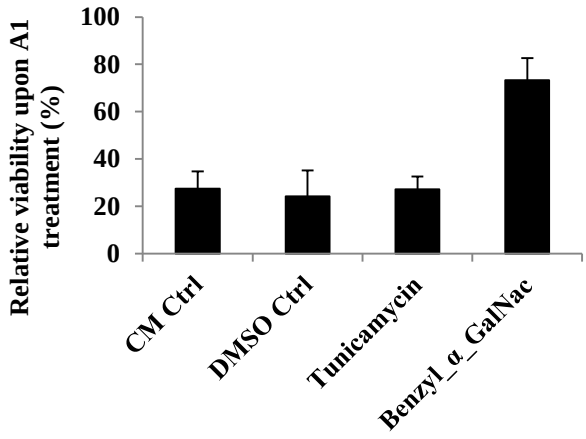

Figure 4-13: A1 cytotoxicity on hESC was down-regulated upon B-GalNac treatment
Benzyl-α-GalNac (4 mM, 24 hours) and tunicamycin (5 μg/ml, 24 hours) were used to inhibit O-glycosylation and N-glycosylation in hESC culture respectively. Cells in different treatment conditions were harvested in single-cell suspension and treated with A1 or PBS-. Viability of cells was estimated by PI uptake. Cell viability in different treatment conditions was normalized to its corresponding negative controls (no A1 treatment). Upon B-GalNac treatment, cell viability upon A1 treatment was significantly higher than these of negative controls (CM control and DMSO control) as well as tunicamycin treatment. Data are represented as mean ± SEM.

Since maintaining hESC in a pluripotent state is crucial to the experiment, here we further investigated whether hESC treated with glycan inhibitor remained pluripotent, i.e., able to be differentiated into cells of the three germ layers: endoderm, mesoderm and ectoderm. To test this, hESC either treated with DMSO or Benzyl-α-GalNac (4 mM or 8 mM) for 24 hours were passaged for spontaneous differentiation as EB. Cells were harvested at two time points: undifferentiated hESC and EB on day 7. Total mRNA was extracted from harvested cells for quantitative real-time PCR (qRT-PCR) analysis. RNA expression levels of markers for pluripotency, endoderm, mesoderm and ectoderm were normalized against endogenous control, RNA levels of GAPDH.

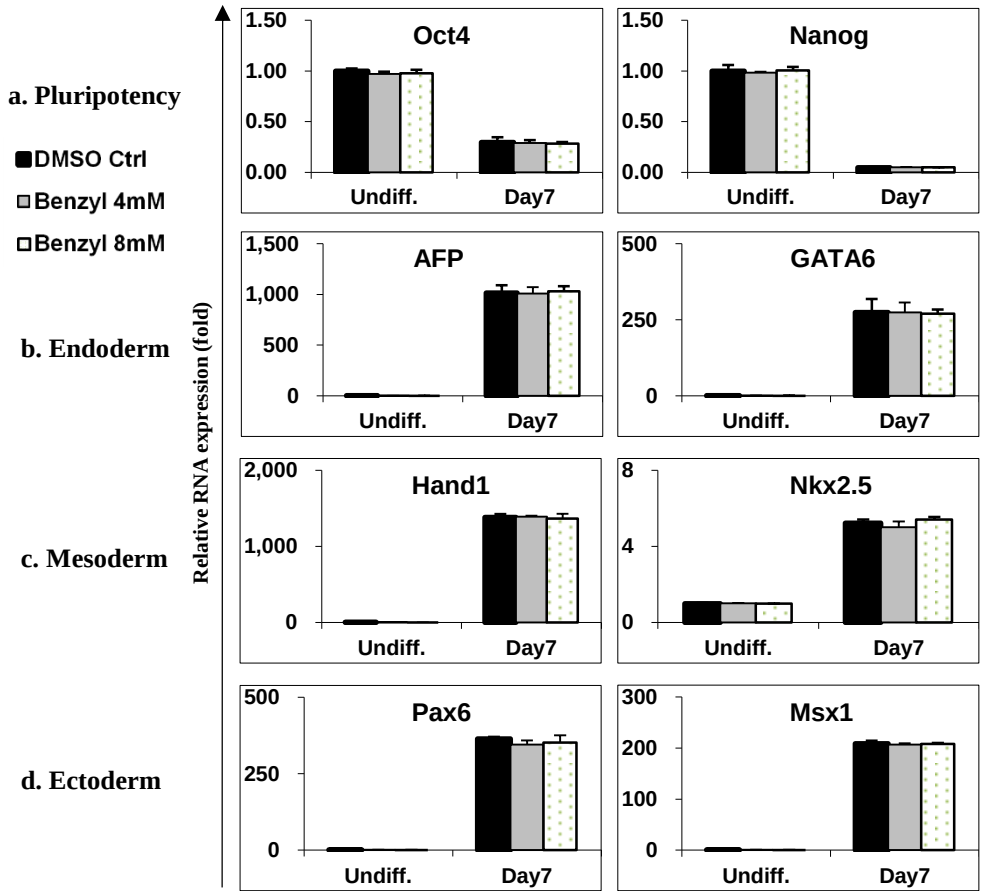

Figure 4-14: There is no difference in the relative RNA expression level of listed markers between DMSO control and B-GalNac treatment.
Relative mRNA expression levels of pluripotency markers (Oct4, Nanog) and markers for the three germ layers (Endoderm: AFP, GATA6, Mesoderm: Hand1, Nkx2.5; Ectoderm: Pax6, Msx1). Data are represented as mean ± SEM.

According to Figure 4-14, there was no significant difference in RNA expression level of markers for pluripotency and markers for the three germ layers between DMSO treatment of B-GalNac treatment. As expected, undifferentiated hESC had the highest expression level of pluripotency markers, Oct4 and Nanog, and lowest expression levels of germ layer markers, indicating cells were highly pluripotent. On Day7, expression of all six germ layer markers significantly increased whereas expression of pluripotency markers decreased drastically. All these observations confirmed that B-GalNac treatment did not affect the pluripotency of hESC.

4.7.3 A1 binds to epitope containing sugar motif (Fucα1-2Galβ1-3GlcNAcβ1-3Galβ1) on hPSC antigens

To determine the glycan epitope that A1 recognizes on hPSC, A1 binding and cytotoxicity on hESC was examined after pre-incubation with nine sugars of the non-sialylated blood group antigens, namely, type-1 H (H1), type-2 H (H2), Lacto-N-fucopentaose I (LNFP1), type-1 A (bgA), type-1 B (bgB), LNFP1, LewisA, LewisB, LewisX, and LewisY (Figure 4-15), separately for 30 minutes before incubation with hESC for 45 minutes.

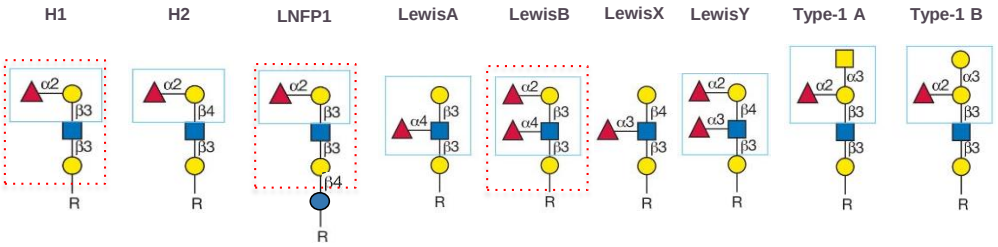

Figure 4-15: Structures of the nine sugars used in the sugar inhibition assay[121].
The sugar motif (Fucα1-2Galβ1-3GlcNAcβ1-3Galβ1-) that may be part of the A1 binding epitope in H1, LNFP1 and Lewis B is highlighted in red box.

Upon pre-incubation with different sugars, A1 binding on hESC as well as hESC viability was assessed by flow cytometry analysis. A decrease in A1 binding on hESC was observed upon pre-incubation with H1, LNFP1 and LewisB (Figure 4-16), indicating a binding competition between these three sugars and the epitope on hESC for A1. Among the nine sugars, H1, LNFP1 and LewisB share a common sequence of four monosaccharide and their linkages (Figure 4-15), suggesting A1 recognizes this glycan motif (Fucα1-2Galβ1-3GlcNAcβ1-3Galβ1-) on hESC antigens.

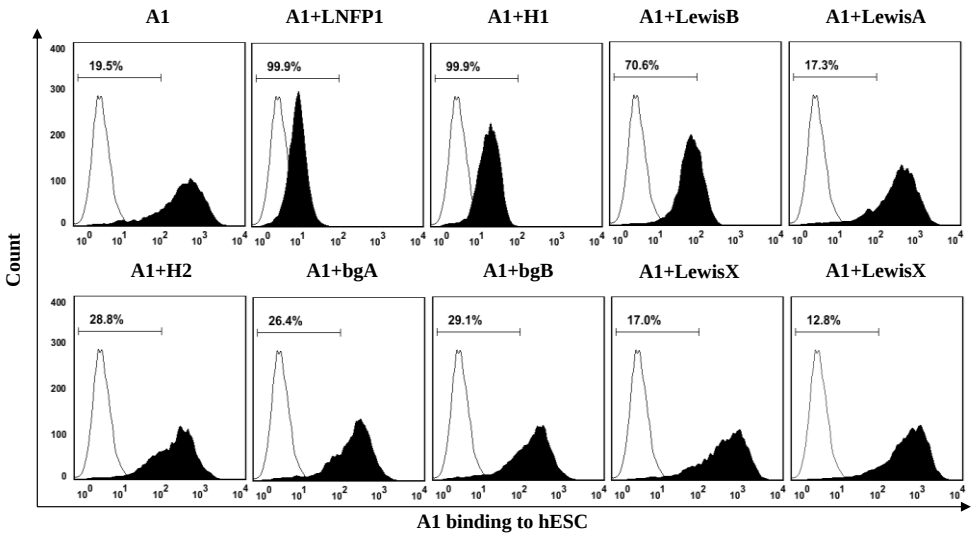

Figure 4-16: A1 binding on hESC was blocked by LNFP1, H1 and LewisB.
A1 (5 μg) was pre-incubated with the nine different sugars (2 mM) prior to treatment with 2 x 10^5 cells (100 μl) for 45 minutes at 4°C. Binding of A1 was assessed with FITC-conjugated secondary antibody by flow cytometry analysis. Representative histograms are shown. Open histogram represents no treatment control and shaded histogram represents antibody-treated cells.

Next, the specific antigen or antigens bands that are blocked by the three sugars were investigated. Immuno-precipitated antigens were resolved by gel electrophoresis and immuno-blotted with sugar-blocked A1. As a result, most of the antigens in the A1 control-blotted membrane were not detected in the other three blots (Figure 4-17).

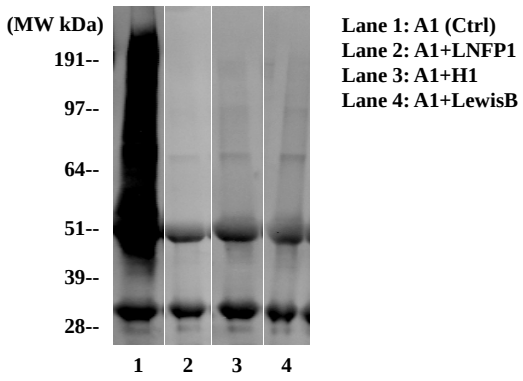

Figure 4-17: Binding profile of sugar-blocked A1 on hESC.
Affinity purified A1 antigens from hESC lysate were resolved on SDS-PAGE, transferred to PVDF membrane, and immunoblotted with A1 or sugar-blocked A1.

From the same sugar inhibition assay, it was further observed that upon pre-incubation with these three sugars, A1 cytotoxicity on hESC was abolished (Figure 4-18), indicating that A1 cytotoxicity on hESC depends on its binding to the glycan motif (-Fucα1-2Galβ1-3GlcNAcβ1-3Galβ1-). Taken together, we conclude that A1 binds to an O-linked glycan epitope containing the sugar motif (-Fucα1-2Galβ1-3GlcNAcβ1-3Galβ1) to elicit cytotoxicity on hPSC.

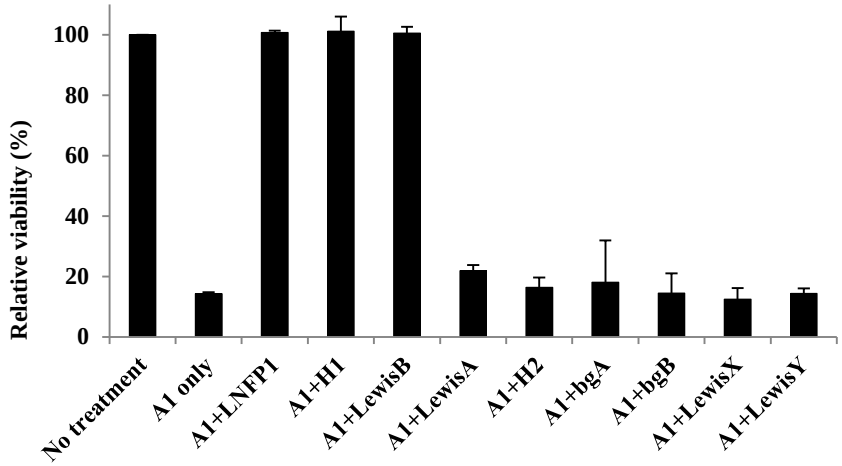

Figure 4-18: A1 cytotoxicity on hESC was blocked by LNFP1, H1 and LewisB.
A1 (5 μg) was pre-incubated with the nine different sugars (2 mM) prior to treatment with 2 x 10^5 cells (100 μl) for 45 minutes at 4°C. Cell viability was assessed via PI uptake. Data are represented as mean ± SEM.

4.8 Amino acid sequences in A1 variable regions

To confirm that A1 and mAb84 are different antibodies despite both mAbs displaying similar cytotoxic effect on hESC, the amino acid sequence of mAb heavy and light variable regions was deduced via nucleotide sequencing of the hybridomas. As expected, differences in amino acid sequences between A1 and mAb84 were observed in the variable regions, more specifically, the complementarity determining regions (CDRs) (Figure 4-19). CDRs are hypervariable domains of antibodies that determine the specificity of antibody binding. In the heavy chain variable regions, there are four different amino acids in all three CDRs (Figure 4-19A); and in the light chain variable regions,

there are also four different amino acids in all three CDRs (Figure 4-19B). Hence, A1 and mAb84 are different antibodies.

A

```
mAb84_Heavy_Chain  QVQLQQSGGGLVQPGGSMKLSCVASGFTFSNYWMNWVRQSPEKGLEWVAEIRLKSNNYAT
A1_Heavy_Chain     QVKLQQSGGGLVQPGGSMKLSCVASGFTFSNYYMNWVRQSPEKGLEWVAEIRLKSNNYAT

mAb84_Heavy_Chain  HYAESVKGRFTISRDDSKSSVYLQMNNLRAEDTGIYYCTGERAWGQGTTVTVSS
A1_Heavy_Chain     HYAESVKGRFTISRDDSKSSVYLQMNNLRAEDTGIYYCEGFGYWGQGTTVTVSS
```

B

```
mAb84_Light_Chain  DIELTQSPAIMSASPGEKVTMTCSASSSVNYMYWYQQKPGSSPRLLIYDTSNLASGVPVR
A1_Light_Chain     DIELTQSPALMSASPGEKVTMTCSASSSVSYMFWYQQKPRSSPKPWIHLTSNLASGVPAR

mAb84_Light_Chain  FSGSGSGTSYSLTISRMEAEDAATYYCQQWSSYPYTFGGGTKLEIKR
A1_Light_Chain     FSGSGSGTSYSLTISSMEAEDAATYYCQQWSSNPYTFGGGTKLEIKR
```

Figure 4-19: Differences in the CDRs amino acids sequences between A1 and mAb84.
(A) Heavy chain sequences of A1 and mAb84. (B) Light chain sequences of A1 and mAb84. CDRs are highlighted in red. Differences in amino acids between A1 and mAb84 were underlined.

4.9 Competitive inhibition between mAb84 and A1

Since both mAb84 and A1 can bind to and kill hESC in a similar manner, we next investigated whether they are binding to the same epitope on hESC using a competitive inhibition assay. Cells (2×10^5 in 100 µl) were treated with 5 µg of A1 or mAb84 at 4^oC simultaneous or sequentially. A1 was labelled with FITC and mAb84 was labelled with APC. Figure 4-20 shows the readout of FITC and APC signal, which represents the binding of mAbs to hESC. We observed that regardless whether the mAbs were added simultaneously or sequentially, the FITC and APC signals were as strong as their corresponding signals in the positive control (individual mAbs), indicating there is no competitive inhibition between the binding of mAb84 and A1 on hESC. Hence, A1 and mAb84 should be targeting different epitopes on hESC.

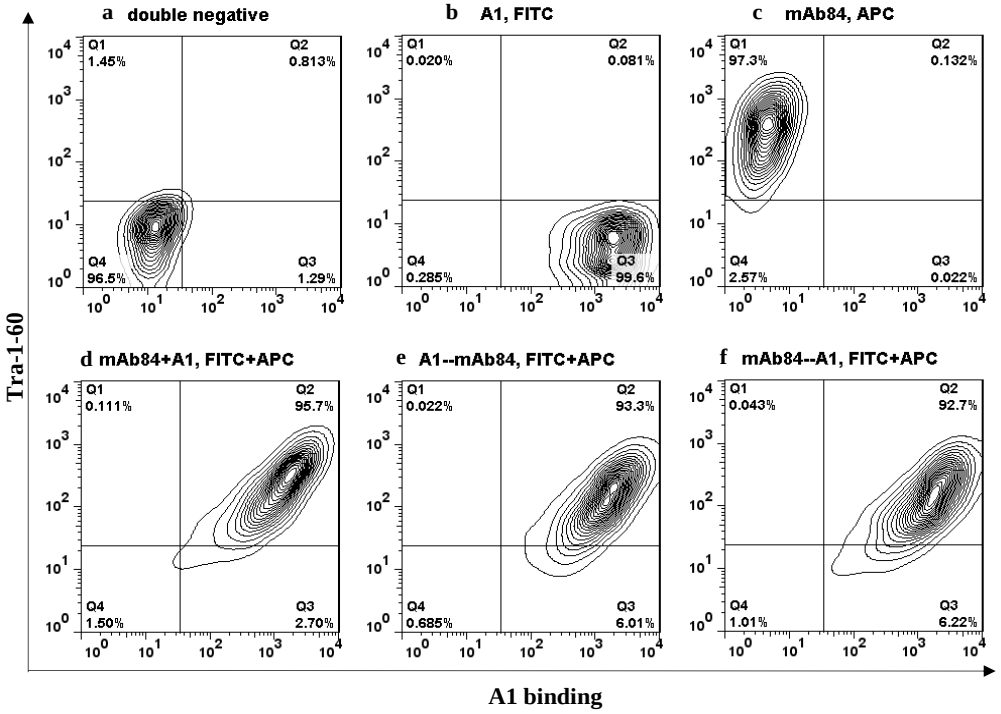

Figure 4-20: There is no competitive inhibition between A1 and mAb84.
(a) Double negative control without antibody treatment; (b) positive control for A1: cells were treated by A1 and labelled with FITC; (c) positive control for mAb84: cells were treated by mAb84 and labelled with APC; (d) cells were treated with A1 and mAb84 simultaneously; (e) cells were firstly treated with mAb84 preceding A1; (f) cells were firstly treated with A1 preceding mAb84.

4.10 A1 showed better penetration efficiency into EB than mAb84

Since A1 is five times smaller than mAb84 (150 kDa vs 850 kDa respectively), A1 is expected to have better penetration into tissue mass. To demonstrate this, the penetration efficiency of A1 and mAb84 into EB was investigated. EB derived from hESC on day 5 were incubated with the same amount (μg) of FITC-conjugated A1 or FITC-conjugated mAb84 for 4 hours at 4^{o}C. Subsequently, excess antibodies were washed off and the EB were cryo-sectioned and imaged with a fluorescence microscope. As shown in Figure 4-21A, mAb84 was mostly localised at the periphery of EB whereas A1 showed better penetration and distribution throughout the EB. Penetration efficiency of mAbs was estimated by the percentage of mean fluorescence intensity within EB over that of the entire EB. A1 showed significantly higher

penetration efficiency over mAb84 (Figure 4-21B). Hence, A1 is advantageous in eliminating residual undifferentiated hESC embedded within 3D aggregates of differentiated progenies.

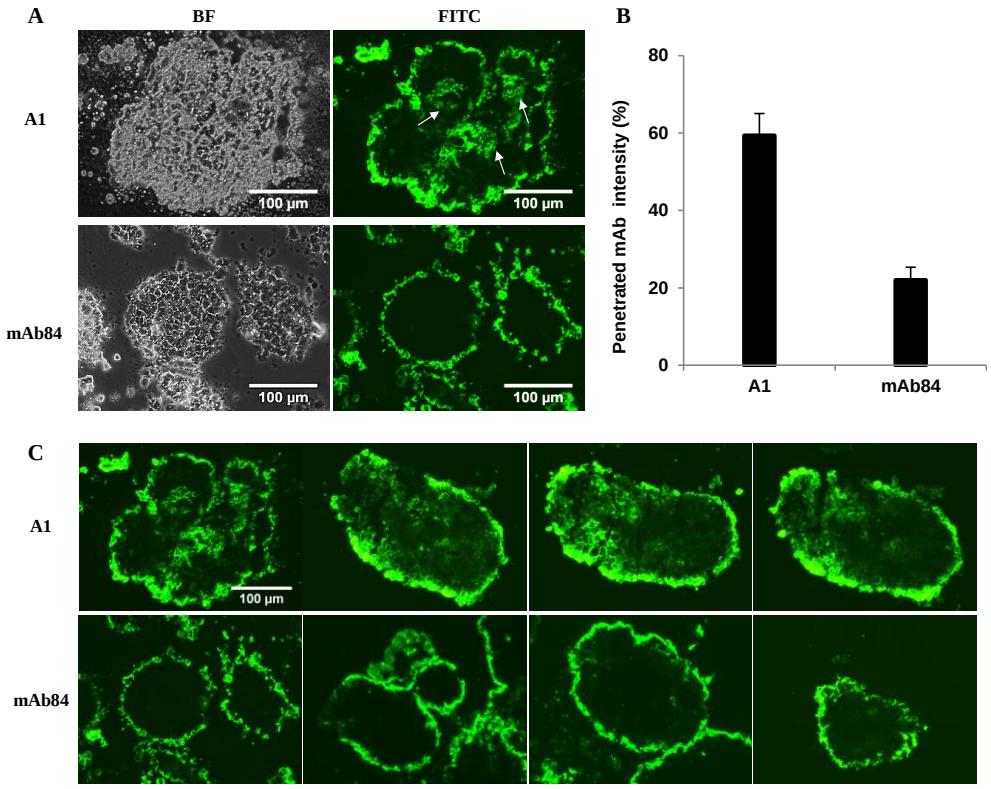

Figure 4-21: A1 showed better penetration efficiency into hESC-derived EB than mAb84.
(A) Fluorescence and bright field images of cryo-sectioned EB exposed to either FITC-conjugated A1 or FITC-conjugated mAb84. Arrows indicate penetrated A1. (B) Penetrated mAb intensity was calculated by comparing the mean fluorescence intensity within EB (about 20 µm from the edge) to the mean fluorescence intensity of the entire EB. Fluorescence intensity was measured by ImageJ. A1 had a significantly higher penetrated intensity compared to mAb84. Data are represented as mean ± SEM. (C) Images of EB that were used for the quantification.

4.11 Binding stoichiometry between A1 and hESC

It is clear that binding of A1 to hESC is a prerequisite for its cytotoxicity on hESC. However, the threshold number of bound A1 on hESC to elicit its cytotoxicity is unclear. Investigation of binding stoichiometry between A1 and hESC may help to better understand the binding profile as well as the correlation between antibody binding and killing.

This was achieved by estimating the number of A1 molecules that can bind to a single hESC upon saturation. Excess A1 was incubated with 2 x 10^5 hESC at 4^oC for 45 minutes and unbound A1 was separated in the supernatant. The amount of unbound A1 was measured by ELISA and used to estimate the number of A1 present on a single hESC. A brief illustration of ELISA working principle is shown in Figure 4-22. At the same time, viability of the cells in the pellet was estimated by PI uptake.

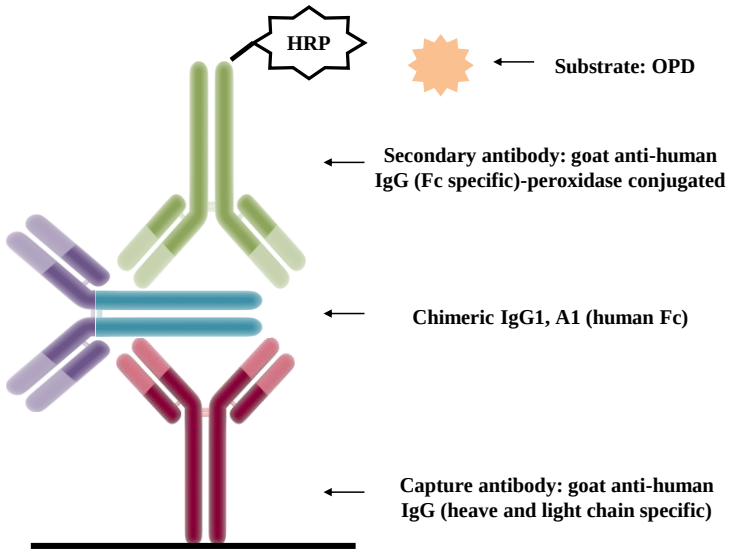

Figure 4-22: Brief illustration of the ELISA working principle.
Excess anti-human IgG (heavy and light chain specific) was used as the coating antibody to capture the chimeric IgG_1 A1 (human Fc). Subsequently, the secondary anti-human IgG (Fc specific) with peroxidase conjugated would bind to the chimeric IgG_1 A1 (Fc region) and the absorbance of an oxidized product from peroxidase-OPD reaction is measured at 492 nm with reference to 620 nm.

For ELISA, the absorbance values of all samples at 492 nm were normalized by their reference values at 620 nm. The relative absorbance value of the standard A1 was then plotted against its corresponding concentration to generate a standard curve (Figure 4-23). Based on the standard curve, the number of A1 molecules per hESC was estimated.

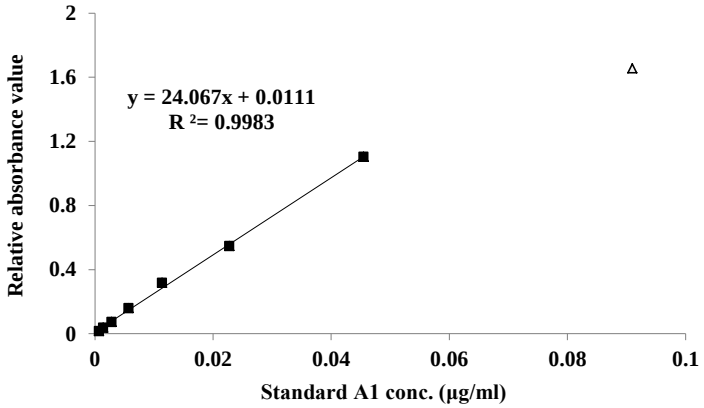

Figure 4-23: The standard curve of ELISA.
The standard curve was generated from the serial diluted IgG_1 A1 with known concentration. The equation of the regression line was then used to calculate the concentration of the unbound A1. The resulted concentration values were multiplied by their corresponding dilution factors and a mean value was taken to calculate the total amount of unbound A1 in the supernatant. Subsequently, the number of A1 that can bind to a single hESC was estimated using the equation in Figure 3-1. Data are represented as mean ± SEM.

In Figure 4-24, the number of A1 molecules as well as A1 killing was plotted against the initial amount of A1. It was observed that A1 binding and killing on hESC was saturated at the same point, where the initial amount of A1 is 3.64 µg, (Figure 4-24), indicating saturated binding is essential for maximum killing. At this point, there are about 2.93 x 10^7 A1 molecules on a single hESC.

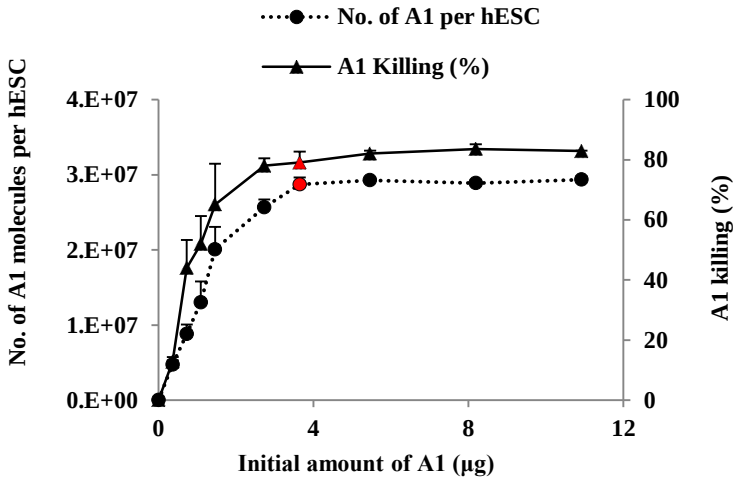

Figure 4-24: A1 binding and killing on hESC at different initial concentration.
Number of A1 molecules per hESC as well as A1 killing was plotted against the initial amount of A1. A1 killing was measured by PI uptake via flow cytometry. Data are represented as mean ± SEM. Point with saturated A1 killing and binding was highlighted in red.

Moreover, by comparing the amount of unbound A1 and bound A1 in the stoichiometry assay (Figure 4-25), it was clear that binding and killing is only saturated when the amount of A1 is significantly higher than the amount of bound A1, suggesting A1 binding is a dynamic and reversible process.

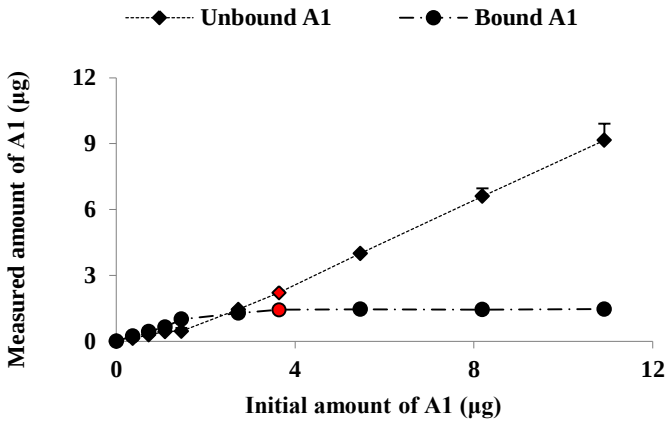

Figure 4-25: The relationship between the amount of unbound A1 and bound A1 in the stoichiometry assay and corresponding A1 killing on hESC at different initial amount of A1.
The amount of bound A1 was estimated by subtracting the difference between the initial amount of A1 by the amount of unbound A1. Point with saturated A1 killing was highlighted in red. Data are represented as mean ± SEM.

4.12 A1-induced hESC plasma membrane damage

The rapid killing effect and the PI uptake of A1-treated hESC suggest that A1 kills hESC via oncosis, which typically results in membrane pore formation. Therefore, the sizes of these pores were estimated with dextran beads of varying molecular weight. As mAb84 was reported to induce pore formation in hESC, it was used as a benchmark. In addition, an in-house antibody, mAb85, which binds to but do not kill hESC, was used as an isotype control.

Cells were incubated with A1, mAb84, mAb85, or PBS- followed incubation with fluorescent dextran beads. As a positive control, cells were fixed and permeabilized. The population of cells with high fluorescence was gated and the percentages are represented in Figure 4-26. Dextran beads of the three

different sizes (40 kDa, 70 kDa, 2000 kDa) were able to diffuse into A1-treated hESC and mAb84-treated hESC, leading to an increase in fluorescence level comparable to the fixed and permeabilized cells. In contrast, the fluorescence level of the negative control and mAb85 control is minimal, representing the background of dead cells. This data suggests that the pores formed on the plasma membrane were greater than 2,000 kDa in size, which is about 20 nm.

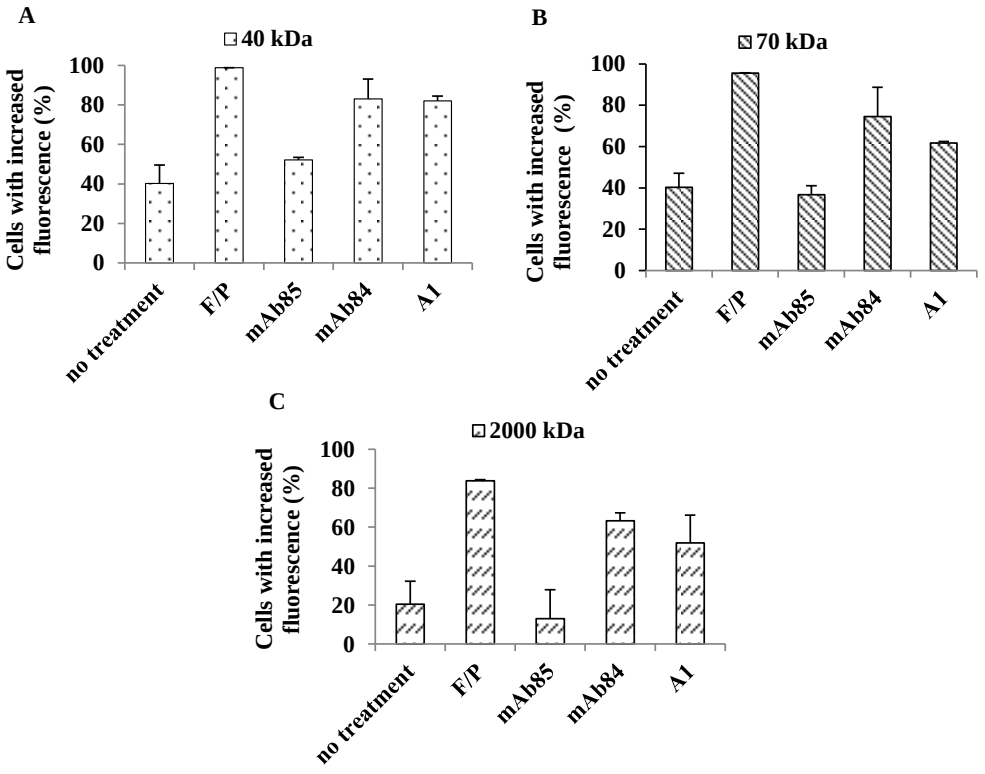

Figure 4-26: Determination of pore size with 40 kDa, 70 kDa and 2000 kDa dextran beads respectively.
Human ESC (2 x 10^5 in 100 µl) were treated with 5 µg of A1, mAb84, mAb85, or PBS- at 4°C Increase in intracellular fluorescence is correlated with the entry of dextran beads into the cells. Data are represented as mean ± SEM.

4.13 A1 cytotoxicity on hESC requires bivalency, but not Fc-domain

The valency of an antibody determines the number of antigens that an individual antibody can bind[122]. Non-engineered antibodies have at least two or more, termed as bivalent or multivalent. Engineering technologies have also

made monovalent antibody available[123]. Some studies have shown that antibodies with bivalency or multivalency have better functionality than their monovalent forms[124–126]. Won et al. has reported that the cytotoxicity of the bivalent ([Fab-SWn-PE38]$_2$) antibody-toxin against the CRL1739 cell line was 18.8-fold higher than that of the monovalent (Fab-SWn-PE38) antibody-toxins[124]. In the study on the effect of antibody valency on Fc gamma RI-mediated ADCC, Koolwijk et al. demonstrated that monovalently bound mAb has a significant decrease in cytotoxicity compared to bivalently bound mAb[125]. Another study also reported that only bivalent antibodies are capable of neutralizing Herpes simplex virus (HSV) since the neutralization capacity of this antibody is dependent on cross-linkage of antigen trimmers on the virus[126]. More relevant to this study, the cytotoxicity of mAb84 fragments was also only recapitulated by the multivalent scFv84-HTH but not Fab84[127]. However, bivalency of antibodies has also been reported to impede its functionality. According to Cobbold et al. [128], bivalent antibody binding would lead to antigenic modulation which allows cells to escape complement lysis or opsonizatioin by redistributing and eventually losing the antigen-antibody complexes from the cell surface[129]. Since IgG A1 is a bivalent antibody that binds and kills hESC, it was investigated if bivalency is essential for A1 to elicit its cytotoxicity on hESC.

An IgG typically consists of two identical heavy chains (one variable domain and three constant domains) and two identical light chains (one variable domain and one constant domain)[130,131] (Figure 4-27). Fragment antigen-binding (Fab) consists of one constant domain and one variable domain of each of the heavy and the light chain from the N-terminal. Fragment

crystallisable region (Fc) consists of four constant domains of the heavy chains nearer to the C-terminal. The size of IgG is about 150 kDa, where both Fab and Fc are about 50 kDa. To investigate whether bivalency or the Fc-domain is essential for A1 binding and cytotoxicity on hPSC, monovalent Fab_A1 was generated with papain and bivalent $F(ab)_2$_A1 was generated with IdeS Protease.

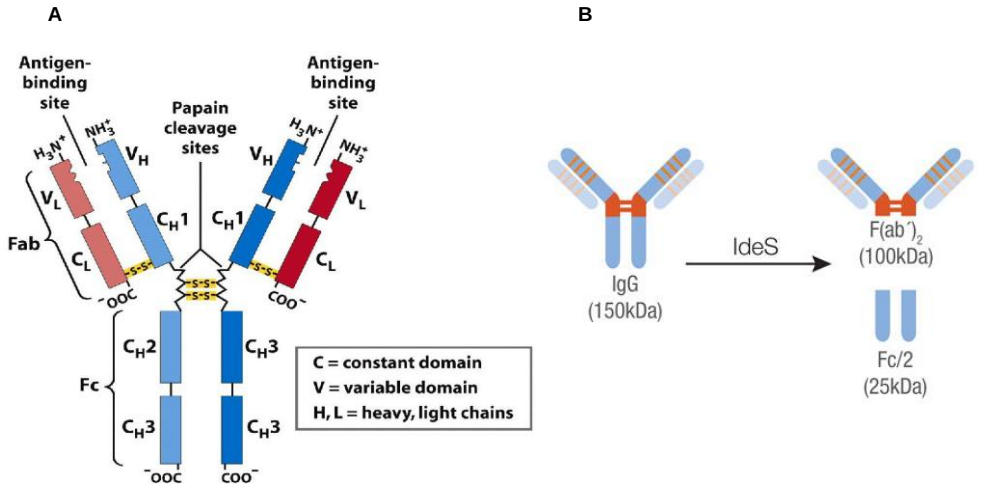

Figure 4-27: Sites of cleavage to generate Fab and $F(ab)_2$ by papain and IdeS respectively[130]
(A) Papain cleaves the peptide bonds linkage between the Fab fragments and Fc fragment[132]. (B) IdeS protease cleaves at a single site below the disulfide bond hinge region, yielding $F(ab)_2$ and Fc fragments[133].

After papain digestion, a mixture of monovalent Fab-A1, Fc-A1 and undesired by-products (smaller than 30 kDa) were obtained. The mixture was then dialyzed through a spin column (30 kDa pore size) to remove the by-products and papain (23 kDa). Subsequently, the protein mixture was resolved using Coomassie gel. Two distinct bands at 45 kDa and 51 kDa (Figure 4-28A) corresponding to the size of Fab and Fc fragments were observed. Even with dialysis, there are still some undesired by-products in the size between 19 kDa to 25 kDa. These small fragments are most likely from over-digestion of Fab or Fc. To determine the exact size of Fab-A1 and Fc-A1, resolved proteins

were transferred to PVDF membrane and immunoblotted with biotin-conjugated Fc-specific antibody. Fc-A1 band was then detected at 51 kDa with a streptavidin-FITC secondary antibody (Figure 4-28B). Therefore, the size of Fab-A1 is about 45 kDa. After IdeS protease digestion, IdeS with histidine tag was removed with affinity spin column. $F(ab)_2$_A1 was observed at 90 kDa, and Fc/2 was observed at 25 kDa (Figure 4-28).

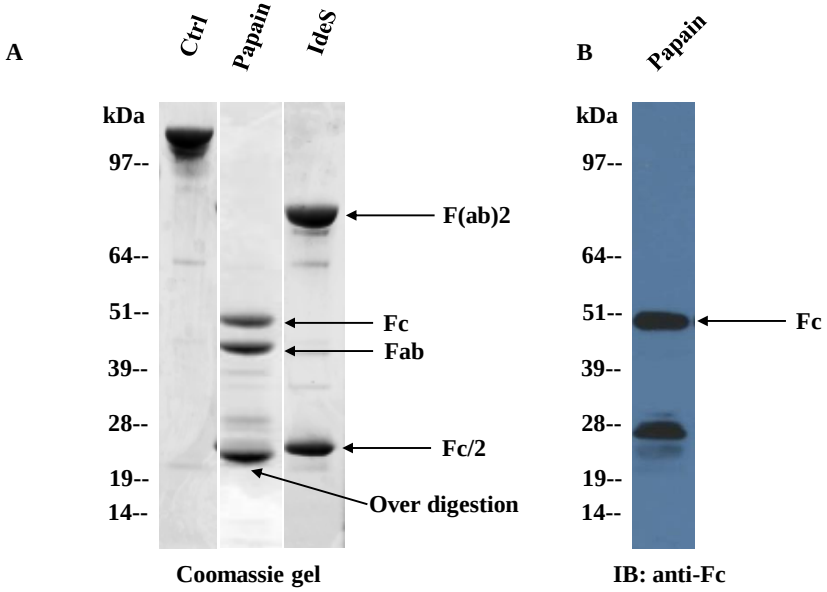

Figure 4-28: Size of digested antibody fragments.
(A) Antibody fragments were resolved in Coomassie gel. Upon papain digestion, two distinct protein bands at 45 kDa and 51 kDa are either Fab-A1 or Fab-Fc. Upon IdeS digestion, $F(ab)_2$_A1 was obtained at 90 kDa, Fc/2_A1 was obtained at 25 kDa; (B) Resolved proteins were transferred to PVDF membrane and Fc-A1 band was detected with an Fc-specific antibody. The size of Fc-A1 is about 51 kDa, therefore, the other protein band at 45 kDa in Coomassie gel would be Fab-A1.

In the subsequent experiments, Fc_A1 or Fc/2_A1 was not removed from the digestion mixture due to the low yield of affinity purification. It was demonstrated that Fc_A1 does not bind to hESC via flow cytometry analysis (Figure 4-29). Therefore, with the presence of Fc_A1 or Fc/2_A1 in the mixture, the binding and killing of Fab_A1 or $F(ab)_2$_A1 on hESC was not affected.

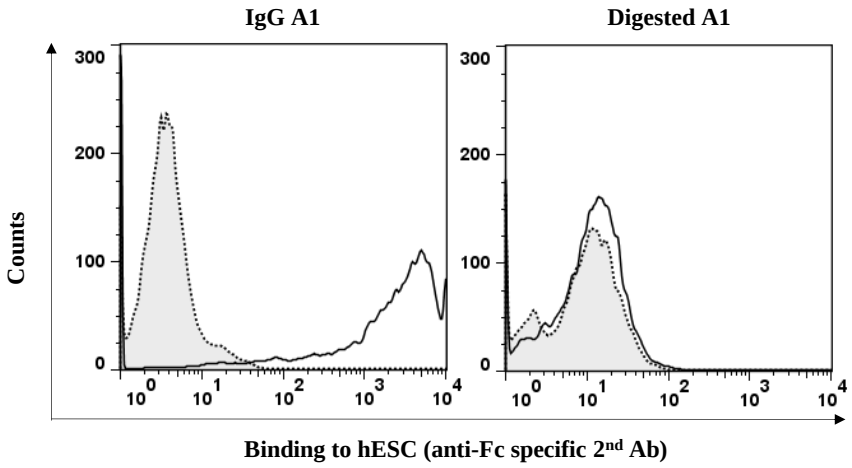

Figure 4-29: Fc_A1 in the digestion mixture does not bind to hESC
Human ESC were incubated with the digested A1 or undigested A1 for 45 minutes and followed by staining with biotin-conjugated Fc-specific primary antibody. Antibodies bound to cells were detected with a FITC-conjugated streptavidin. The shaded histogram represents staining with the negative control and open histograms represent staining with primary antibodies.

Next, the binding and killing of Fab_A1 and $F(ab)_2$_A1 on hESC was assessed via flow cytometry analysis. Cells were incubated with IgG_1_A1, $F(ab)_2$_A1, or Fab_A1 for 45 minutes. The binding of antibodies to hESC was detected by staining with FITC-conjugated anti-Kappa light chain specific antibody. Cell viability was estimated by PI uptake. Both Fab_A1 and $F(ab)_2$_A1 bound to hESC comparably as A1 (Figure 4-30A), suggesting neither bivalency nor Fc-domain is essential for A1 binding on hESC. However, $F(ab)_2$_A1 cytotoxicity on hESC was comparable to A1 whereas Fab_A1 did not elicit any cytotoxicity on hESC (Figure 4-30B). Hence, bivalency, but not the Fc-domain, is essential for A1 cytotoxicity on hESC.

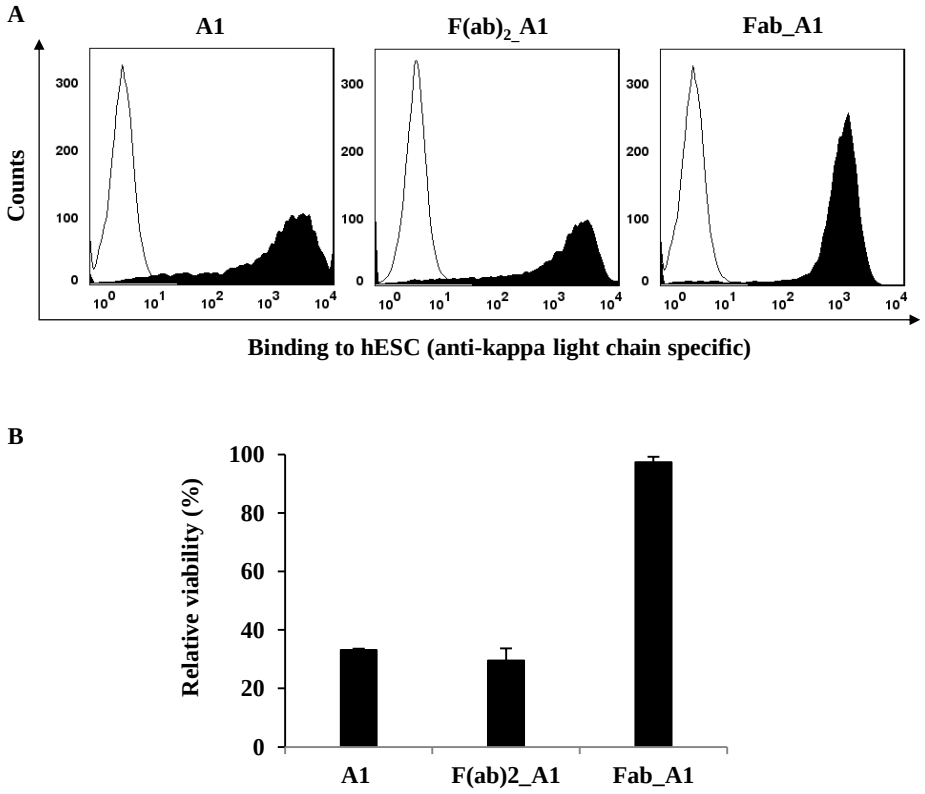

Figure 4-30: Bivalency of A1 is essential for its cytotoxicity on hESC, but not binding
Human ESC (2 x 10^5 in 100 µl) were treated with 5 µg of A1, $F(ab)_2$_A1 or Fab_A1 for 45 minutes at 4^oC. (A) Binding of $F(ab)_2$_A1 and Fab_A1 to hESC was comparable to A1. Antibody binding to hESC was detected with FITC-conjugated kappa light chain specific antibody. Representative histograms are shown. Open histogram represents non-treated cells and shaded histogram represents antibody-treated cells. (B) However, only bivalent $F(ab)_2$_A1 can recapitulate A1 cytotoxicity on hESC. Cell viability was assessed via PI uptake. Data are represented as mean ± SEM.

4.14 Summary

In this chapter, *in vitro* characterization of A1 was discussed in detail. A1, generated against undifferentiated hESC, showed strong binding and cytotoxicity on both hESC and hiPSC. By inducing hESC to undergo spontaneous differentiation via EB formation and FGF-2 starvation, A1 cytotoxicity was demonstrated to be highly specific to undifferentiated hESC, but not differentiating or differentiated cells. Unlike mAb84 that binds to glycosylated PODXL on hESC, A1 surprisingly recognizes an O-linked glycan epitope present on multiple antigens on hESC. The termini of this

glycan epitope were found to contain the sugar motif Fucα1-2Galβ1-3GlcNAcβ1-3Galβ1. Differences in the amino acid sequences of all three CDRs in the variable heavy and light chain were observed between A1 and mAb84, which further proved that they are different antibodies. Intriguingly, there are no competitive inhibition of binding between A1 and mAb84 suggesting that different epitopes are recognized by the mAbs. Being five times smaller than mAb84, A1 showed better penetration efficiency into EB. Cytotoxicity of A1 was dosage-dependent. A1 rapidly kills hESC within 5 minutes of incubation in a dosage-independent manner. A1 binding on hESC is a dynamic and reversible process. Killing is most likely achieved at saturated binding, when there are about 3 x 10^7 A1 molecules per hESC. A1 induced hESC plasma membrane damage with pore size larger than 20 nm. Last but not the least, A1 cytotoxicity on hESC requires minimally bivalency, and is independent of the Fc domain.

In conclusion, the cytotoxic antibody, A1, can be used as a cell surface marker for undifferentiated hESC and hiPSC. In hPSC-based therapy, A1 can be potentially used to eliminate residual undifferentiated hPSC from differentiated cell products especially in 3D aggregates to prevent teratoma formation. In the next chapter, *in vivo* characterization of A1 will be discussed.

5 CHAPTER 5 *IN VIVO* CHARATERIZATION OF A1

5.1 Introduction

The ability of A1 to kill undifferentiated hPSC *in vitro* is characterized in chapter 4. As the ultimate application of cytotoxic A1 is to eliminate residual undifferentiated hPSC from differentiated cells and therefore prevent teratoma formation, in this chapter, we determined the ability of A1 to prevent teratoma formation *in vivo*. Previously, Tan et al. showed that injection of hESC pre-treated with mAb84 for 45 minutes *in vitro* successfully prevented teratoma formation in SCID mouse models for up to 6 months post-injection[34]. Leveraging on the success of mAb84, the study was extended in this thesis to evaluate the potential of teratoma formation if undifferentiated hESC was mixed with A1 just prior to injection into SCID mouse models, without further *in vitro* incubation. Additionally, we also evaluated the efficiency of *in vivo* A1 treatment to prevent teratoma formation in SCID mouse models.

5.2 Teratoma grading system

Teratoma formation in SCID mice was monitored visually and measured by caliper using a previously established grading system for the study of mAb84[34]: grade 0 = no visible teratoma (6.32 mm average maximal hind leg diameter), grade 1 = teratoma just detectable (10.55 mm average), grade 2 = teratoma obvious (13.2 mm average), and grade 3 = teratoma impedes locomotion (14.52 mm average).

5.3 SCID mouse model: instantaneous *in vitro* A1 treatment

Based on *in vitro* characterization, A1 showed rapid killing on undifferentiated hPSC within 5 minutes of incubation. Hence, we aimed to investigate whether

this rapid killing is efficient to prevent teratoma formation *in vivo*. Single-cell suspension of hESC (5 x 10^6 cells/per mouse in 30 µl fresh KO media and 30 µl matrigel) were mixed with 30 µl of IgG_1 A1, or $F(ab)_2$_A1, or IgG_1 A19, or HEPES buffer under identical conditions, and instantaneously (without further incubation) injected into SCID mouse via intramuscular (IM) route. IgG_1 A19 was incorporated as an isotype control since it binds to hESC without exerting cytotoxicity. Treatment with $F(ab)_2$_A1 was used to preclude the possibility of ADCC.

In the first trial, teratoma formation under each condition was monitored 5 weeks after injection (Figure 5-1A). All 3 mice in the buffer control group developed grade 3 teratomas by week 6 post-injection. Cells treated with the isotype control, IgG_1 A19, also formed teratomas as early as non-treated cells and all reached grade 3 by week 7, indicating that antibody binding to hESC alone has no effect on preventing teratoma formation. In contrast, cells treated with IgG_1 A1 did not form teratomas in 2 SCID mice after 10 weeks post-injection. In the remaining SCID mouse injected with IgG_1 A1 treated hESC, the onset of teratoma formation was delayed until week 8. The ability to still form teratomas after A1 treatment was most likely due to non-homogenous mixing without incubation between antibodies and undifferentiated hESC. Moreover, cells treated with $F(ab)_2$_A1 also did not form teratomas in all 3 SCID mice after 10 weeks post-injection, indicating that the prevention of teratoma formation *in vivo* is caused by the mAb directly and independent of ADCC. Successful prevention of teratoma formation in five out of six SCID mice suggested that *in vitro* treatment with either IgG_1 A1 or $F(ab)_2$_A1 just prior to injection could be effective.

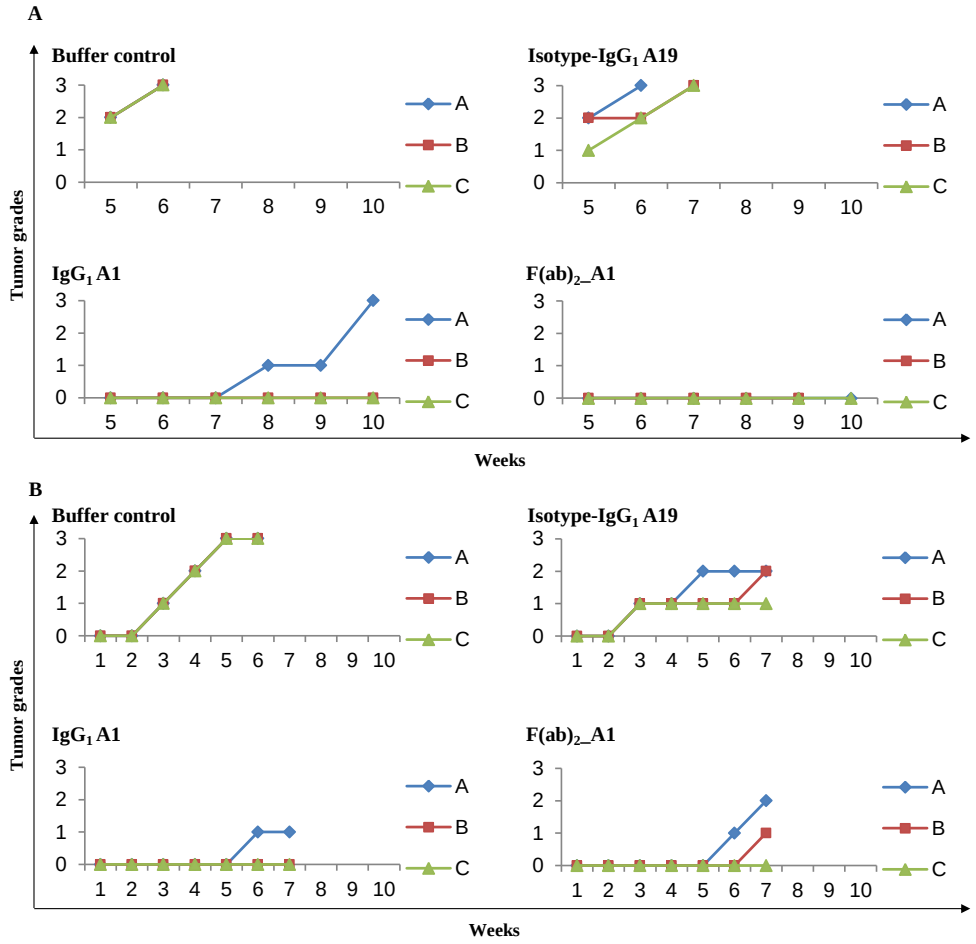

Figure 5-1: Prevented or delayed teratoma formation with *in vitro* A1 treatment.
Undifferentiated hESC was mixed with antibodies or buffer control *in vitro* instantaneously prior to injection into SCID mouse models. Each condition has 3 SCID mice. (A) First trial: teratoma formation was monitored from week 5 post-injection. (B) Second trial: teratoma formation was monitored from week 2 post-injection.

A second trial was performed to further confirm this result and to begin monitoring the teratoma formation in SCID mouse models from grade 1 onwards. Consistent with the first study, cells in buffer control or treated with the isotype control developed grade 3 teratomas by week 6 post injection where palpable grade 1 tumours were observed as early as week 2 post-injection (Figure 5-1B). For cells treated with IgG_1 A1, 2 SCID mice did not form teratomas after 7 weeks whilst 1 SCID mouse showed delayed teratoma formation with grade 1 teratoma observed only after week 7 post-injection. Two SCID mice with $F(ab)_2$_A1 also showed delayed teratoma formation with

the onset only occurring at either week 6 or week 7 post-injection. These results confirmed that instantaneous *in vitro* A1 treatment can prevent or delay teratoma formation. However, delayed onset of teratoma formation in several SCID mice renders further optimization to improve the efficiency of instantaneous *in vitro* A1 treatment. This could include a longer incubation *in vitro* before injection.

5.4 SCID mouse model: *In vivo* A1 treatment

A1 has been demonstrated to have better penetration efficiency over mAb84 into EB clusters. Here, we evaluated its efficiency in preventing teratoma formation via *in vivo* treatment. Single-cell suspension of hESC were firstly injected into SCID mouse, and followed by the injection of IgG_1 A1 or $F(ab)_2$_A1 at approximately the same site under identical conditions. The same buffer control group from the second trial of *in vitro* treatment was used here since both experiments were performed at the same time with the same source of undifferentiated hESC and A1.

Teratoma formation was monitored from week 2 post-injection. Comparing to non-treated mice developing teratomas at week 2, all 3 SCID mice injected with IgG_1 A1 did not form teratomas after week 7 post-injection (Figure 5-2), indicating IgG_1 A1 can potentially be administered directly *in vivo* to kill undifferentiated hESC and prevent teratoma formation. However, SCID mice injected with $F(ab)_2$_A1 only showed a delayed onset of teratoma formation at week 5 or week 6.

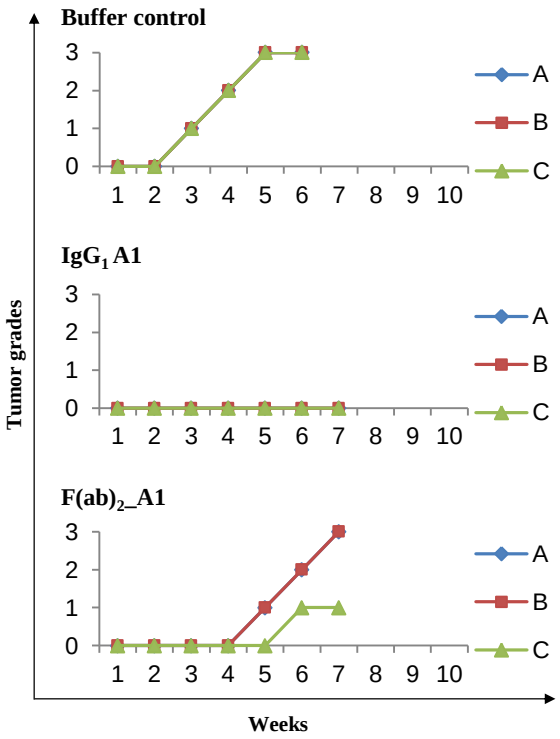

Figure 5-2: Prevented or delayed teratoma formation with *in vivo* A1 treatment.
Undifferentiated hESC was injected into SCID mouse models first followed by injection of antibodies at approximately the same site. Each condition has 3 SCID mice.

For *in vivo* A1 treatment, since A1 was administered in close proximity to undifferentiated hESC, the more likely route for the mAbs to locate the hESC *in vivo* would be via localised diffusion rather than systemic circulation. As for the difference between A1 and $F(ab)_2$_A1, we postulate that $F(ab)_2$_A1 may be drained from the tissue into systemic circulation more quickly and therefore lowering the localised concentration of $F(ab)_2$_A1 for interaction with hESC-containing tissue. This is because antibody fragments without the Fc portion have been reported to cross the blood-tissue barrier more easily and are less hindered by the binding-site barrier[134]. Furthermore, $F(ab)_2$_A1 will also be cleared more easily from the systemic circulation and out of the body without the protection by neonatal Fc receptor (FcRn) compared to IgG_1 A1[135].

5.5 Summary

To facilitate the use of cytotoxic A1 in hPSC-based therapy, we demonstrated that both *in vitro* and *in vivo* A1 treatment can prevent or delay teratoma formation by undifferentiated hESC in SCID mouse models. Treatment with isotype control did not delay or prevent teratoma formation compared to the buffer control group, indicating non-cytotoxic antibody binding to hESC does not affect teratoma formation, for example, by ADCC. Moreover, *in vitro* treatment with $F(ab)_2$_A1 also prevented or delayed teratoma formation, comparable to IgG_1 A1. We therefore conclude that the killing of hESC with A1 and prevention of teratoma formation is a direct effect of the mAb and independent of ADCC. These data provide a proof of concept that A1 can be administered both *in vitro* and *in vivo* to kill undifferentiated hESC and prevent *in vivo* teratoma formation in hPSC-based therapy.

6 CHAPTER 6 ELUCIDATION OF A1-INDUCED HESC DEATH MECHANISM

6.1 A1 induces hESC death via oncosis

6.1.1 Introduction

As discussed previously, there are two major modes of cell death in the pre-mortal phase: apoptosis and oncosis. Apoptosis and oncosis can be distinguished by their respective hallmarks (Table 6-1). Based on *in vitro* characterization, A1 kills hPSC within 5 minutes of incubation and resulting in the formation of pores larger than 20 nm in the plasma membrane. These two features match well with the hallmarks of oncosis. Therefore, it was hypothesized that A1 kills hPSC via oncosis, not apoptosis. In this section, hallmarks of apoptosis and oncosis were examined in A1-induced hESC death to confirm the hypothesis.

Table 6-1: Different hallmarks of apoptosis and oncosis.

	Apoptosis	**Oncosis**
Cell death time	Slow (12-24hrs)	Fast (seconds to minutes)
DNA fragmentation	Increased	No change
Caspases activity	Increased	No change
Volume changes	Shrinking of cytoplasm and condensation of nucleus	Swelling of cytoplasm and mitochondria
Membrane pore formation	No	Yes
Cytoplasm	Retained in apoptotic bodies	Released

6.1.2 A1-treated hESC does not undergo apoptosis

First, this hypothesis was reiterated by two complimentary biochemical assays for apoptosis: TUNEL assay and caspase assay.

6.1.2.1 TUNEL assay

TUNEL assay was used to measure the extent of DNA fragmentation upon cell death[107]. In TUNEL assay, 3' end of DNA fragments are labelled with fluorescent-tagged dUTP catalysed by TdT enzyme. The intensity of dUTP and DNA size were read by flow cytometry. Increased dUTP intensity is correlated to DNA fragmentation and plotted in Figure 6-1. As positive control, confluent hESC cultures were exposed to 200 mJ of UV to induce apoptosis. After UV exposure, the cells were maintained at 37^{o}C, 5% CO_2 for 20 hours before harvest for apoptotic assays. A1-treated hESC did not exhibit significant elevation in the level of DNA fragmentation compared to the negative control, non-treated hESC. On the contrary, the positive control, UV-treated hESC exhibited a significant elevation in the level of DNA fragmentation.

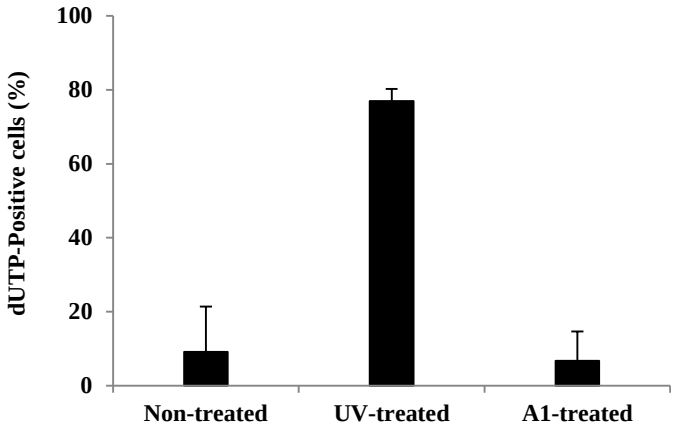

Figure 6-1: Degree of DNA fragmentation measured in TUNEL assay by flow cytometry. Increase in dUTP fluorescence intensity was correlated to increased DNA fragmentation. UV-treated hESC was positive control. Data are represented as mean ± SEM.

6.1.2.2 Caspase assay

Next, we compared the activity of several caspases (caspases 3, 7 and 9) between A1-treated hESC, UV-treated hESC and non-treated hESC. In this

assay, fluorescence-labelled inhibitor of caspase reagents were used to specifically detected activated caspase. To correlate cell death with caspase activity, cells were co-stained with a cell impermeable dye, 7-AAD, to identify dead cells. Fluorescence intensity of caspase reagents and 7-AAD were displayed on a scatter plot by flow cytometry (Figure 6-2A) and gated into four different quadrants. The population in each quadrant was plotted in Figure 6-2B. Results showed that the activity of caspases measured for both A1-treated and non-treated hESC were comparable and at minimal basal levels. In contrast, UV-treated hESC exhibited significantly higher caspases activities. Hence, results from both apoptotic assays suggested that the A1 killing of hPSC was unlikely induced by apoptosis.

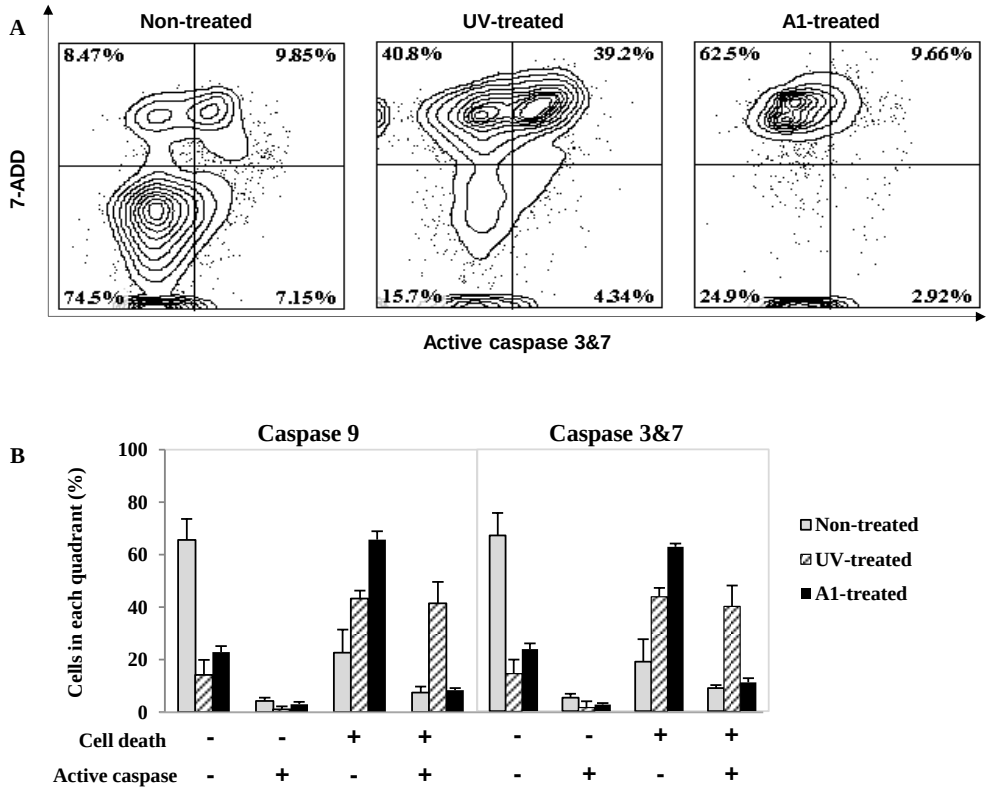

Figure 6-2: Measured caspases activity and cell death by flow cytometry.
(A) A representative scatter plot of detecting active caspase 3&7 and cell death. Fluorescence-labelled inhibitor of caspase reagents were used to specifically identify active caspases. Cell death was determined with 7-AAD dye by measuring cell membrane integrity. UV-treated hESC was positive control. Bottom left quadrant represents viable cells without active caspase; top left quadrant represents dead cells without active caspase (oncosis); top right quadrant represents dead cells with active caspase (apoptosis). Population in each quadrant was plotted in (B). Data are represented as mean ± SEM.

6.1.3 Morphological and structural changes of A1-treated hESC

Morphological changes, such as cell volume change, plasma membrane damage, and apoptotic bodies, are hallmarks to distinguish apoptosis and oncosis. Therefore, to further elucidate the mode of A1-induced hESC death and investigate the lethal effect of A1 on hESC, we examined the morphological and structural changes under confocal microscopy for time-lapsed dynamics, scanning electron microscopy for surface morphological and cell structural changes, as well as transmission electron microscopy for intracellular morphological changes on hESC before and after A1 treatment.

6.1.3.1 Time-lapsed dynamics of A1-treated hESC under confocal microscope

Knowing that A1 is able to induce hESC death within several minutes of incubation, we went on to examine the dynamic morphological changes of hESC in culture under time-lapsed Spinning Disk Confocal Microscope. Immediately after the *in-situ* treatment with A1, hESC started to retract from each other and round up on the culture plate (Figure 6-3). Cell morphology changed drastically over the first 10 minutes. After imaging, the mAb-containing buffer was aspirated. Cells were washed with PBS-, topped up with condition media, and incubated in 37^{o}C, 5% CO_2 for an additional 24 hours to test the survival rate after A1 treatment. Almost all A1-treated hESC detached from the culture plate and were assessed to be dead by PI uptake assay. This is indicative that A1 is capable of killing hESC in culture. However, hESC confluency seemed to be an important factor for A1-induced morphological changes. No obvious morphological changes were observed if hESC confluency was > 80%. This could be possibly explained by the strong stress

fibre formed in focal adhesions as well as formation of stress fibre connection through cell-cell junction when cells reach confluency in culture[137,138].

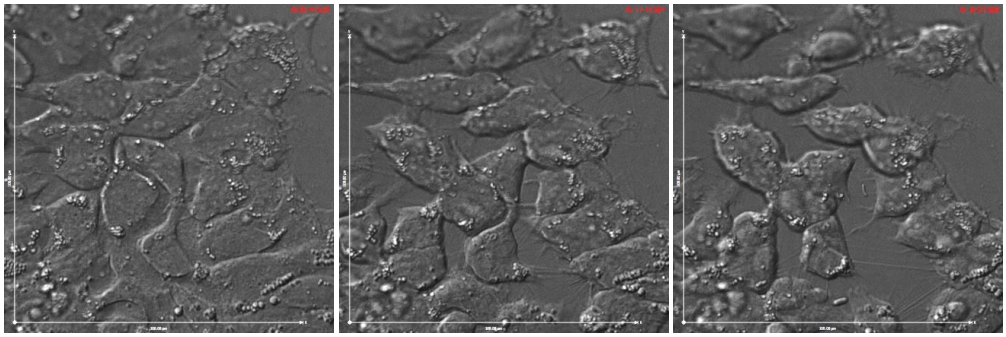

0 minutes **5 minutes** **10 minutes**

Figure 6-3: Dynamics of A1-treated hESC in culture under Confocal Microscopy.
Human ESC were cultured for 4 days prior to A1 treatment. Cell confluency was about 40%. A1 was added into cell culture right after the recording was started. Scale bar: 100 μm.

6.1.3.2 Visualization of hESC under Transmission Electron Microscope (TEM)

Previous studies on antibody-induced cell death have used TEM to investigate the cell death mechanism. According to Matsuoka[71], mAb RE2 was reported to induce lymphocyte death. Under TEM, they observed the plasma membrane damage, dilation of ER and mitochondria. With these observations, they concluded that this antibody induces lymphocyte death via oncosis. Separately, a study on GA101-induced oncosis also revealed early stage intercellular adhesion and involvement of microvilli in intercellular adhesion under TEM[74]. We therefore used TEM to study the intracellular and intercellular morphological changes of A1-treated hESC. Cells in single cell suspension were treated with A1 (5 μg per 2 x 10^5 hESC in 100 μl) or PBS control for 45 minutes, followed by immediate fixation. Upon fixation, cells were processed as described previously for TEM imaging. Non-treated cells were uniformly distributed with an average size of approximately 10 μm in diameter, uniform staining intensity, and intact plasma membrane (Figure 6-4).

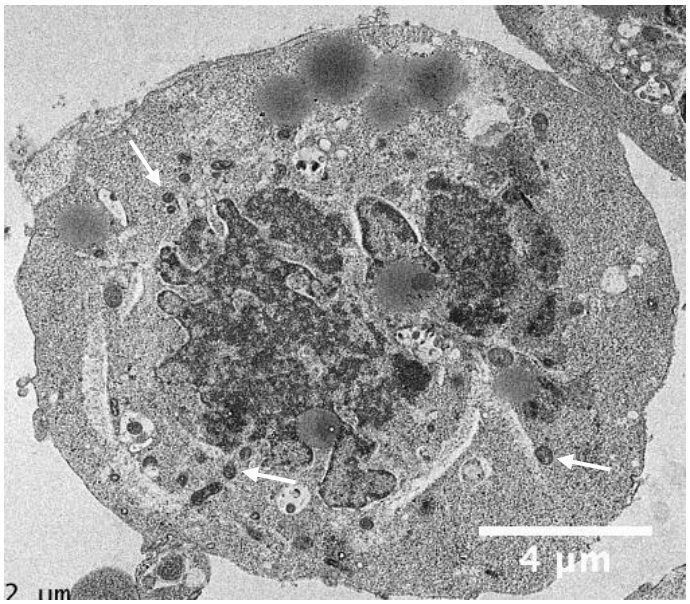

Figure 6-4: Morphology of a non-treated hESC under TEM.
Human ESC were fixed with paraformaldehyde and glutaraldehyde, embedded in resin, sectioned into ultra-thin sections, stained with uranyl acetate and lead citrate to be viewed under TEM. Non-treated hESC had uniform cell shape and intact membrane. Mitochondria were marked with white arrows.

Upon A1 treatment, distinct morphological alterations were observed. In general, there was no formation of apoptotic bodies in A1-treated hESC. Instead, significant enrichment of mitochondria was observed (Figure 6-5A). These mitochondria had well-developed cristae suggesting that they were in an energy-producing phase. This feature has not been reported in other similar modes of cell death. Figure 6-5B showed an example of intercellular adhesion formed by four A1-treated hESC. Different staining intensities were observed among these cells. One possible reason could be that they were at different stages of cell death and thus the amount of proteins being stained was different. The cell at the bottom right was least stained and it had lost its membrane integrity and cell morphology, suggesting this cell was undergoing post-mortal oncotic necrosis. The cell in the middle had lower staining intensity than the two cells at the top. However, this cell has the most apparent cell swelling and

mitochondria swelling, which suggest that swelling occurred at later stage than protein degradation in A1-induced hESC death. Moreover, peripheral re-localisation of mitochondria in this cell towards cell-cell adhesion sites was also observed (Figure 6-5B). These observations further proved our hypothesis that A1 kills hESC via oncosis, and it may also imply that A1-induced cell death may be associated with mitochondria, ATP and adhesion proteins.

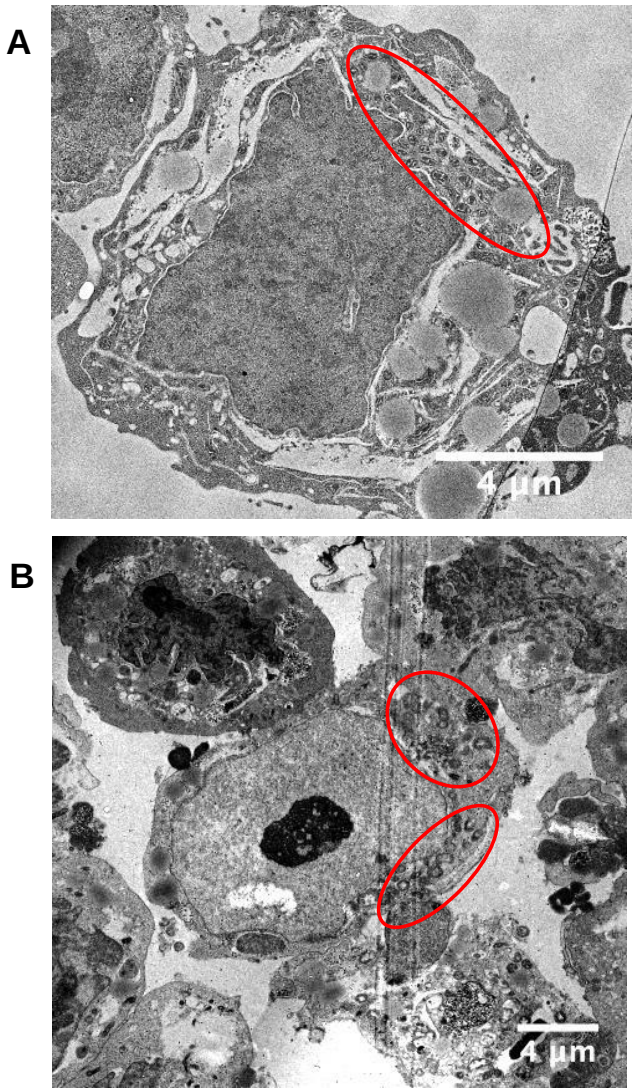

Figure 6-5: Morphological changes of A1-treated hESC under TEM.
Human ESC were treated with A1, fixed with paraformaldehyde and glutaraldehyde, embedded in resin, sectioned into ultra-thin sections, stained with uranyl acetate and lead citrate to be viewed under TEM. (A) Significantly enriched mitochondria (highlighted with red circle) were observed in A1-treated hESC. These mitochondria had well-develop cristae, suggesting the cell was at energy producing stage. (C) An example of intercellular adhesions formed by 4 cells. Cells were not uniformly stained and lost different degrees of membrane and cell integrity. Peripheral re-localisation of mitochondria towards cell-cell adhesion sites was highlighted in red circle.

6.1.3.3 Visualization of hESC under Scanning Electron Microscope (SEM)

Next, we examined hESC for cell surface morphological changes and cell structural changes under scanning electron microscopy (SEM). Cells in single cell suspension were treated with A1 (5 μg per 2 x 10^5 hESC in 100 μl) or PBS control for 45 minutes, followed by immediate fixation. Upon fixation, cells were processed as described previously for SEM imaging. In general, non-treated hESC had uniform shape, rich microvilli and intact plasma membrane (Figure 6-6).

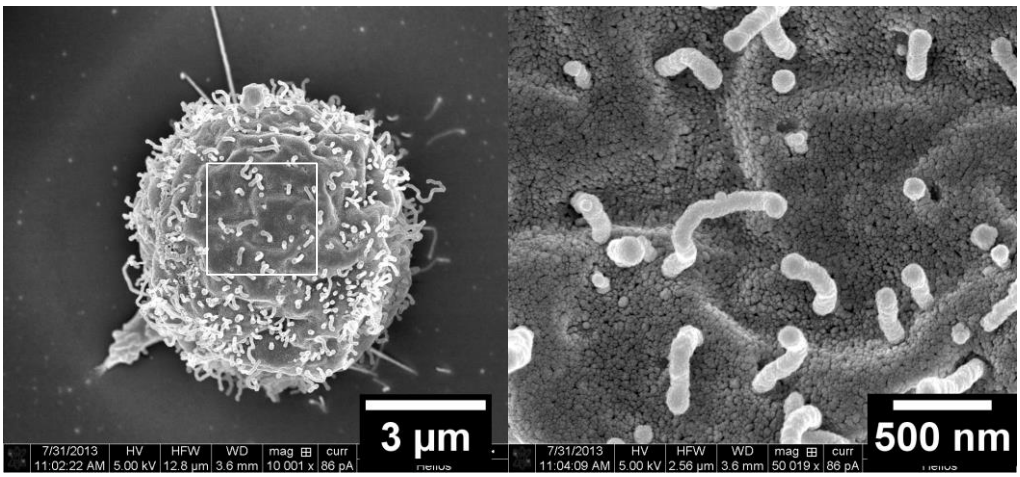

Figure 6-6: Morphology of non-treated hESC under SEM.
Left: overview of a single hESC; right: highlighted area in higher magnification. Arrows indicates microvilli.

Upon A1 treatment, there was a loss of cell surface microvilli and membrane integrity. Pores were formed on the plasma membrane with convoluted surface, which were usually covered by debris networks of fused microvilli or damaged plasma membrane. A 5-staged pattern of hESC morphological changes triggered by A1 treatment was summarized. At stage 1, A1-treated hESC typically displayed partially degraded or shortened microvilli and enlarged cell volume, whereas the membrane integrity was still relatively

intact (Figure 6-7). Some fused microvilli at certain membrane area should be the transition from stage 1 to stage 2.

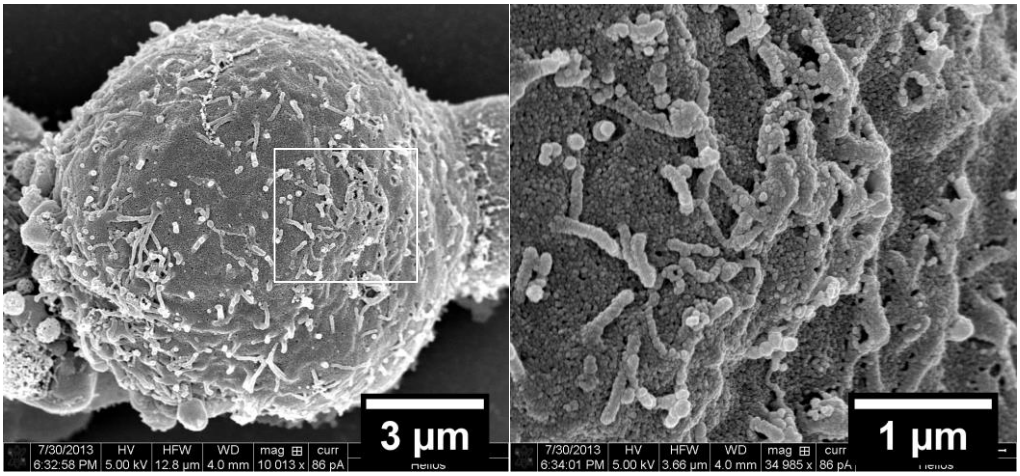

Figure 6-7: Morphological changes of A1-treated hESC at stage 1 under SEM.
Left: overview of a single hESC; right: highlighted area in higher magnification. A1-treated hESC at stage 1: relatively intact membrane, but degraded/shortened microvilli and cell swelling. Fused microvilli are likely to be the transition from stage 1 to stage 2.

At stage 2, numerous membrane pores in varied sizes were formed (Figure 6-8). Another feature at stage 2 was the appearance of one or more circular shaped areas of ~2 µm that were always surrounded by fused microvilli. Within this area, microvilli were absent but there was the presence of cytoskeleton-like structures.

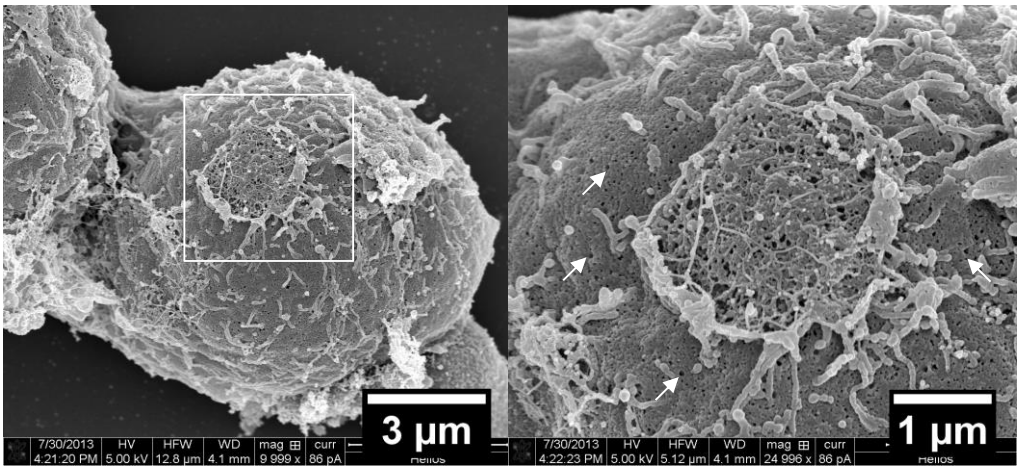

Figure 6-8: Morphological changes of A1-treated hESC at stage 2 under SEM.
Left: overview of a single hESC; right: highlighted area in higher magnification. A1-treated hESC at stage 2: formation of membrane pore in varied sizes (indicated by arrows) and appearance of partially damaged membrane area in circular shape.

At stage 3, microvilli further shortened or even completely disappeared (Figure 6-9). Different from stage 2, in the circular area, both the surrounding fused microvilli and the centred cytoskeleton-like structures disappeared. Moreover, larger membrane pores were formed.

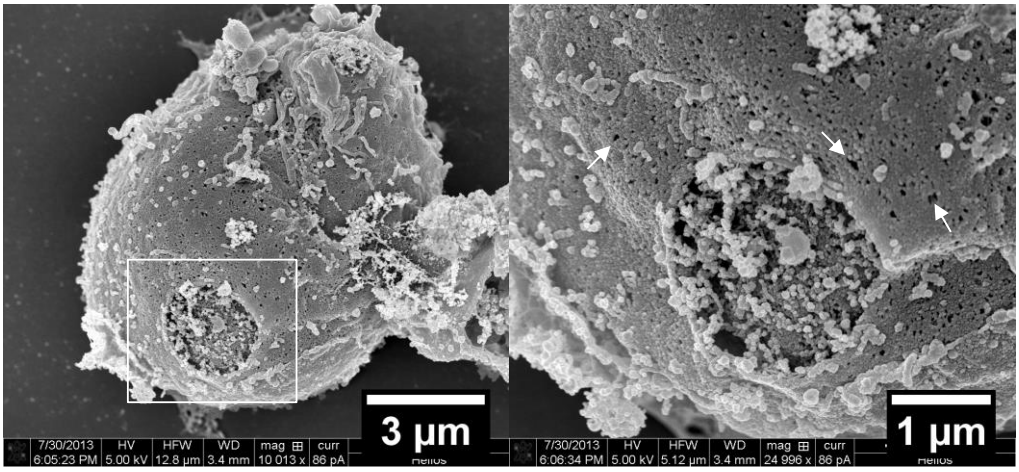

Figure 6-9: Morphological changes of A1-treated hESC at stage 3 under SEM.
Left: overview of a single hESC; right: highlighted area in higher magnification. A1-treated hESC at stage 3: Microvilli further shortened or even completely disappeared. Larger membrane pores formed as indicated by arrows. In highlighted area, fused microvilli around the circular area as well as the cytoskeleton-like structures in the centre disappeared.

At stage 4, membrane damage was more pronounced and likely from the damaged circular area of stage 3 revealing the cytoskeleton structure and nucleus (Figure 6-10A). Lastly, at stage 5, severely damaged membrane peeled off from the nucleus leaving the nucleus uncovered (Figure 6-10B). Among these observed morphological changes, cell swelling, plasma membrane pore formation and subsequent severe plasma membrane damage are all previously reported hallmarks of oncosis. The progress of morphological changes also suggested that A1-induced hESC death is likely associated with altered stability of microvilli and actin cytoskeleton structures.

A

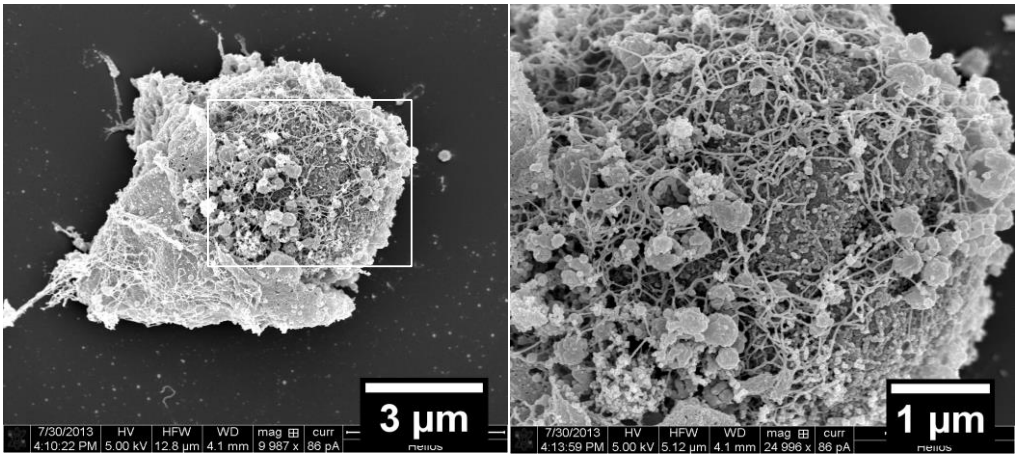

B

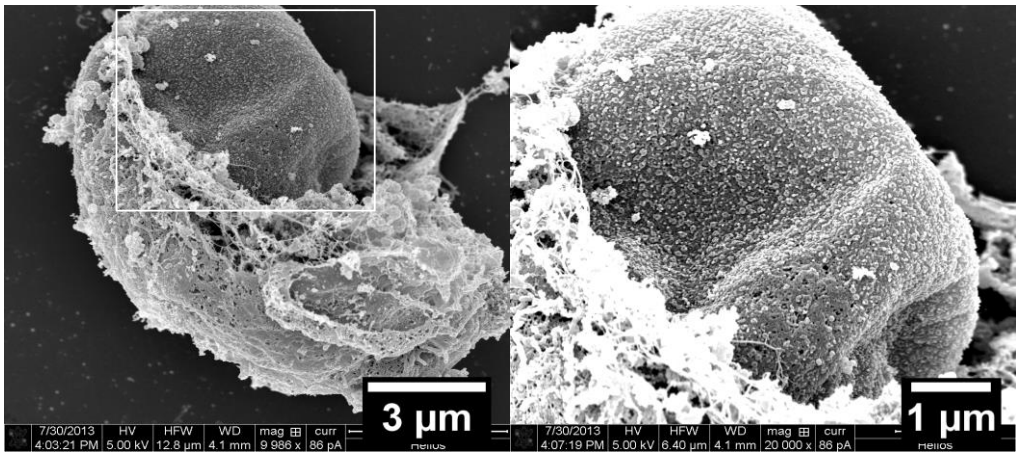

Figure 6-10: Morphological changes of A1-treated hESC at stage 2 under SEM.
Left: overview of a single hESC; right: highlighted area in higher magnification. (A) A1-treated hESC at stage 4: massive membrane damage; Membrane damage was worsen from the damaged circular area of stage 3 and visible nucleus covered by massive cytoskeleton structures; (B) A1-treated hESC at stage 5: damaged membrane peeling off from the nucleus.

6.1.4 Summary

In this section, effort was made to determine the mode of A1-induced hESC death. In two apoptosis assays, it was proved that A1-treated hESC did not have significant increase in the level of DNA fragmentation as well as caspases activity. Therefore, A1 was unlikely killing hESC via apoptosis. Furthermore, under confocal microscope, TEM and SEM, features that are consistent with the hallmarks of oncosis were observed, including absence of

apoptotic bodies, cell swelling, plasma membrane pore formation, and severe plasma membrane damage. Taking together all the features, we concluded that A1 kills hESC via oncosis. Intriguingly, we also observed mitochondria enrichment and peripheral re-localisation, microvilli shortening or degradation, as well as massive destruction of actin cytoskeleton structures. These events were hypothesized to be associated with the mechanism of A1-induced hESC death, which will be discussed in detail later in this thesis.

6.2 A1 binds uniformly on hESC surface

Next, to better understand how A1 binding to hESC leads to cell death, we examined the distribution pattern of A1 on hESC surface under scanning electron microscope aided with gold-conjugated secondary antibodies to reveal the distribution. Briefly, hESC were treated with A1 or PBS- control, fixed with glutaraldehyde and paraformaldehyde, incubated with gold-conjugated secondary antibodies, dehydrated, critical point dried and viewed under SEM.

Samples were viewed under three different modes: cell morphology was detected under secondary electron mode while gold particle-labelled A1 were detected under backscattering mode. Overlay between cell morphology and A1 binding was viewed under combined mode. No non-specific binding of secondary antibodies was observed in non-treated control (Figure 6-11). Consistent with previous observation under normal SEM, the cell membrane non-treated cell was intact and covered with rich microvilli.

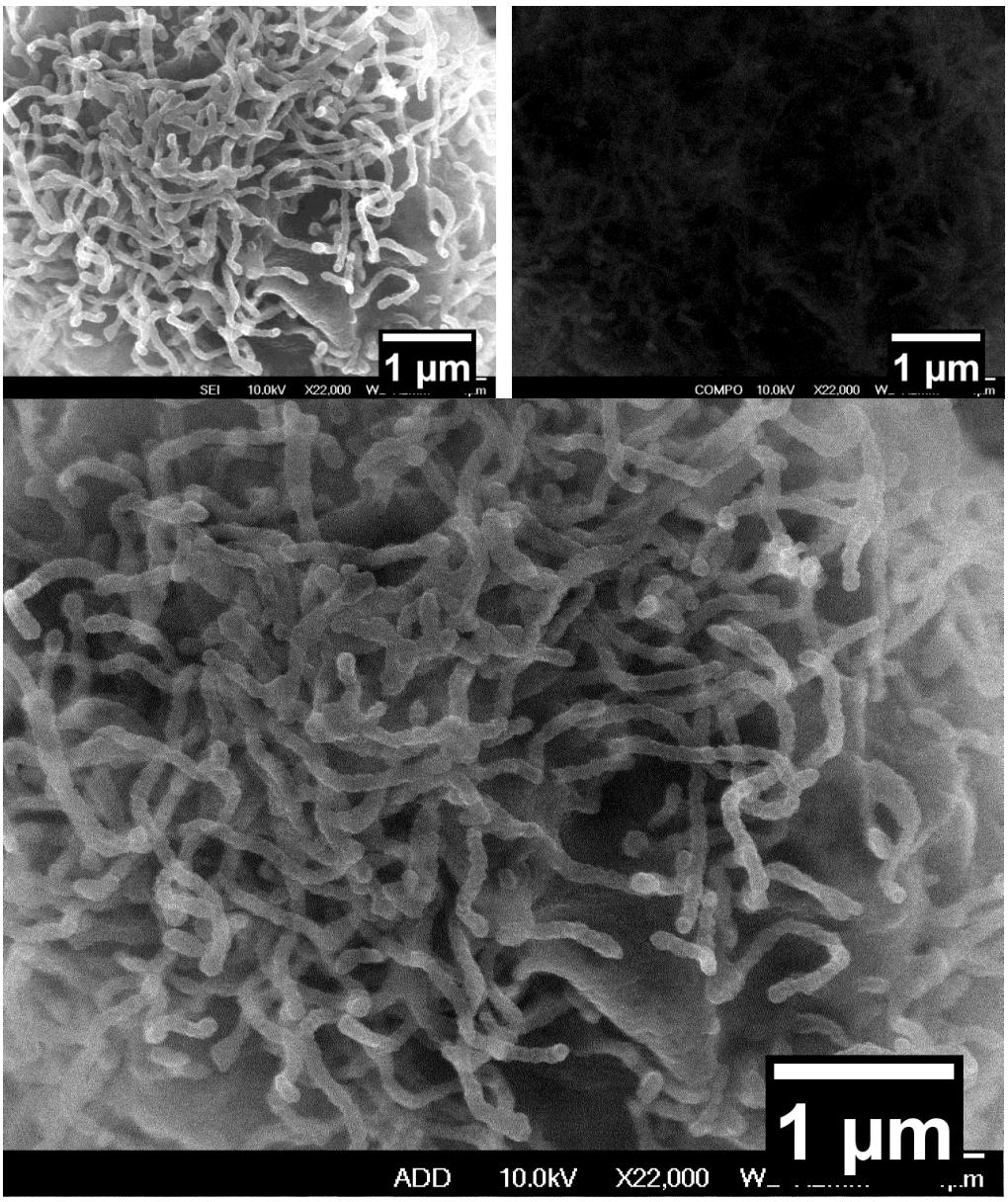

Figure 6-11: Non-treated hESC under immuno-SEM.
Cell morphology was detected under secondary electron mode (upper left) while gold particle-labelled A1 were detected under backscattering mode (upper right). Overlay between cell morphology and A1 binding was viewed under combined mode (bottom). Representative images are shown. No non-specific binding of secondary antibodies on hESC under immuno-SEM.

In A1-treated hESC, A1 particles were uniformly distributed across the cell surface (Figure 6-12). Previously, in mAb84-induced hESC death, gold-labelled antibody clusters were observed under backscattering mode[34]. Without the combined mode, this clustering effect was interpreted as antibody clustering antigens to form pores throughout the plasma membrane. However,

in our study, under combined mode, it was clear that there was no correlation between A1 binding pattern and plasma membrane damage.

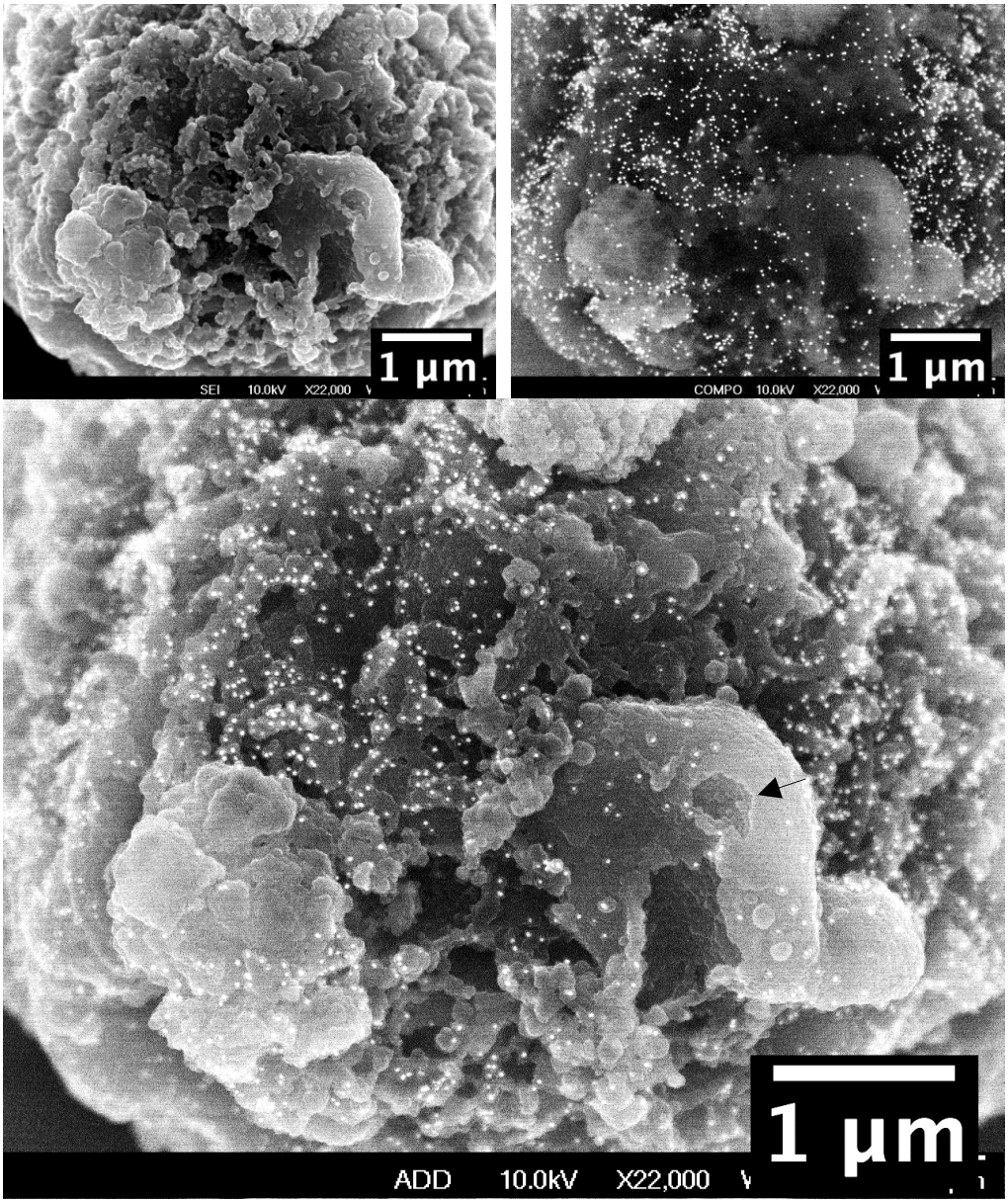

Figure 6-12: A1 binding pattern was not correlated with plasma membrane damage.
Cell morphology was detected under secondary electron mode (upper left) while gold particle-labelled A1 were detected under backscattering mode (upper right). Overlay between cell morphology and A1 binding was viewed under combined mode (bottom). Representative images are shown. A1 binding on hESC is uniform. Arrow indicates an example of plasma membrane damage that was not correlated with A1 binding pattern.

On the contrary, observed clusters of gold particle were more likely resulting from fusion of microvilli and damaged plasma membrane (Figure 6-13). These observations suggest that the formation of membrane pores was not the result

of external mechanical force from A1 binding, but more likely through A1 binding initiated signalling cascade.

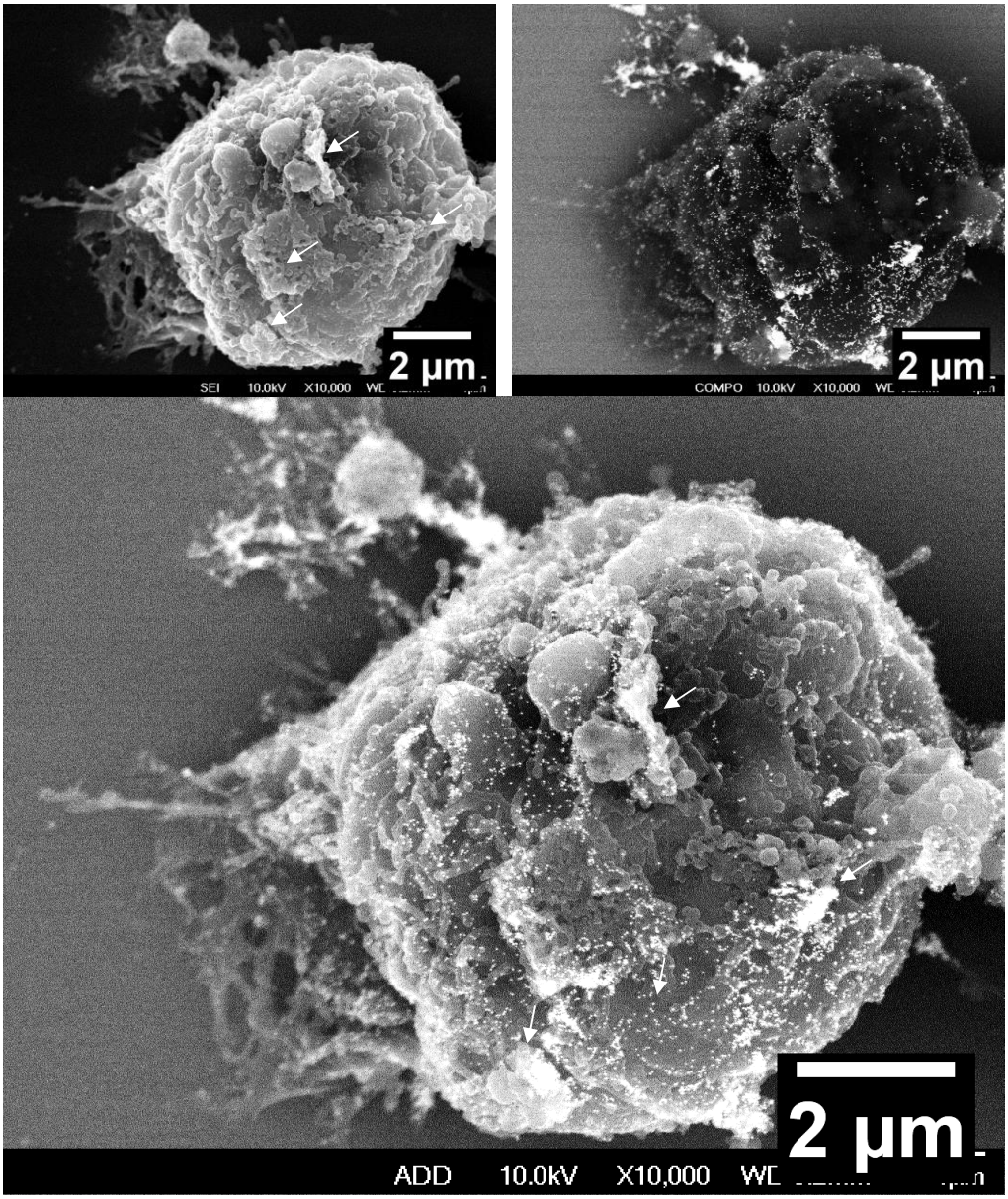

Figure 6-13: Correlation between A1 aggregates and membrane debris.
Arrows indicates the correlation between A1 (gold particles) aggregates and debris of fused microvilli or damaged plasma membrane.

Surprisingly, we also observed that the majority of A1 binding was on surface microvilli, both elongated and shortened (Figure 6-14), suggesting that A1-induced death signalling might be initiated through receptors on surface microvilli.

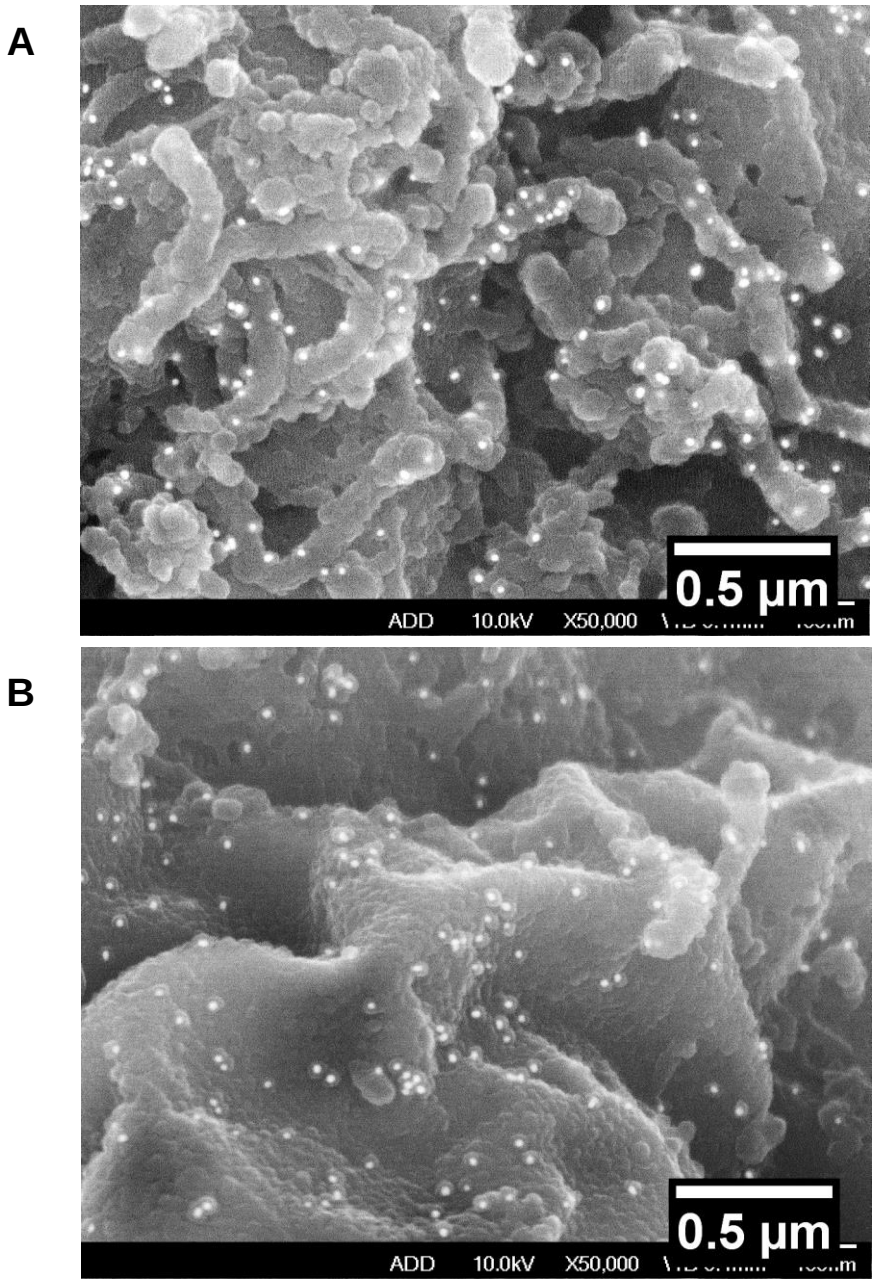

Figure 6-14: A1 bound to surface microvilli of hESC.
Representative images are shown in combined mode. (A) A1 bound to elongated hESC microvilli. (B) A1 bound to shortened hESC microvilli.

6.3 Bivalent A1 binding elicits hESC homotypic adhesion

Upon A1 binding, we also observed formation of hESC aggregates (Figure 6-15). Formation of cell aggregate or homotypic adhesion has been reported in many antibody-induced cell death via either apoptosis[139,140] or oncosis[72,74,79]. To investigate the cause of homotypic adhesion, we first used an in-house antibody control, mAb8 (IgG) which binds to EpCAM on hESC without

conferring cytotoxicity[141]. Binding of bivalent antibodies alone to hESC was previously shown not to sufficient to elicit homotypic adhesion (data not shown). Moreover, the difference in the ability of $F(ab)_2$_A1 and Fab_A1 to induce homotypic adhesion was observed (Figure 6-15). Intriguingly, this difference coincided with the difference in their cytotoxicity on hESC, indicating homotypic adhesion and cell death is functionally related.

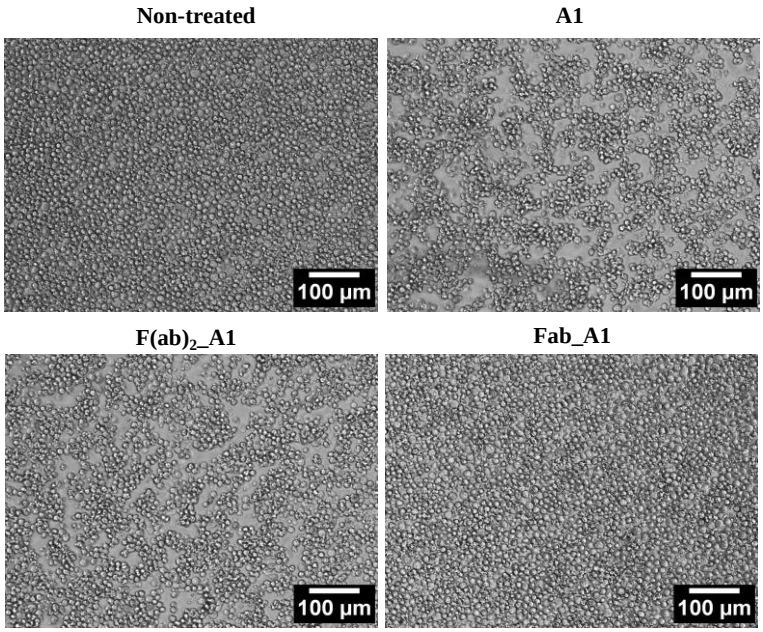

Figure 6-15: Bivalent A1 and $F(ab)_2$_A1 can induce hESC homotypic adhesion.
Human ESC (2 x 10^5 in 100 µl) were treated with 5 µg of A1, $F(ab)_2$_A1, or Fab_A1 for 45 minutes at 4°C in 96-well plates. After incubation, cells were viewed under bright field light microscopy. Homotypic adhesion were formed upon A1 or $F(ab)_2$_A1 treatment, not monovalent Fab_A1. Representative images are shown.

6.4 A1-induced hESC death is associated with actin re-organization

Homotypic adhesion, microvilli degradation and plasma membrane damage all implied the involvement of actin cytoskeleton in A1-induced hESC death. Actin cytoskeleton undergoes constant formation and remodelling, which contributes to its roles in cell motility, cell signalling and the establishment and maintenance of cell junctions and cell shape. Here, different assays were performed to study the role of actin in A1-induced hESC death.

6.4.1 A1 treatment induces reduction of actin-association proteins

Firstly, similar to mAb84-induced hESC oncosis[34], significant reduction of four actin-associated proteins in A1-treated hESC compared to non-treated hESC was observed, namely, α-actinin, paxillin, talin and vinculin (Figure 6-16).

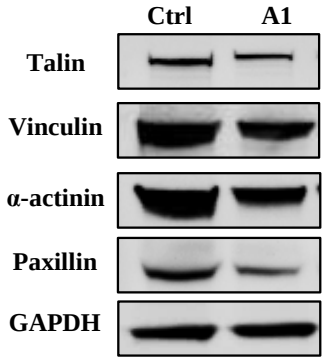

Figure 6-16: A1 treatment induced reduction of actin-associated proteins.
Human ESC were harvested in single-cell suspension, treated with A1 or PBS- control for 45 minutes. After incubation, cells were washed and lysed in 2% Triton/PBS-. Reduction of actin-associated proteins, namely, talin, vinculin, α-actinin and paxillin, after A1 treatment was detected. GAPDH was used as an endogenous control. Representative data are shown.

6.4.2 Inhibitors of actin polymerization can partially block A1 cytotoxicity

A previous study on mAb RE2-mediated T cells oncosis identified that treatment with Cytochalasin B/D completely blocks the cytotoxicity of mAb RE2 towards T cells[71]. We therefore investigated the effect of Cytochalasin B, Cytochalasin D and Latrunculin A on A1-induced hESC death. In general, Cytochalasin B/D inhibits actin polymerization by blocking the fast growing end of actin polymer[142], whereas Latrunculin A binds to G actin and prevents polymerization of actin monomers[143]. Briefly, hESC was pre-incubated with optimized amount of Cytochalasin B/D or Latrunculin A for 5 minutes and the cell-inhibitor mixture were incubated with A1 for another 45 minutes. As negative control, cells were pre-incubated with the same volume of PBS- or

DMSO as that of the inhibitors. Cell viability was assessed by PI uptake. In Figure 6-17, upon A1 treatment, inhibitors-treated hESC had a reduction in cell death compared to the non-treated controls, suggesting a functional link between actin polymerization and A1-induced hESC death.

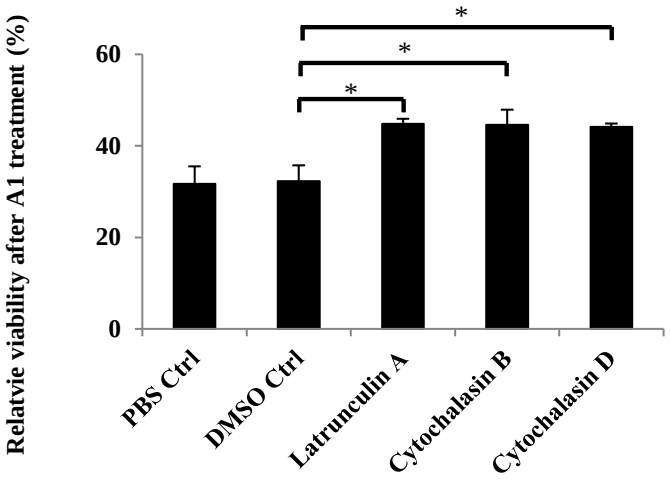

Figure 6-17: Association between actin polymerization and A1 cytotoxicity on hESC. Human ESC (2 x 10^5 cells in 100 µl) were pre-incubated with the actin inhibitors: Latrunculin A (4 µg), cytochalasin B (4 µg), and cytochalasin D (4 µg) for 5 minutes before A1 treatment. Cell viability was assessed with PI uptake. A1 cytotoxicity on hESC was partially inhibited upon actin inhibitors (latrunculin A, Cytochalasin B, and Cytochalasin D) treatment. Data are represented as mean ± SEM. P values for t-test: * < .05, ** < .01, *** < .001.

6.4.3 A1 induces F-actin enrichment and G-actin re-localisation in hESC

Studies by Alduaij et al. on GA101, an mAb targeting type II CD20 showed that peripheral relocalization of actin cytoskeleton is critical for GA101-induced lymphoma oncosis and homotypic adhesion[75]. Hence, we investigated whether there is alteration of F-actin and G-actin in hESC upon A1 treatment. Briefly, hESC were harvested as a single-cell suspension and incubated with A1 for 45 minutes. After incubation, excess A1 were washed off and cells were fixed before loading onto poly-L-lysine-coated plates. As a negative control, hESC were treated with PBS-. Immuno-staining of F-actin and G-actin revealed that A1 treatment evoked the relocalization of G-actin from the nucleus to cytoplasm and the enrichment of F-actin at cell-cell adhesion sites

(Figure 6-18). Enrichment of F-actin upon A1 treatment further confirmed that actin polymerization is involved in A1-induced hESC death. Moreover, enrichment at cell-cell adhesion sites could be associated with homotypic adhesion.

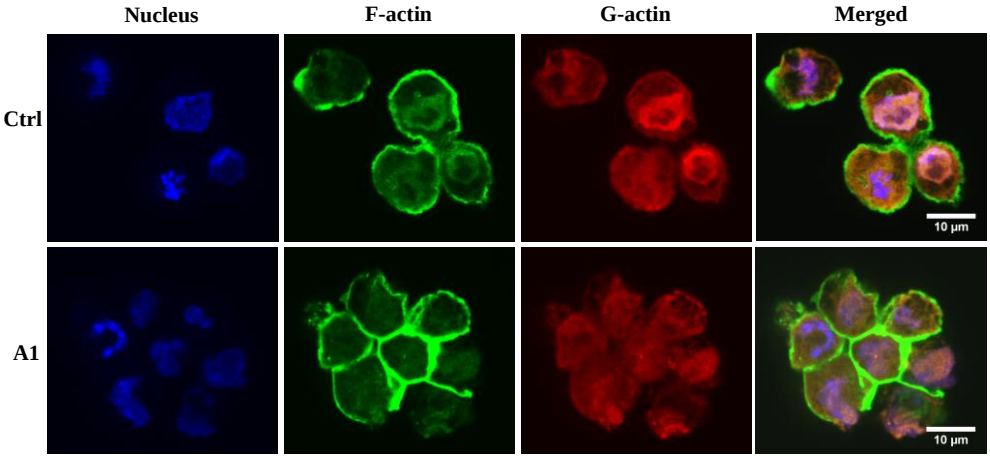

Figure 6-18: Re-distribution of F-actin and G-actin in A1-treated hESC.
A1 treatment led to enrichment of F-actin at cell-cell adhesion cites and G-actin translocation from nucleus to cytoplasm. Representative images are shown. F-actin was labelled with Alexa Fluor 488 Phalloidin, nucleus was stained with Hoechst blue, and G-actin was labelled with Deoxyribonuclease I, Alexa Fluor 594 Conjugate.

6.4.4 Summary

In this section, the role of actin cytoskeleton in A1-induced hESC death was studied. Upon A1 treatment, reduction of four actin-associated proteins (talin, vinculin, α-actinin, and paxillin) was observed. Moreover, inhibitors of actin polymerization partially blocked A1 cytotoxicity on hESC, which was further supported by the enrichment of F-actin at cell-cell adhesion sites and the re-localisation of G-actin from nucleus to cytoplasm. Taken together, these results demonstrated a close association between actin re-organization and A1-induced hESC death.

6.5 A1-induced hESC death is mediated by excess reactive oxygen species (ROS) production from NADPH oxidase

6.5.1 Introduction

ROS are chemically highly reactive molecules containing oxygen, such as superoxide, hydrogen peroxide, hydroxyl radicals and peroxynitrite. Under normal conditions, ROS can perform multiple functions in living organism, such as signalling cell growth/differentiation and maintaining cell homeostasis[144,145]. However, ROS level can increase drastically upon stimulation, such as hypoxia[146], serum deprivation[147], apoptosis[148] and integrin signalling[149]. Excessive amount of ROS would lead to irreversible oxidative damages to DNA, lipids, proteins and enzymes[150–152]. ROS production has been reported in different types of cell death including apoptosis[153], autophagy[154] and oncosis[155,156], though it is still unclear whether the production of ROS is always an essential component. Several studies have reported the excess production of ROS in mAb-induced cell death[76,157–160].The modes of mAb-induced cell death involving ROS production are either apoptosis or oncosis. Studies involving mAb GA101 targeting human B-lymphoma cells, demonstrated that by depleting ROS with scavengers, GA101-induced cell death can be partially inhibited[76]. They have also demonstrated that GA101 kills human B-lymphoma cells via a non-apoptotic pathway with features of homotypic adhesion and plasma membrane damage[74,75], which are also observed in A1-induced hESC death. Therefore, we hypothesized that ROS might also play an essential role in A1-induced hESC death.

6.5.2 A1 induces excess ROS production in hESC

First, we investigated whether ROS is produced in A1-treated hESC. After A1

treatment, cells are incubated with dihydroethidium (HE) staining which when oxidized by ROS emits red fluorescence. From Figure 6-19, there was a distinct population of cells with higher fluorescence in the A1 treated condition thus suggesting that A1 treatment led to a significant increase in the level of ROS.

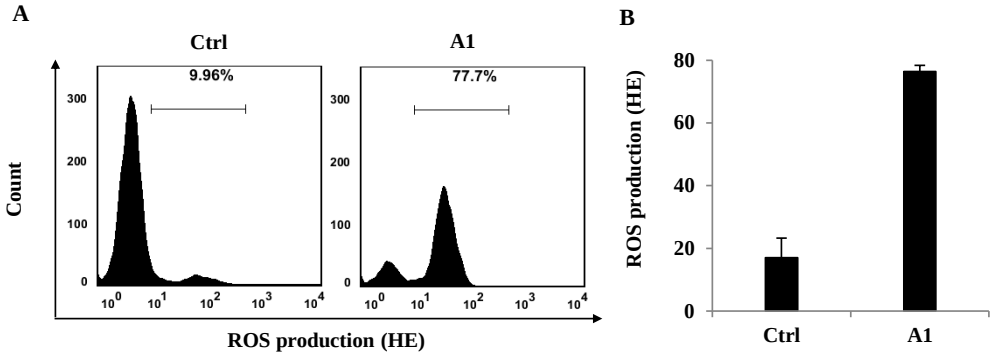

Figure 6-19: A1-induced ROS production measured via HE staining by flow cytometry. Human ESC (2 x 10^5 in 100 µl) were treated with 5 µg of A1 or PBS- control for 45 minutes at 4°C. ROS production was then determined 30 minutes after incubation with HE (25 µM). In the presence of ROS, HE is oxidized to emit red fluorescence. (A) The amount of ROS production as measured via HE staining was quantified by flow cytometry analysis. Gated population represents increased level of ROS production. Representative histograms are shown. (B) A1 treatment induced excess ROS production (measured by HE staining) in hESC. Data are represented as mean ± SEM.

Alternatively, ROS production was determined using carboxy-H2DCFDA staining under light microscopy. In the presence of ROS, carboxy-H2DCFDA is oxidized to carboxy-DCF that emits green fluorescence. Similar to HE staining, there was an increased level of carboxy-DCF green fluorescence detected after A1 treatment (Figure 6-20) indicative of elevated ROS production induced by A1.

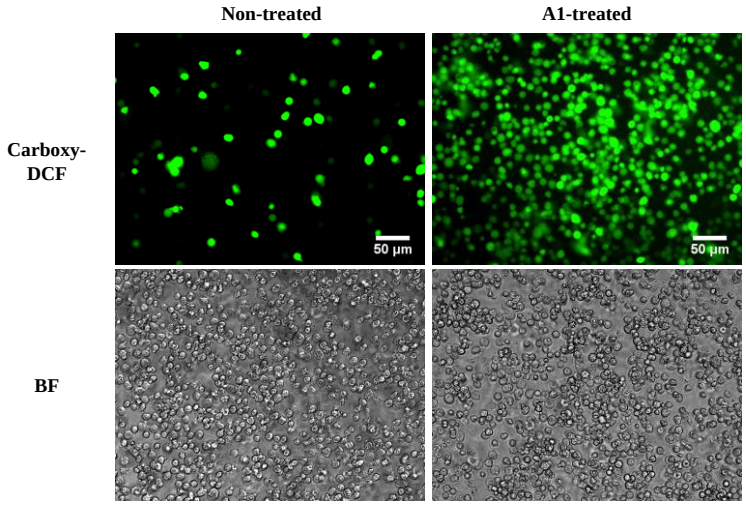

Figure 6-20: A1-induced ROS production measured via carboxy-H2DCFDA staining by fluorescence microscopy.
A1 (5 µg) was directly added to the 96-well flat-bottomed plate with 2 x 10^5 hESC which were pre-incubated with carboxy-H2DCFDA. In the presence of ROS, carboxy-H2DCFDA is oxidized to carboxy-DCF that emits green fluorescence. Images were taken 30 minutes after A1 treatment.

6.5.3 A1-induced hESC death correlates with ROS production

To examine the relationship between ROS production and cell death, hESC were dual stained with Sytox green to identify dead cells and HE for ROS production (Figure 6-21). After A1 treatment, there was a significant increase in the cell population localised in the upper right quadrant of the scatter plot (Fig 6-21) which represents dead cells with high level of ROS production. Hence, ROS production directly correlates with hESC death upon A1 treatment.

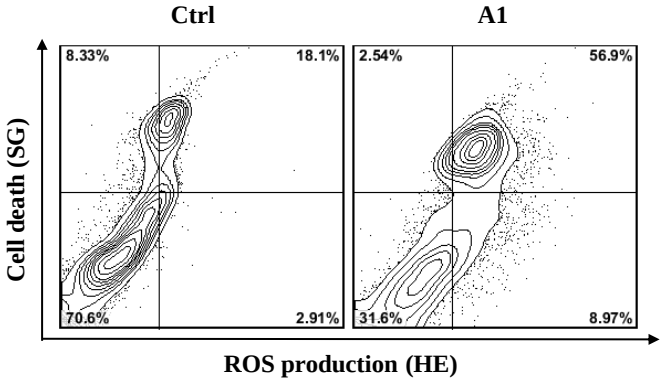

Figure 6-21: A1-induced hESC death and ROS production were directly correlated.
Human ESC (2 x 10^5 in 100 µl) were treated with 5 µg of A1 or PBS- control for 45 minutes at 4°C. Cell death (Sytox Green uptake) and ROS production (HE intensity) was quantified by flow cytometry analysis. Representative scatter plots are shown.

6.5.4 ROS production is essential for A1-induced hESC death

Having established a direct correlation between A1-induced hESC death and ROS production, we investigated whether ROS production is an essential step in A1-induced hESC death. Using ROS scavengers: Tiron and Tempol, which are well-characterized superoxide dismutase (SOD) mimetic[161–163], the extent of cell killing by A1 was compared. Briefly, hESC were pre-incubated with Tiron or Tempol for 1 hour before treatment with A1. Cell viability after A1 treatment was estimated by PI uptake. It was clear that pre-treatment of hESC with both Tiron and Tempol significantly inhibited A1-induced hESC death (Figure 6-22), indicating that excess ROS production is required for A1 killing of hESC.

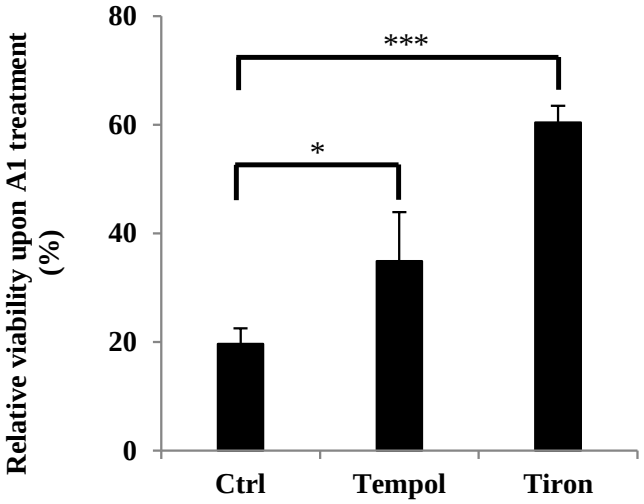

Figure 6-22: ROS scavengers partially blocked A1-induced hESC death.
Before A1 treatment, cells were treated with PBS- or the ROS scavengers (Tiron 50mM or Tempol 120mM) for 1 hour. Cell viability was assessed via PI uptake by flow cytometry analysis. Data are represented as mean ± SEM. P values for t-test: * < .05, ** < .01, *** < .001.

By dual staining hESC with Sytox green and HE, we proved that depletion of ROS by Tiron correlated with a decrease in A1-induced cell death (Figure 6-23), which clearly establishes the essential role of ROS in A1-induced hESC death. For both Tiron and Tempol, the mechanism of action is to convert

superoxide (O^2) to hydrogen peroxide[163], suggesting that the superoxide is the form of ROS responsible for A1-induced hESC death.

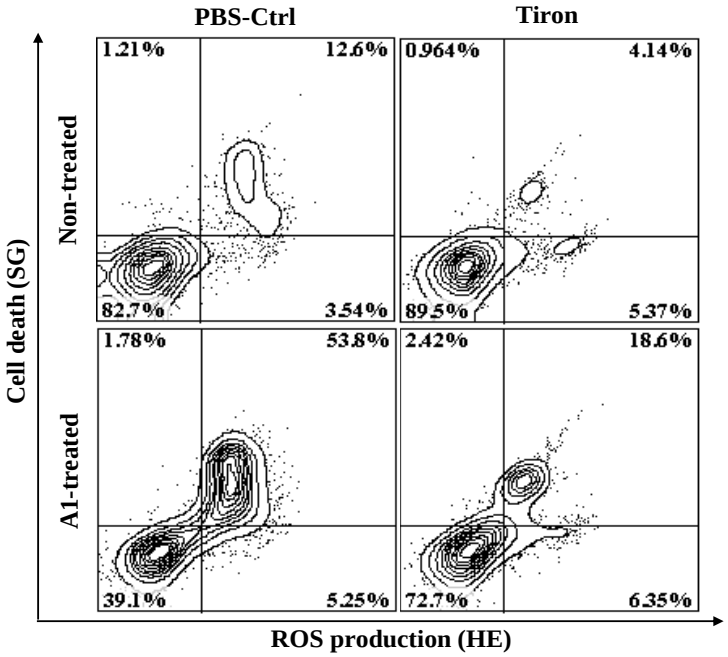

Figure 6-23: Depletion of ROS production was directly correlated with decreased A1-induced hESC death.
Before A1 treatment, cells were treated with PBS- or Tiron (50mM) for 1 hour. Cell death (Sytox Green uptake) and ROS production (HE intensity) was quantified by flow cytometry analysis. Representative scatter plots are shown. Population in upper right quadrant represents dead cells with excess ROS production.

6.5.5 Source of A1-induced ROS production in hESC

Knowing ROS production is essential for A1-induced hESC death, we went on to explore the upstream source of A1-induced ROS production in hESC. In living cells, ROS can be produced by several sources including endothelial nitric oxide synthases, mitochondria (complex I and complex III), xanthine oxidase, 5-lipoxygenase and nicotinamide adenine dinucleotide phosphate-oxidase (NADPH oxidases)[164]. However, the sources of superoxide production, which are most dominant and relevant to cell death, would be mitochondria and NADPH oxidases. Mitochondria O^{2-} was commonly reported in apoptosis studies[165] whereas O^{2-} from NADPH oxidases can be

involved in both apoptosis and oncosis[166]. Another study also reported that an initial generation of ROS by NADPH oxidases is needed to trigger the release of ROS by other enzymes[167]. Moreover, NADPH oxidase has been reported to be the source of GA101-induced ROS production in human B-lymphoma cells[76]. Since we have demonstrated that A1 induces hESC death via oncosis, we hypothesized that A1 induces ROS production and eventually hESC death via the activation of NADPH oxidase.

NADPH oxidase is a membrane-bound enzyme complex which transfers electrons across biological membranes to free oxygen and generate ROS, more specifically superoxide anions (O^{2-})[168]. There are seven NOX homologues of NADPH oxidase, namely Nox1-Nox5, Duox1 and Duox2. Some structural properties have been highly conserved among all seven NOX homologues (Figure 6-24A): six membrane-spanning domains, four heme-binding domains, NADPH-binding sites and FAD binding sites[168]. Despite their similarities in structural properties and enzymatic function, NOX homologues differ in their mechanism of assembly or activation[169,170] (Figure 6-24B).

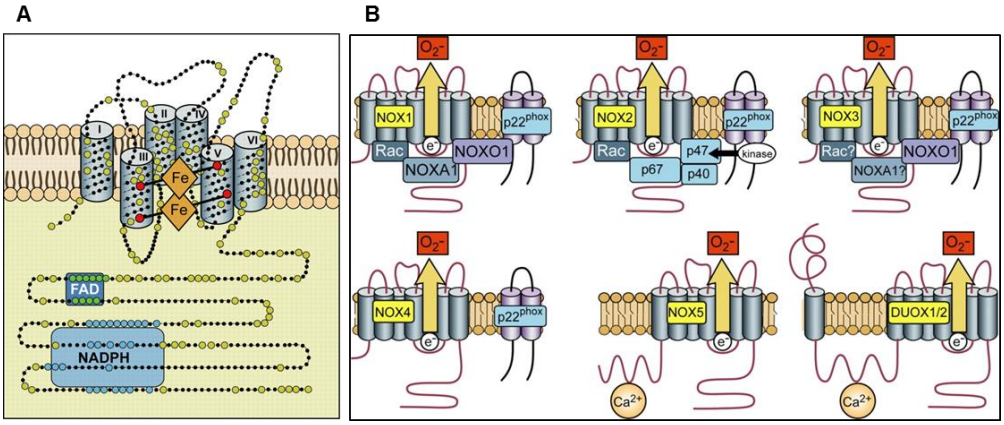

Figure 6-24: Isoforms of NADPH oxidases[168].
(A) Conserved structural properties of all seven Nox isoforms of NADPH oxidase; (B) Different assembly mechanism of Nox isoforms of NADPH oxidase.

The first identified and most thoroughly studied isoform of NADPH oxidase is Nox2, or gp91phox. Nox2-NADPH oxidase consists of two membrane-bound subunits: Nox2 (glycoprotein, 91 kDa) and p22phox (22 kDa) and at least three cytoplasmic subunits: the small GTPase Rac2, p47phox and p67phox[168–170]. Later studies also identified two more proteins involved in the complex assembly and activation: Rap1a[171,172] and p40phox[173,174].

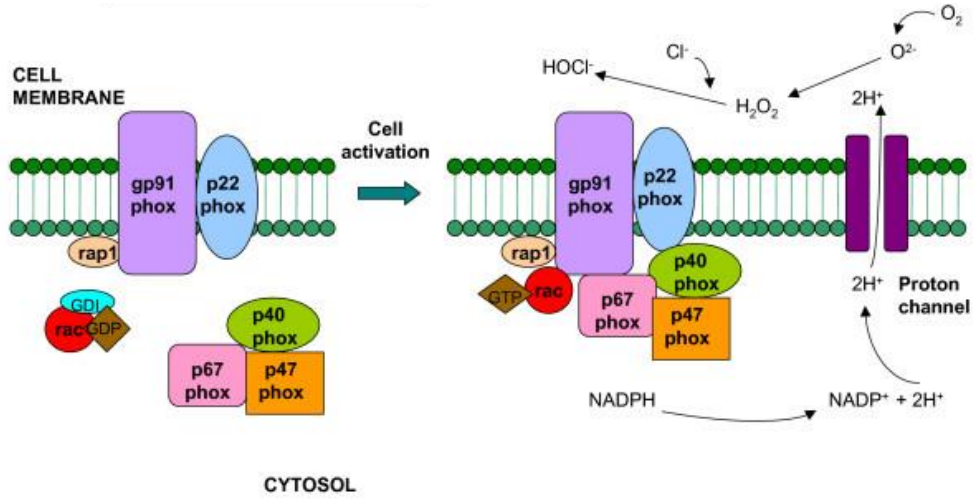

Figure 6-25: Assembly and activation of Nox2-NADPH oxidase[164]
(Left) Before activation: cytosolic components (p67phox, p40phox, p47phox, and Rac-GDP), transmembrane components (gp91phox/Nox2, p22phox, and rap1). (Right): After activation: NADPH oxidase complex transfers electron to oxygen to generate superoxide and convert NADPH to $NADP^+$.

Nox2 constitutively interacts with p22phox to form a cytochrome b558 complex, which is essential for its oxidase activity (Figure 6-25). Activation stimuli lead to phosphorylation of p47phox and its subsequent conformational change allowing its interaction with p22phox. As an "organizer subunit", localised p47phox then brings the "activator subunit" p67phox into contact with Nox2 as well as the small subunit p40phox to the complex. Activation stimuli also lead to the activation Rac-GDP to Rac-GTP, allowing translocation of Rac-GTP to the plasma membrane to interact with Nox2 and p67phox. Upon successful assembly, the active NADPH oxidase complex

would transport electrons from cytoplasmic NADPH to extracellular oxygen to generate superoxide (O^{2-}).

6.5.5.1 Activity of NADPH oxidase increases upon A1 treatment

To investigate the involvement of NADPH oxidase in A1-treated hESC death, the activity of NADPH oxidase was estimated by measuring NADP/NADPH ratio. Upon activation of NADPH oxidase, NADPH will be oxidized to $NADP^+$ with the production of superoxide. Briefly, hESC were treated with A1 or PBS- control and lysed for the extraction of NADPH and $NADP^+$. A1-treated hESC has significantly higher NADP/NADPH ratio than that of non-treated hESC (Figure 6-26), indicating NADPH oxidase in A1-treated hESC are highly active.

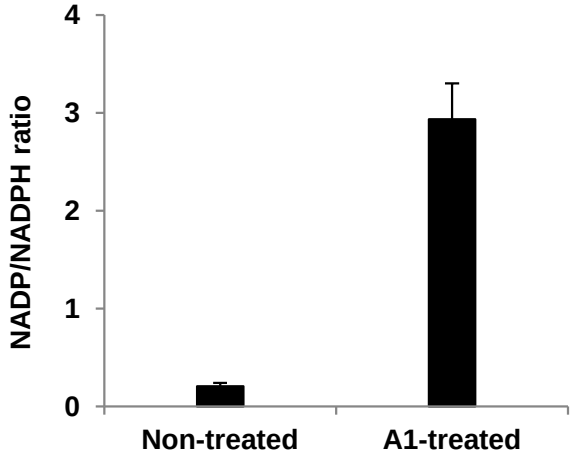

Figure 6-26: Increased NADPH oxidase activity in A1-treated hESC.
Activity of NADPH oxidase as measured via $NADP^+$/NADPH ratio in hESC significantly increase upon A1 treatment. Data are represented as mean ± SEM.

6.5.5.2 Inhibitor of NADPH oxidase partially blocks A1-induced hESC death

Next, to confirm that NADPH oxidase is responsible for the production of superoxide in hESC, three inhibitors of NADPH oxidase, Diphenyleneiodonium chloride (DPI), Mycophenolic acid (MPA), and Apocynin or Acetovanillone (APO) were used. DPI acts by abstracting an

electron from the redox centre of NADPH oxidase and forming a radical which then inhibits electron transfer from NADPH to oxygen[175]. MPA depletes cellular GTP and consequently inhibits Rac activation[176]. Apocynin prevents the assembly of the NADPH oxidase subunits by inhibiting the translocation of cytosolic components to plasma membrane[177]. Briefly, cells were pre-incubated with inhibitors for 1 hour prior to the addition of A1. For the negative control, cells were pre-incubated with the same volume of DMSO. After A1 treatment, cell viability in different treatment conditions was estimated by PI uptake and normalized to their respective non-A1-treatment controls. Pre-treatment with these inhibitors significantly attenuated A1 killing on hESC (Figure 6-27).

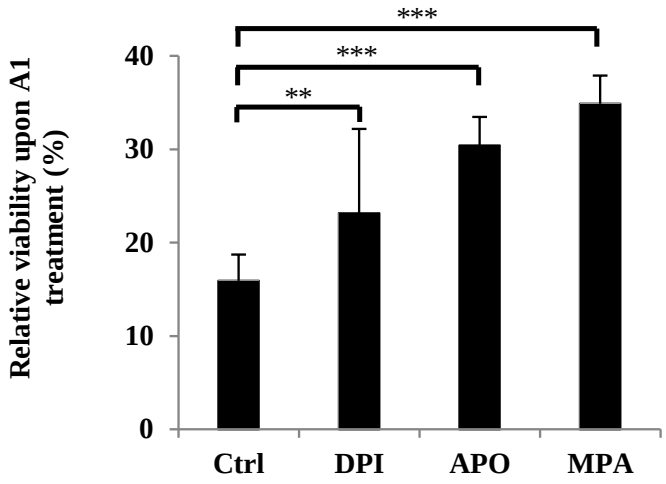

Figure 6-27: Inhibitors of NADPH oxidase can partially block A1-induced hESC death. Before A1 treatment, cells were treated with DMSO or inhibitors of NADPH oxidase (DPI 240 mM, or Apo 40 mM, or MPA 3.12 mM) for 1 hour. Cell viability in different treatment conditions was estimated by PI uptake and normalized to their respective non-A1-treatment controls. Data are represented as mean ± SEM. P values for t-test: * < .05, ** < .01, *** < .001.

To confirm that the inhibitors are blocking A1 cytotoxicity on hESC via inhibiting NADPH oxidase, hESC were dual stained with Sytox green to identify dead cells and HE for ROS production. Decrease in cell death corresponds to the inhibition of ROS production (Figure 6-28), suggesting that

NADPH oxidase is the source of A1-induced ROS production and it is essential for A1 to elicit cytotoxicity on hESC.

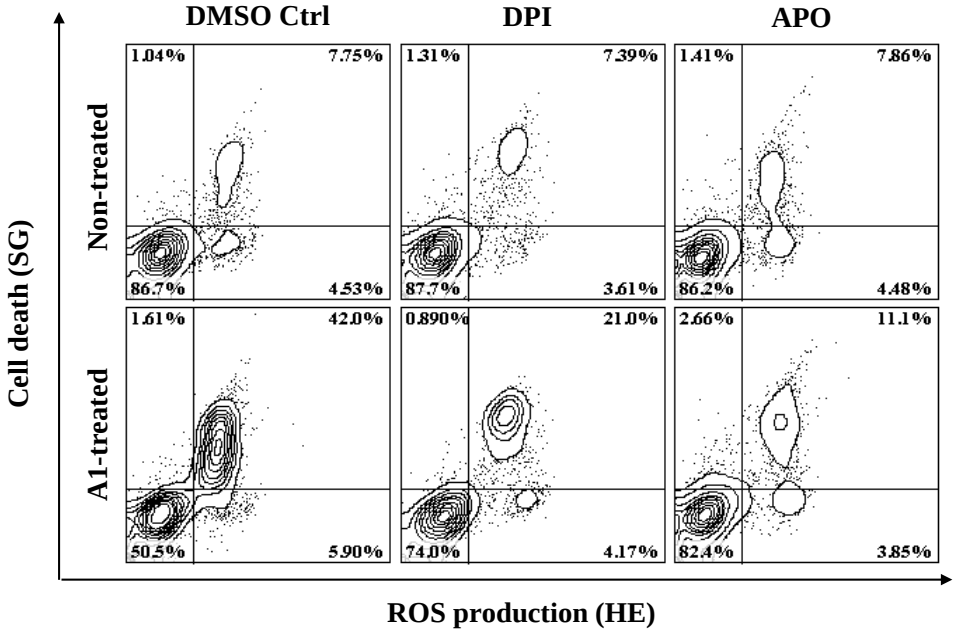

Figure 6-28: Inhibition of ROS production was directly correlated with decreased A1-induced hESC death.
Before A1 treatment, cells were treated with DMSO or inhibitors of NADPH oxidase (DPI 240 mM, or Apo 40 mM) for 1 hour. Human ESC were dual stained with Sytox green and HE to detect cell death and ROS production respectively. Representative scatter plots are shown. Population in upper right quadrant represents dead cells with excess ROS production. After A1 treatment, hESC with inhibitors treatment have a significant decrease in ROS production and cell death.

6.5.5.3 Nox2 is the mediator of A1-induced ROS production and hESC death

As discussed previously, there are seven isoforms of NADPH oxidase. We next explored which isoform or isoforms are responsible for A1-induced ROS production. Among the seven isoforms, activation of Nox1, Nox2, and Nox3 requires the assembly of cytoplasmic and membrane-bound subunits as well as Rac activation (Figure 6-24B). On the contrary, activation of other isoforms does not involve any cytoplasmic subunits as well as Rac activation. Therefore, since both APO and MPA can inhibit ROS production and A1 killing, their target isoforms are likely to be Nox1-Nox3. Since there is lack of knowledge about the role of Nox isoforms in hESC and Nox2 has been

reported to produce ROS in GA101-treated lymphocytes[76], we first investigated whether Nox2 is responsible for A1-induced ROS production.

Two different siRNAs (siNox2_s3787 and siNox2_s3788) were used to down-regulate Nox2 expression in hESC. Briefly, prior to transfection, cells were pre-incubated with ROCK inhibitor to preserve cell viability. After incubation, cells were then dissociated into single-cell suspension and incubated in siNox2 or scramble siRNA. After 10-15 minutes incubation, the suspension was seeded on matrigel-coated plates, maintained with daily fresh mTeSR and harvested 4-5 days after transfection for various assays. Firstly, transfection efficiency was verified using qRT-PCR and western blotting. Upon siNox2 transfection, the RNA expression of Nox2 in transfected hESC decreased by about 50% compared to hESC transfected with scramble siRNA control (Figure 6-29A). Significant reduction of Nox2 protein expression was also observed in western blotting (Figure 6-29B).

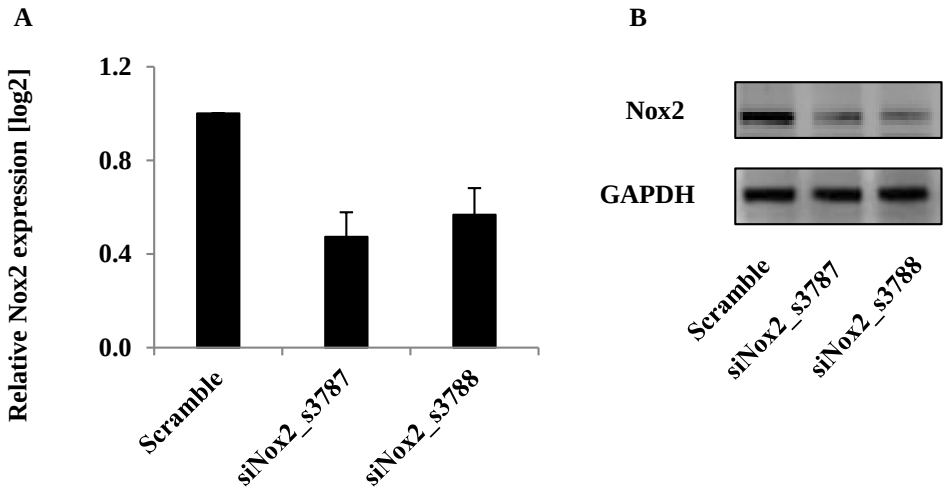

Figure 6-29: Nox2 expression was partially down-regulated with siNox2.
(A) Knockdown of Nox2 was confirmed via measured Nox2 RNA expression level by qRT-PCR. Data are represented as mean ± SEM. (B) Knockdown of Nox2 was confirmed by western blotting.

The expression of pluripotency marker, Tra-1-60, after transfection was also determined. There was no difference in the binding of anti-Tra-1-60 antibody between siNox2-transfected and scramble control transfected hESC (Figure 6-30), indicating that expression of pluripotency marker, Tra-1-60, was not affected by the knockdown of Nox2.

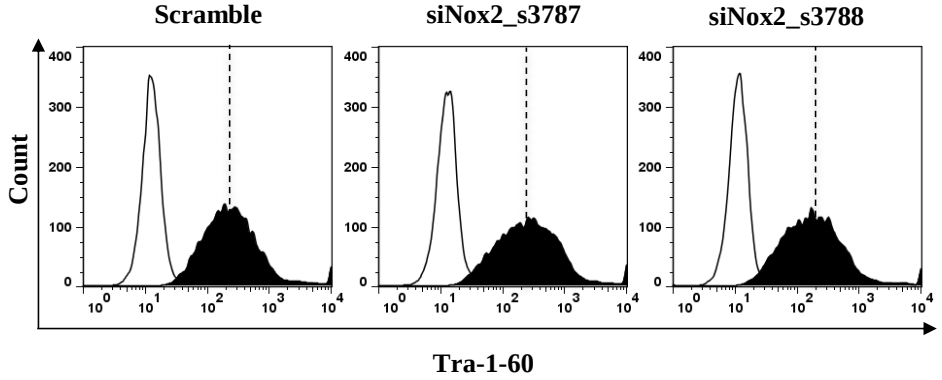

Figure 6-30: Expression of pluripotency marker Tra-1-60 of hESC was maintained upon siNox2 transfection.
Pluripotency marker expression of hESC (Tra-1-60) upon Nox2 knockdown was confirmed via flow cytometry analysis. Representative histograms are shown. Open histogram represents non-primary antibody control. Shaded histogram represents cells with anti-Tra-1-60 antibody treatment.

Similarly, there was no significant difference observed in A1 binding between the two conditions (Figure 6-31), indicating that Nox2 is not an antigen target of A1 on hESC.

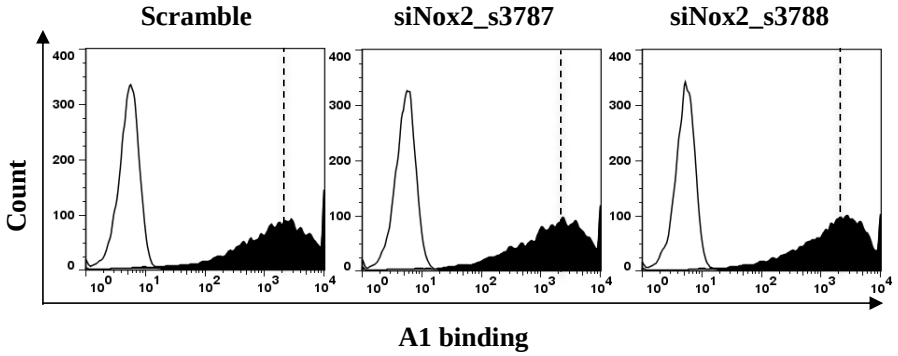

Figure 6-31: A1 binding was not affected upon Nox2 knockdown.
2 x 10^5 siNox2-transfected hESC or hESC with scramble control (100 µl) were treated with 5 µg of A1 or PBS- control for 45 minutes at 4^{o}C. Binding of A1 was assessed with FITC-conjugated secondary antibody by flow cytometry analysis. Representative histograms are shown. Open histogram represents no A1 treatment control and shaded histogram represents A1-treated cells.

However, with down-regulation of Nox2 expression, A1-induced hESC death was significantly attenuated (Figure 6-32). Increase in the viable cell population correlated to the percentage of siNox2-knockdown cells, suggesting Nox2 is responsible for A1-induced ROS production and hESC death.

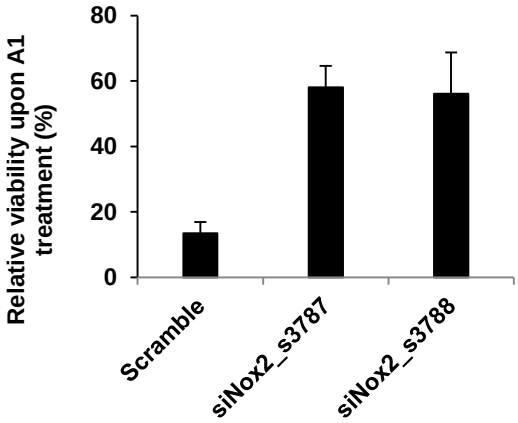

Figure 6-32: A1 cytotoxicity on hESC was down-regulated upon Nox2 knockdown.
siNox2-transfected hESC or scramble control transfected hESC (2 x 10^5 in 100 µl) were treated with 5 µg of A1 or PBS- control for 45 minutes at 4^{o}C. Cell viability was assessed via PI uptake by flow cytometry analysis. Data are represented as mean ± SEM.

As neither Nox2 knockdown nor inhibition of A1-induced hESC death was complete, it is still unclear whether Nox2 is the only mediator of A1-induced hESC death. We continued to assess the expression of Nox1 and Nox3 in hESC by western blotting and immuno-staining. Nox1 expression was not detected in western blotting whereas Nox3 was detected around the predicted molecular weight of 51 kDa (Figure 6-33A) and distributed in the cytoplasm as well as the plasma membrane of the cell (Figure 6-33B).

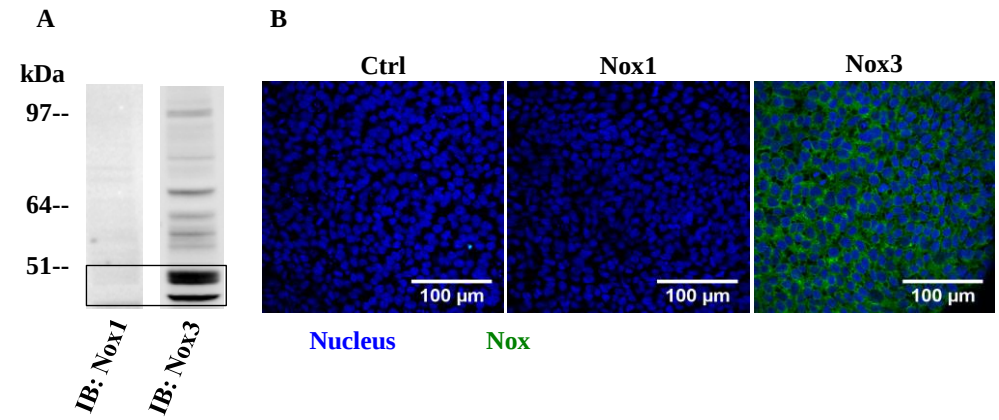

Figure 6-33: Expression of Nox1 and Nox3 in hESC.
(A) Nox3 expression in hESC was detected at 51kDa by western blotting. However, Nox1 was not detected. (B) Nox3 expression in hESC was detected at cell cytoplasm and plasma membrane by immuno-staining, but not Nox1. Nucleus was stained with Hoechst blue. Nox proteins were stained with Alexa Fluor-488.

To investigate the role of Nox3 in A1-induced hESC death, Nox3 expression was down-regulated with siRNA. Transfection efficiency was verified using western blotting (Figure 6-34A) and pluripotency (Tra-1-60 expression) of hESC after transfection was confirmed using flow cytometry analysis (Figure 6-34B).

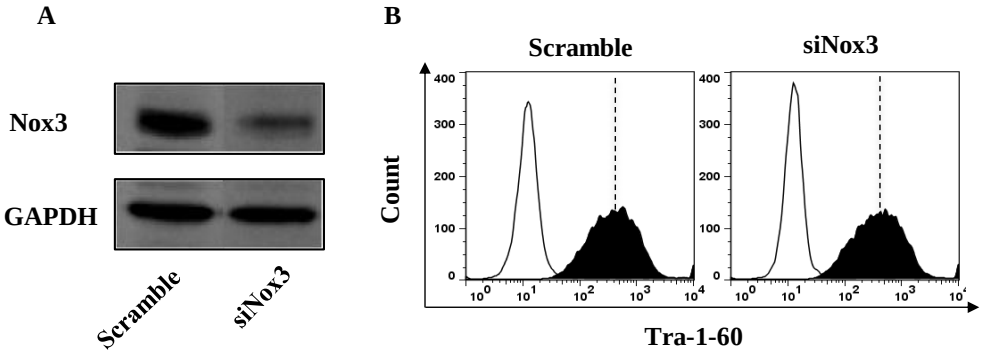

Figure 6-34: Nox3 was partially knockdown in hESC while hESC pluripotency was maintained.
(A) Knockdown of Nox3 was confirmed by western blotting. (B) Pluripotency of hESC (Tra-1-60) upon Nox2 knockdown was confirmed via flow cytometry analysis. Representative histograms are shown. Open histogram represents non-primary antibody control. Shaded histogram represents cells with anti-Tra-1-60 antibody treatment.

Though with similar transfection efficiency as Nox2, down-regulation of Nox3 did not significantly affect A1 killing on hESC (Figure 6-35), suggesting Nox3 is not a mediator of A1-induced hESC death.

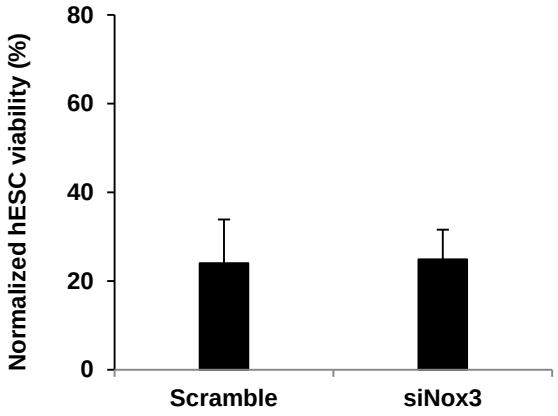

Figure 6-35: A1 cytotoxicity on hESC was not affected upon Nox3 knockdown.
siNox3-transfected hESC or scramble control transfected hESC (2 x 10^5 in 100 µl) were treated with 5 µg of A1 or PBS- control for 45 minutes at 4°C. Cell viability after A1 treatment was assessed via PI uptake. Data are represented as mean ± SEM.

6.5.6 Mitochondrial depolarization is a consequence of A1-induced ROS production.

Since NADPH oxidase activity was not completely blocked by either inhibitors or siNox2 knockdown, we were unable to prove that Nox2-NADPH oxidase is the only source of A1-induced superoxide production. Besides NADPH oxidase, excess production of superoxide from mitochondrial after mitochondrial membrane permeabilization has been reported in apoptosis[178]. Moreover, mitochondrial impairment was also observed in GA101-induced lymphocytes death[76]. Therefore, we used potentiometric dye JC-1 to assess mitochondrial impairment by measuring mitochondrial depolarization. JC-1 exhibits potential-dependent accumulation. JC-1 monomers emit green fluorescence (~529 nm) whist JC-1 aggregates emit red fluorescence (~590nm). Mitochondrial depolarization is detected by a decrease in the

red/green fluorescence intensity ratio. Upon A1 treatment, an increase in mitochondrial depolarization was observed (Figure 6-36), indicating A1 treatment can induce hESC mitochondrial impairment.

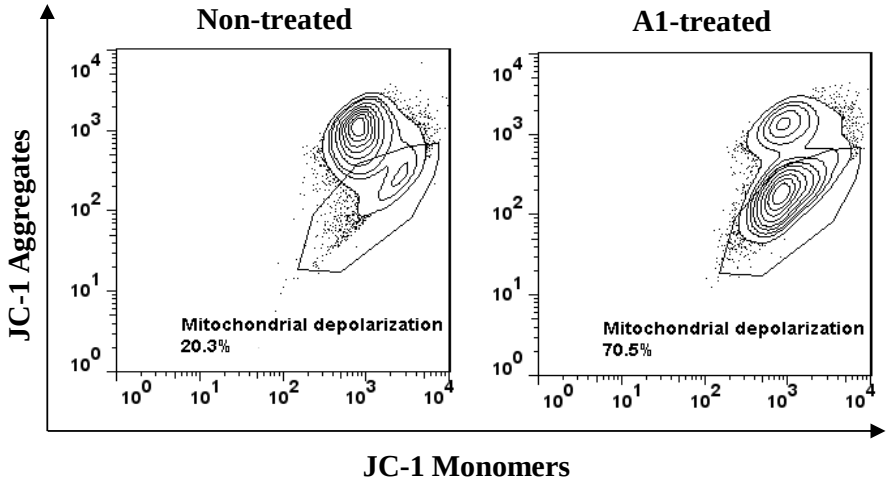

Figure 6-36: A1 induced hESC mitochondrial impairment.
Human ESC (2 x 10^5 in 100 µl) were treated with 5 µg of A1 or PBS- control for 45 minutes at 4°C. Mitochondrial permeabilization was estimated with JC-1 dye by flow cytometry analysis. JC-1 exhibits potential-dependent accumulation. JC-1 monomers emit green fluorescence (~529 nm) whist JC-1 aggregates emit red fluorescence (~590 nm). Mitochondrial depolarization is indicated by a decrease in the red/green fluorescence intensity ratio. Representative scatter plot was shown. Gated population represents cells with mitochondrial membrane depolarization.

We therefore wanted to know whether mitochondrial membrane permeabilization is another source of A1-induced superoxide production. However, by down-regulating Nox2 expression in hESC, JC-1 measured mitochondrial depolarization was reduced correlating to the attenuation in cell death (Figure 6-37), suggesting mitochondrial depolarization is a consequence of A1-induced Nox2 activation. Therefore, the mitochondrion is unlikely an alternative source of superoxide production besides Nox2-NADPH oxidase.

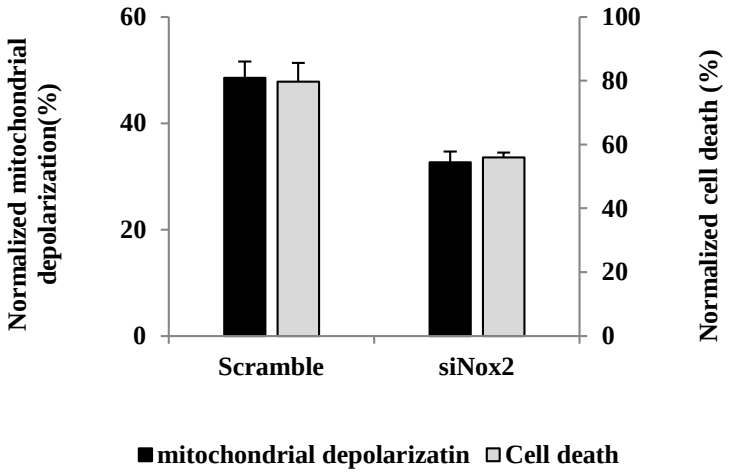

Figure 6-37: Mitochondrial depolarization was down-regulated upon Nox2 knockdown. Upon A1 treatment, mitochondrial depolarization and cell death (PI uptake) were measured in scramble and Nox2-knockdown hESC. JC-1 dye exhibits potential-dependent accumulation in mitochondria. JC-1 aggregates emit red fluorescence whereas JC-1 monomers emit green fluorescence. Mitochondrial depolarization is indicated by a decrease in the red/green fluorescence intensity ratio. Data are represented as mean ± SEM.

6.5.7 Summary

In this section, the role of excess reactive oxygen species (ROS) production in A1-induced hESC was studied. First, excess ROS production was detected via HE staining by flow cytometry analysis and H2DCFDA staining by fluorescent microscopy. By using two ROS scavengers (Tiron and Tempol) targeting superoxide, the essential role of excess superoxide production was identified. Significant increase in NADPH oxidase activity as well as partially inhibited A1 cytotoxicity by NADPH oxidase inhibitors implied that NADPH oxidase was the source of A1-induced ROS production, which was subsequently confirmed by the knockdown of Nox2 isoform. Moreover, mitochondrial impairment was shown to be a consequence of A1-induced ROS production, instead of the source.

6.6 What is the sequence of observed events?

So far, several events have been observed during A1-induced hPSC death including microvilli degradation, homotypic adhesion, actin cytoskeleton re-organization, plasma membrane damage and ROS production. To have a clearer understanding of the killing mechanism, we therefore aimed to delineate the order of these observed events. Given the functional significance of ROS production in A1-induced hESC death, we were interested to investigate where along the oncolytic cell death pathway is ROS production effecting.

6.6.1 A1-induced ROS production occurs downstream of microvilli degradation, and upstream of plasma membrane damage

The effect of ROS depletion on A1-induced morphological changes was assessed by SEM. Similar to hESC in PBS- control, Tiron-treated hESC also resulted in microvilli degradation upon A1 treatment (Figure 6-38). However, Tiron-treated hESC retained a uniform cell size and morphology without plasma membrane damage (Figure 6-38), indicating that ROS production lies downstream of microvilli degradation, and upstream of plasma membrane damage.

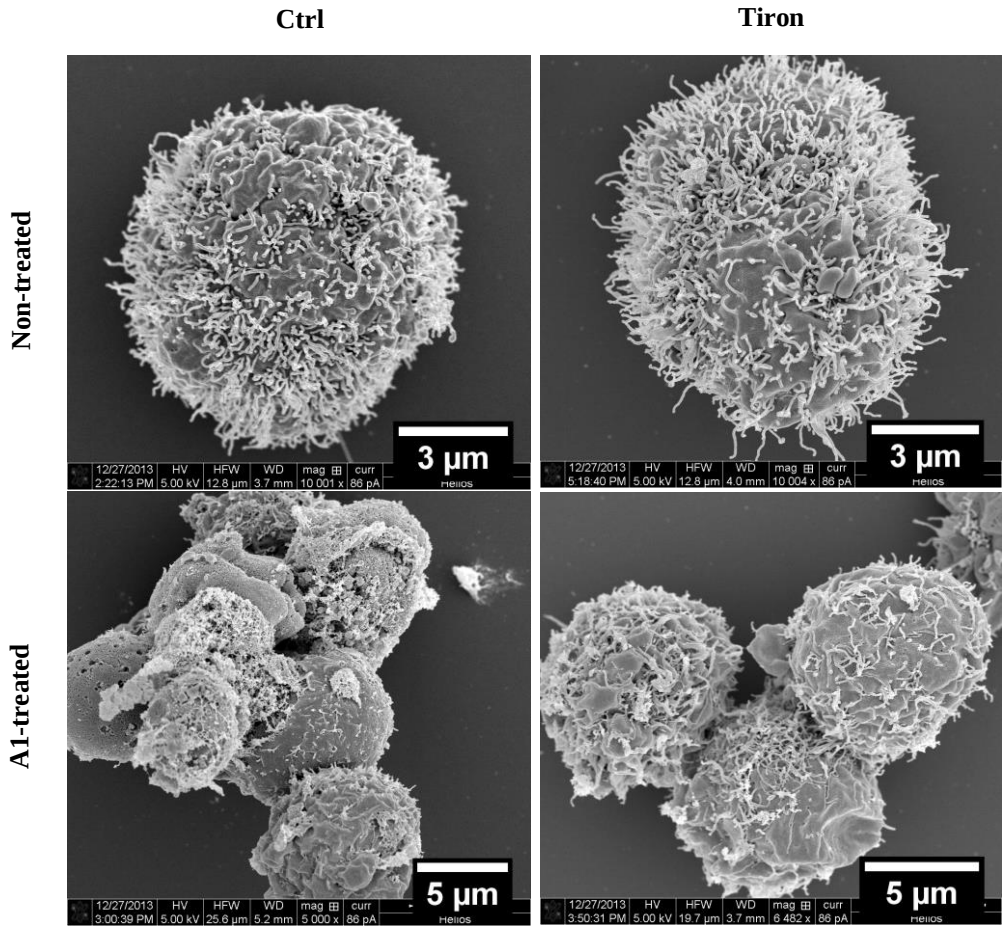

Figure 6-38: ROS production occurs downstream of microvilli degradation, but upstream of severe plasma membrane damage.
Before A1 treatment, 2 x 10^5 cells (100 µl) were treated with PBS- or Tiron (50 mM) for 1 hour. Cell morphology was observed under SEM. Representative images are shown. ROS depletion by Tiron did not prevent microvilli degradation, but plasma membrane damage after A1 treatment.

6.6.2 A1-induced ROS production occurs downstream of homotypic adhesion

Next, the effect of ROS depletion by Tiron on A1-induced homotypic adhesion was assessed. Tiron treatment did not inhibit homotypic adhesion induced by A1 (Figure 6-39), suggesting ROS production occurs down-stream of homotypic adhesion.

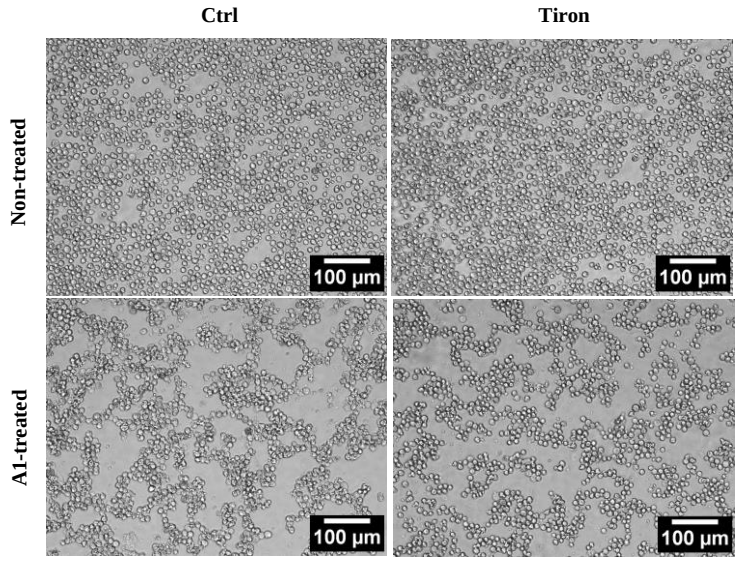

Figure 6-39: ROS depletion by Tiron did not prevent A1-induced homotypic adhesion.
Before A1 treatment, 2 x 10^5 cells (100 µl) were treated with PBS- or Tiron (50 mM) for 1 hour. Homotypic adhesion was viewed under light microscopy. Representative images (original magnification x10) are shown.

6.6.3 A1-induced ROS production occurs upstream of actin-reorganization

We then assessed how Tiron and actin inhibitors together would affect A1-induced ROS production and hESC death. In the presence of Tiron, actin inhibitors treatment did not show significant inhibition effect on A1 cytotoxicity (Figure 6-40).

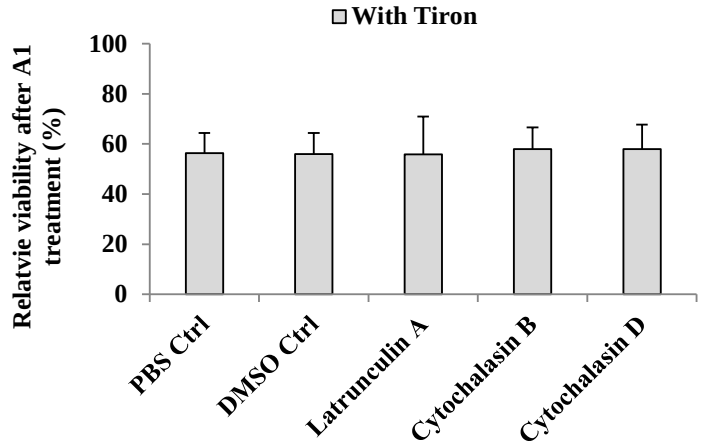

Figure 6-40: Actin inhibitors treatment did not prevent A1 cytotoxicity on hESC in addition to Tiron treatment.
Human ESC (2 x 10^5 in 100 µl) were pre-incubated with PBS- or Tiron (50 mM) for 1 hour and subsequently the three actin inhibitors: Latrunculin A (4 µg), cytochalasin B (4 µg), or cytochalasin D (4 µg) for 5 minutes before A1 treatment. Cell viability was assessed with PI uptake. Data are represented as mean ± SEM.

More importantly, regardless of Tiron, treatment with actin inhibitor did not change the amount of ROS production induced by A1 (Figure 6-41), indicating ROS production occurs upstream of actin re-organization.

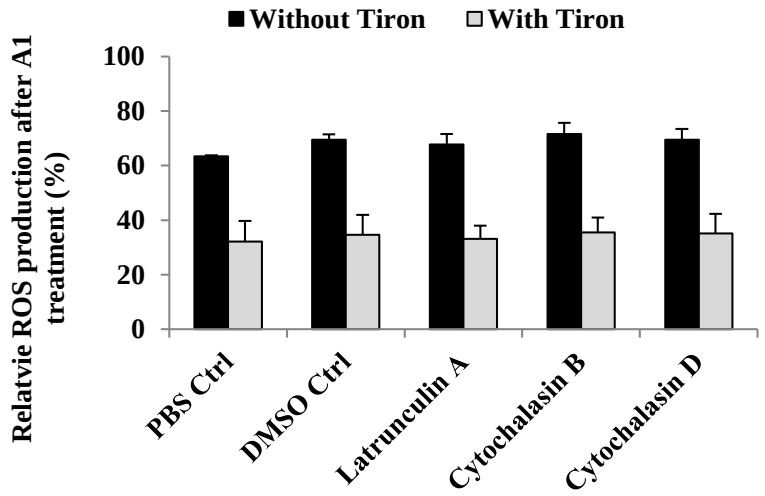

Figure 6-41: Treatment with actin inhibitors did not affect A1-induced ROS production. Human ESC (2 x 10^5 in 100 µl) were pre-incubated with PBS- or Tiron (50 mM) for 1 hour and subsequently the three actin inhibitors: Latrunculin A (4 µg), cytochalasin B (4 µg), or cytochalasin D (4 µg) for 5 minutes before A1 treatment. ROS production was estimated with HE staining by flow cytometry analysis. Data are represented as mean ± SEM.

6.7 Summary

In this chapter, we elucidated the mechanism of A1-induced hESC death. Firstly, in the absence of four apoptosis hallmarks, namely slow killing rate, significant DNA fragmentation and elevated activity of caspases and the formation of apoptotic bodies, A1-induced hESC death was unlikely the result of apoptosis. On the contrary, rapid killing rate, and morphological changes such as cell and mitochondria swelling, plasma membrane damage, all pointed to oncosis as the cause of hESC killing by A1.

A1-induced oncosis was initiated by the binding of A1 on hESC surface. There was no correlation between A1 distribution and plasma membrane pore formation, whilst the A1 aggregates were shown to localize predominantly on fused debris of microvilli and damaged plasma membrane, indicating pore

formation is not caused by external mechanical forces exerted by A1 binding, but more likely to be a result of A1-initiated signalling pathway. The minimally required bivalency of A1 (Figure 4-30B) might contribute to the signalling pathway by ligating receptors on hESC. Microvilli are likely to be the signal initiating sites since the majority of A1 binding was observed on surface microvilli.

In addition, A1-treated hESC exhibited microvilli degradation and homotypic adhesion. A close association between A1-induced cell death and actin re-organization was also unravelled. More importantly, we demonstrated that excess reactive oxygen species (ROS), more specifically superoxide, was produced upon A1 treatment and it was critical for A1-induced hESC death. The source of A1-induced ROS was nicotinamide adenine dinucleotide phosphate (NADPH) oxidase, most likely Nox2 isoform.

Moreover, A1-induced ROS production occurs downstream of microvilli degradation and homotypic adhesion, but upstream of massive actin re-organization, mitochondria impairment and plasma membrane damage.

Taken together, we proposed a mechanistic model of A1-induced hESC death (Figure 6-42). Briefly, bivalent A1 binds to surface microvilli of hESC and ligates certain antigen receptors to initiate the death signal, which leads to microvilli degradation and hESC homotypic adhesion. NADPH oxidase is subsequently activated to produce excess ROS (O^{2-}). Highly oxidized environment leads to massive actin re-organization, mitochondria membrane permeabilization and plasma membrane damage. Eventually, cells undergo oncosis due to severe cellular damage. To our knowledge, this is the first mechanistic model for antibody-induced oncosis on hPSC.

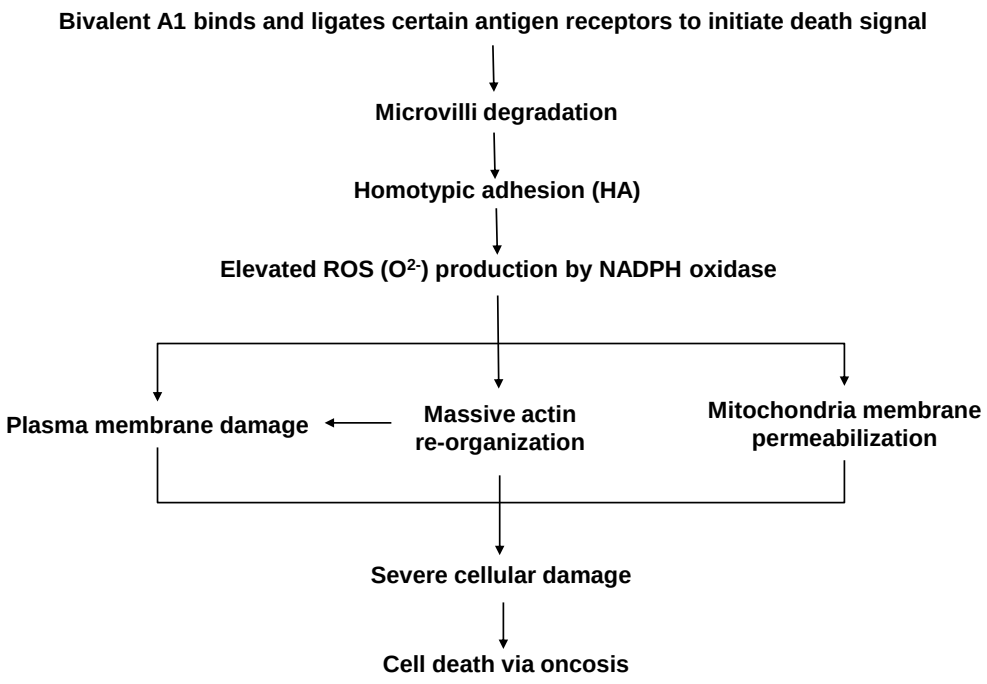

Figure 6-42: Mechanistic model of A1-induced hESC death.
Ligation of antigen receptors upon A1 binding initiates death signalling which firstly resulted in microvilli degradation and homotypic adhesion. Subsequently, excess ROS was produced upon the activation of NADPH oxidase, which leads to plasma membrane damage, actin re-organization, and mitochondrial membrane permeabilization. Eventually, cells undergo oncosis due to severe cellular damage.

7 CHAPTER 7 CONCLUSION, DISCUSSION AND FUTURE WORKS

7.1 Conclusion

A panel of monoclonal antibodies (mAbs) was raised against hESC to identify novel cell surface markers for characterization, enrichment or isolation of undifferentiated hESC from differentiated cells. Interestingly, apart from binding, one of our mAbs, mAb84 was also reported to exert a direct cytotoxic effect on undifferentiated hESC which can be exploited to eliminate residual teratoma-forming hESC after differentiation[34]. Leveraging on this initial finding, our group in BTI continued to generate new mAbs and another mAb exhibiting this hESC killing property is mAb TAG-A1 (A1). Thus the objectives of this thesis were to focus on characterizing mAb A1 *in vitro* and *in vivo*, and elucidated the mechanism of A1-induced hPSC death.

In vitro characterization of A1 found that A1 binds to and kills both hESC and hiPSC. A1 cytotoxicity is specific to undifferentiated hESC as A1 is unable to kill spontaneously differentiated cells via EB formation or FGF-2 starvation. This corresponds to the down-regulation of the A1 epitope during differentiation. Based on stoichiometry assay, saturated A1 binding (over 3 x 10^7 A1 molecules on a single hESC) is essential for maximum killing. The minimum valency required for cell killing is 2 (either IgG or $F(ab)_2$) and the Fc region of the mAb do not contribute to cell killing. A1 kills hPSC within 1 minute in a dosage-dependent manner, which is comparable to mAb84. Nevertheless, being five times smaller in size than mAb84, A1 showed better penetration efficiency into EB. Therefore, A1 may be a better alternative for the removal of residual undifferentiated hPSC in cell aggregates. Although

both A1 and mAb84 show strong reactivity to hPSC, there is no competitive inhibition between the binding of A1 and mAb84 on hESC. Unlike mAb84 that binds to glycosylated PODXL, A1 recognizes an O-linked glycan epitope expressed on multiple antigens on hESC surface. By inhibition studies, the glycan epitope was determined to contain the sugar motif Fucα1-2Galβ1-3GlcNAcβ1-3Galβ1. This difference in antigen specificity can be explained because there are differences in the amino acid sequence of the 6 CDR (3 each for variable heavy and variable light chain) which is responsible for antigen recognition.

From *in vivo* characterization, it was demonstrated that *in vitro* treatment of undifferentiated hESC with A1 just prior to injection into SCID mice was able to prevent or delay the onset of teratoma formation in SCID mouse models. Extending the study to $F(ab)_2$_A1 and a hESC-binding isotype control, further showed that the prevention of teratoma formation *in vivo* is caused by the mAb directly and is independent of ADCC. The *in vivo* characterization was also extended to evaluate the efficiency of *in vivo* A1 treatment. Here, IgG_1 A1 was directly administered *in vivo* separate from hESC injection. Like before, A1 was able to prevent teratoma formation. Therefore, A1 can potentially be administrated either *in vitro* or *in vivo* to kill undifferentiated hPSC and prevent *in vivo* teratoma formation in hPSC-based therapy.

Functional studies were carried out to elucidate the mechanism of A1-induced hPSC death. In the absence of the four hallmarks of apoptosis, including slow killing rate, formation of apoptotic bodies, DNA fragmentation and elevated activity of caspases, it was concluded that A1 was not killing hPSC via

apoptosis. Instead, A1 was killing hPSC via oncosis with hallmarks that include rapid cell death, cell swelling and plasma membrane damage.

A1-induced oncosis was initiated by bivalent A1 binding to and ligating antigen receptors on hPSC surface. Ligation of antigen receptors does not directly form pores throughout the plasma membrane since there was no correlation between A1 distribution and plasma membrane pore formation, whilst A1 aggregates were found to localize predominantly on fused debris of microvilli and damaged plasma membrane. Hence, receptor dimerization was more likely initiating a signalling pathway leading to cell death where microvilli are likely the signal initiating sites since A1 binding was predominantly observed on surface microvilli.

Upon activation of death signalling, A1-treated hESC undergo microvilli degradation and homotypic adhesion at the early stage, followed by excess ROS production, which is upstream of massive actin re-organization, mitochondrial membrane permeabilization, and severe plasma membrane damage. The elevated ROS production is essential for A1-induced hESC death, which is produced by NADPH oxidase, most likely Nox2 isoform.

Taken together, A1 can be utilized *in vitro* to eliminate undifferentiated hPSC from differentiated cell products prior to transplantation, or as a subsequent *in vivo* enhancement, to prevent teratoma formation *in vivo*. We believe that development of stringent removal procedures with A1 alone or in combination with other marker-specific antibodies will greatly improve the safety of hPSC-based therapeutics. Moreover, the first mechanistic model for antibody-induced hESC oncosis is proposed, which also uncovers the essential role of NADPH oxidase-mediated ROS production in A1-induced hESC oncosis.

Understanding of A1-induced hESC death pathway will also be helpful in optimizing the efficacy of antibody-based elimination of undifferentiated hPSC.

7.2 Discussion and future works

Despite the increasing success of differentiating hPSC into various lineage-specific cells and increased clinical trials for the transplantation of hPSC-derived progenies, the safety concerns of teratoma formation by residual undifferentiated hPSC remains to be solved. Prospective approaches, including cell sorting with marker-specific antibodies and recently emerged cytotoxic agents, are superior to retrospective approaches, as the latter would introduce unknown risks by genetic modification and metastatic transformation.

Following the discovery of cytotoxic mAb84 by our group[32], Ben-David et al.[62] identified the small molecule, PluriSIn#1, which can selectively kill hPSC by inhibiting oleic acid biosynthesis from stearoyl-coA desaturase (SCD1). However, based on its mechanism of action, cytotoxicity of PluriSIn#1 may not be restricted to hPSC. Although *in vitro* treatment with PluriSIn#1 prevented teratoma formation in SCID mouse models, prolonged exposure to PluriSIn#1 (~48 hours) may compromise the viability of differentiated cells. Moreover, the effectiveness of *in vivo* treatment with PluriSIn#1 was not investigated.

A1 holds three advantages over PluriSIn#1 in hPSC-based therapy including: specific targeting of hPSC, rapid killing rate, and efficiency in preventing or delaying tumour formation after *in vivo* treatment. A1 is also advantageous over mAb84 for any hPSC-derived transplants in the form of cell layers or cell aggregates. Moreover, to provide the highest level of safety, A1 can be used

in combination with other marker-specific antibodies *in vitro*, or as a subsequent dose *in vivo*. Nevertheless, further optimization is still needed for both *in vitro* treatment and *in vivo* treatment since a complete elimination of teratoma formation was not observed in all the A1 treated SCID mice. For *in vitro* A1 treatment, instead of instantaneous injection after mixing, a longer mixing and/or incubation time (around 5 minutes) may increase the efficiency. Titration of the antibody dosage may also improve hESC killing. For *in vivo* A1 treatment, IgG_1 A1 should be preferred over $F(ab)_2$_A1 to provide a longer half-life post-injection and higher local concentration around hESC-containing tissue. To improve efficiency, one or more subsequent doses can be injected since A1 has no side effects on differentiated cells. Moreover, a combination of *in vitro* and *in vivo* treatment can also be adopted.

For the future work, we are aiming to evaluate the efficiency of A1 in preventing teratoma formation in 3 different SCID mouse models. First, since the ultimate goal is to eliminate undifferentiated hESC from differentiated cell products, a differentiated model, which contains a heterogeneous population of both differentiated and undifferentiated hESC, would be investigated. Differentiation of hESC could either be spontaneous or directed. *In vivo* A1 treatment via intramuscular route would be adopted as it has been demonstrated to work on the undifferentiated model. Second, as not all the undifferentiated hESC can be targeted locally by intramuscular route, we would also evaluate the efficiency of delivering A1 via the intravenous (IV) route, which is the most commonly adopted route of administration for antibody drugs in the market. Comparing to local treatment via IM, a significantly larger amount of mAbs is required by IV to achieve similar local

concentration upon systemic circulation and diffusion[136]. Moreover, as mAb distribution from systemic circulation to the site of cell injection depends on the vascularization of the localised area, the timing of antibody administration and injection of undifferentiated hESC should be optimized. Third, in addition to hESC, *in vivo* characterization of A1 can be extended to hiPSC to demonstrate equivalence in A1 efficacy since the *in vitro* killing data was comparable for both sources of hPSC. The outcome will greatly benefit the field of regenerative medicine because hiPSC is not only an alternate source of hPSC, it has a wider applicability catering to patient-specific hiPSC-based therapy.

So far, most of our findings on A1-induced hESC death are consistent with previous work carried out on type II anti-CD20 antibody, GA101-induced lymphoma cell death[74–76] (Table 7-1). However, different from A1-induced hESC death, GA101 kills lymphoma cell at a slower rate (~4 hours). Moreover, actin re-organization in GA101-induced cell death occurs upstream of homotypic adhesion and ROS production.

Table 7-1: Similarities and differences between GA101 and A1.

Characteristic	GA101	A1
Target cells	B-lymphoma cells	hESC and hiPSC
Bivalency-dependent	--	Fab_A1 loss killing on hESC
Fc-independent	$F(ab)_2$_GA101 kills lymphoma cells	$F(ab)_2$_A1 kills hESC
Not apoptosis	No DNA fragmentation; Low caspases activity ; Bcl-2 overexpression does not affect killing.	No DNA fragmentation; Low caspases activity.
Antigen(s)	CD20	O-linked glycan epitope on multiple proteins
Killing kinetics	**Within 4 hours**	**Within 5 minutes**
Increased membrane permeability	PI, 7-AAD, Annexin V, FITC	PI, 7-AAD, Sytox green
Microvilli degradation	--	Observed under SEM
Homotypic adhesion	Observed under light microscopy	Observed under light microscopy
Actin re-organization	F-actin redistribution; Inhibitors of actin polymerization partially blocks GA101 killing. **Upstream of ROS production**	Actin-associated proteins reduction; F-actin and G-actin redistribution; Inhibitors of actin polymerization partially blocks A1 killing. **Downstream of ROS production**
Plasma membrane damage	Observed under SEM	Measured by dextran beads; Observed under SEM and TEM.
Mitochondrial impairment	Measure with JC-1 dye and $DiOC_6$	Measure with JC-1 dye
Excess ROS production by NADPH oxidase	Excess superoxide production from NADPH oxidase	Excess superoxide production from NADPH oxidase

The differences in killing rate and order of actin re-organization might be explained by the difference in microvilli characteristics between hESC and lymphoma cells. Lymphoma cells have a median microvillar length and surface density ranging from 0.3 to 0.4 μm and 2 to 4 microvilli/ μm^2[2,179]. However, based on our SEM images, microvilli on hESC are generally 2 times longer and denser than lymphoma cells. Microvilli have been reported to initiate signalling pathways through surface receptors such as receptor-tyrosine kinase[180] or G-protein coupled receptors[181]. In A1-induced hESC death, binding of the antibody was predominantly observed on surface microvilli, suggesting that A1-induced death signalling might be initiated through microvilli. Similarly, GA101 might induce death signalling through microvilli on lymphoma cells.

In fact, latrunculin treatment on lymphoma cells was found to result in shortening or even disappearance of microvilli[179]. Therefore, in GA101 studies, prevention of homotypic adhesion, ROS production and eventual lymphoma cell death by latrunculin B treatment could possibly be due to the lack of microvilli to initiate death-signalling pathway. However, in the case of A1, with longer and denser microvilli on hESC, actin inhibitors within a non-toxic range may not be able to affect signalling through shortening hESC microvilli. Therefore, future work could be carried out to investigate how to control hESC microvilli structure and hence control A1-induced cell death.

This hypothesis about signalling through microvilli might also explain the difference in the time required for antibody-induced cell death (GA101-induced lymphoma cell death: 4 hours vs A1-induced hPSC death: 5 minutes)

since theoretically longer and denser microvilli would provide more receptors and therefore faster signal amplification.

Moreover, microvilli are abundant in cellular adhesion proteins. Microvilli structure was also shown to be associated with homotypic adhesion of lymphoma cells[182]. Therefore, A1-induced re-structuring of microvilli is likely to be the cause for the subsequent homotypic adhesion.

Unlike antibody-dependent cell-mediated cytotoxicity (ADCC), complement-dependent cytotoxicity (CDC), and antibody-induced apoptosis, antibody-induced oncosis is a relatively new paradigm. There is still no clear understanding on the mechanism of action for different antibodies to induce oncosis on different cell types. Therefore, understanding the mechanism of A1-induced hESC oncosis would be insightful for the understanding of antibody-induced oncosis in general.

Based on the current findings, we have proposed a model to elucidate the mechanism of A1-induced hESC death. This model revealed a previously unrecognized role for NADPH oxidase-derived ROS in mediating oncotic hESC death. Together with previously reported role of NADPH oxidase-derived ROS in GA101-induced lymphoma death, it might suggest that NADPH oxidase-derived ROS plays a central role in mediating antibody-induced oncosis in various types of cells. Therefore, combination of A1 with ROS–generating reagents could be explored to provide synergistic cell killing. Further investigation of this cell death pathway might be helpful in optimizing the efficacy of antibody-based elimination of undifferentiated hESC.

The molecular basis underlying the activation of Nox2-NADPH oxidase upon A1 binding to hESC remains to be elucidated. Studies have shown that

NADPH oxidase can be activated via different signalling pathways by various stimuli, such as growth factors, cytokines, physical stimuli and lipids[183–185]. However, all pathways eventually converge at a common passage with the phosphorylation of p47phox and the activation of Rac. Therefore, we could start the investigation retrospectively by finding out the responsible kinase and guanine nucleotide exchange factors (GEFs) in A1-induced Nox2 activation. This common passage might also explain why different antibodies targeting different cell types can induce ROS production and eventually lead to oncosis. Alternatively, we could start the investigation from A1 binding. Based on three well-studied pathways of Nox2-NADPH oxidase activation, G-protein coupled receptor (GPCR) or receptor tyrosine kinase (RTK) are responsible for the signalling transduction across the plasma membrane[172] (Figure 7-1).

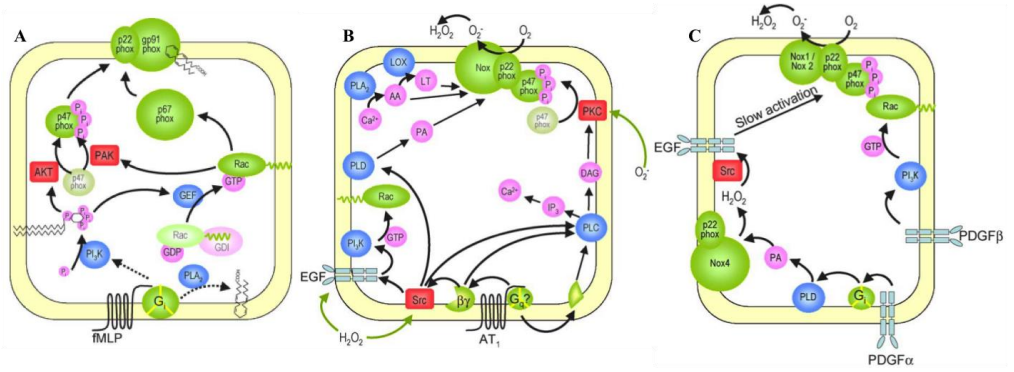

Figure 7-1: Three well-studied pathways of Nox2-NADPH oxidase activation.

Activation of GPCR or RTK requires ligand binding mediated conformational change or dimerization. Although we have demonstrated that membrane pore is not directly formed by antigen oligomerization, bivalency-dependent cytotoxicity of A1 might be associated with antigen conformational change or dimerization. In the support of this hypothesis, bivalent antibody-induced activation of GPCR[186] and RTK have been reported[187]. A previous study has

reported that neutralization of Herpes simplex virus (HSV) is dependent on bivalent antibody crosslinking antigen trimmers on the virus[126]. Moreover, based on our previous study on engineered mAb84 fragments, antibody cytotoxicity appears to depend not only on bivalency, but also on the specific interaction between mAb and target, since bivalent scFv84-HTH was able to recapitulate the cytotoxicity of mAb84 on hESC whereas scFv84-diabody was not cytotoxic[33]. The specificity of antibody-antigen interaction was also observed in anti-CD20 antibodies as demonstrated that even with overlapping epitope, type I and II anti-CD20 mAbs evoke different modes of lymphoma cell death[188]. The same study suggested that the specificity is caused by differences in the orientation of antibody-antigen binding and the resultant membrane compartmentalization of antigen dimers. Therefore, it is imperative to identify the complete epitope that A1 recognizes so as to further understand how the signalling cascade is triggered. Since A1 recognizes glycans on multiple proteins, we also need to delineate whether one or multiple types of receptors trigger the signalling cascade.

NADPH oxidases are membrane-bound and can be found at different subcellular locations. The 2 major sites of Nox2-NADPH oxidases are plasma membrane[189,190] and lysosomal/endosomal membrane[191–193]. Since targeting to specific subcellular site is required for localised ROS production, knowing the site of A1-induced ROS production could provide us an insight to understand the activation pathway of NADPH oxidase as well. Plasma membrane-bound NADPH oxidases orientate in the way that the electron transfers from cytoplasmic NADPH to oxygen on the extracellular side of the plasma membrane (Figure 6-25). Superoxide generated in the extracellular domain

requires time to diffuse into intracellular space and would also be instantly diluted with a much larger assay volume, therefore unlikely can induce a rapid and drastic killing. Moreover, superoxide released into the extracellular domain would result in a homogeneously oxidized environment for all cells in the assay, which contradicts to the direct correlation between cell death and ROS production. To achieve direct and rapid cell killing, superoxide is more likely produced in an intracellular compartment, such as lysosomal membrane or endosomal membrane. Since lysosomal/endosomal membrane is formed from phagocytosis/endocytosis of plasma membrane (Figure 7-2), NADPH oxidase orients in the opposite way so that superoxide is produced into the lumen of lysosome and endosome.

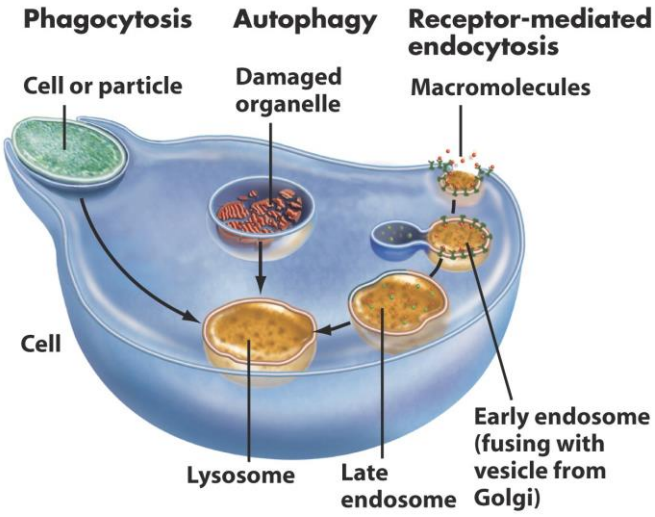

Figure 7-2: Role of phagocytosis and endocytosis in formation of endosomal and lysosomal membrane[194].

Lysosomal-produced ROS has been implicated in different cell death pathways, including apoptosis, oncosis and autophagic cell death[195,196]. Studies have also reported the link between superoxide production and lysosome membrane permeabilization (LMP), though it appears that superoxide can be both cause and consequence of LMP[195,197]. Therefore,

whether there is LMP in A1-treated hESC and how is LMP linked to A1-induced ROS production warrants further investigation.

8 BIBLIOGRAPHY

1. Thomson, J. A. *et al.* Embryonic Stem Cell Lines Derived from Human Blastocysts. *Science* **282,** 1145–1147 (1998).
2. Takahashi, K. *et al.* Induction of pluripotent stem cells from adult human fibroblasts by defined factors. *Cell* **131,** 861–872 (2007).
3. Joseph, I. E. *et al.* Differentiation of human embryonic stem cells into embryoid bodies compromising the three embryonic germ layers. *Mol Med* **6,** 88–95 (2000).
4. Beqqali, A., van Eldik, W., Mummery, C. & Passier, R. Human stem cells as a model for cardiac differentiation and disease. *Cell Mol Life Sci* **66,** 800–13 (2009).
5. Dai, W. *et al.* Survival and maturation of human embryonic stem cell-derived cardiomyocytes in rat hearts. *J Mol Cell Cardiol* **43,** 504–16 (2007).
6. Chong, J. J. H. *et al.* Human embryonic-stem-cell-derived cardiomyocytes regenerate non-human primate hearts. *Nature* **510,** 273–277 (2014).
7. Duan, Y. *et al.* Differentiation and enrichment of hepatocyte-like cells from human embryonic stem cells in vitro and in vivo. *Stem Cells* **25,** 3058–68 (2007).
8. Ng, S. *et al.* Human iPSC-Derived Hepatocyte-like Cells Support Plasmodium Liver-Stage Infection In Vitro. *Stem Cell Rep.* **4,** 348–359 (2015).
9. Takayama, K. *et al.* Efficient Generation of Functional Hepatocytes From Human Embryonic Stem Cells and Induced Pluripotent Stem Cells by HNF4α Transduction. *Mol. Ther.* **20,** 127–137 (2012).

10. Grealish, S. *et al.* Human ESC-Derived Dopamine Neurons Show Similar Preclinical Efficacy and Potency to Fetal Neurons when Grafted in a Rat Model of Parkinson's Disease. *Cell Stem Cell* **15,** 653–665 (2014).
11. Hallett, P. J. *et al.* Successful Function of Autologous iPSC-Derived Dopamine Neurons following Transplantation in a Non-Human Primate Model of Parkinson's Disease. *Cell Stem Cell* **16,** 269–274 (2015).
12. Hu, B. Y. & S.C., Z. Directed differentiation of neural-stem cells and subtype-specific neurons from hESCs. *Methods Mol Biol* **636,** 123–37 (2010).
13. Takasato, M. *et al.* Directing human embryonic stem cell differentiation towards a renal lineage generates a self-organizing kidney. *Nat. Cell Biol.* **16,** 118–126 (2014).
14. Bai, H. & Wang, Z. Z. Directing human embryonic stem cells to generate vascular progenitor cells. *Gene Ther* **15,** 89–95 (2008).
15. Ferreira, L. S. *et al.* Vascular progenitor cells isolated from human embryonic stem cells give rise to endothelial and smooth muscle like cells and form vascular networks in vivo. *Circ Res* **101,** 286–94 (2007).
16. Jezierski, A., Swedani, A. & Wang, L. Development of hematopoietic and endothelial cells from human embryonic stem cells: lessons from the studies using mouse as a model. *ScientificWorldJournal* **7,** 1950–64 (2007).
17. Levenberg, S., Zoldan, J., Basevitch, Y. & Langer, R. Endothelial potential of human embryonic stem cells. *Blood* **110,** 806–14 (2007).

18. Li, Z., Han, Z. & Wu, J. C. Transplantation of human embryonic stem cell-derived endothelial cells for vascular diseases. *J Cell Biochem* **106,** 194–9 (2009).
19. Xiong, Q. *et al.* A fibrin patch-based enhanced delivery of human embryonic stem cell-derived vascular cell transplantation in a porcine model of postinfarction left ventricular remodeling. *Stem Cells* **29,** 367–75 (2011).
20. Bielby, R. C., Boccaccini, A. R., Polak, J. M. & Buttery, L. D. In vitro differentiation and in vivo mineralization of osteogenic cells derived from human embryonic stem cells. *Tissue Eng* **10,** 9–10 (2004).
21. Sottile, V., Thomson, A. & McWhir, J. In vitro osteogenic differentiation of human ES cells. *CLONING STEM CELLS* **5,** 2 (2003).
22. Green, H., Easley, K. & Iuchi, S. Marker succession during the development of keratinocytes from cultured human embryonic stem cells. *Proc Natl Acad Sci U A* **100,** 15625–30 (2003).
23. Idelson, M. *et al.* Directed differentiation of human embryonic stem cells into functional retinal pigment epithelium cells. *Cell Stem Cell* **5,** 396–408 (2009).
24. Lu, B. *et al.* Long-term safety and function of RPE from human embryonic stem cells in preclinical models of macular degeneration. *Stem Cells* **27,** 2126–35 (2009).
25. FDA approves human embryonic stem cell study. at <http://edition.cnn.com/2009/HEALTH/01/23/stem.cell/>
26. Vergano, D. Second human embryonic stem cell clinical trial to start. (2010). at

<http://content.usatoday.com/communities/sciencefair/post/2010/11/second-human-embryonic-stem-cell-clinical-trial-to-start/1#.VUCVDSGqpBc>

27. ACT announces clinical trials for myopia. at <http://www.stemcellsfreak.com/2013/02/ACT-stem-cell-trial-myopia.html>
28. Embryonic Stem Cells in Trial for Diabetes. at <http://www.biosciencetechnology.com/articles/2014/10/embryonic-stem-cells-trial-diabetes>
29. Blum, B. & Benvenisty, N. The Tumorigenicity of Human Embryonic Stem Cells. *Adv Cancer Res* **100,** 133–158 (2008).
30. Ben-David, U. & Benvenisty, N. The tumorigenicity of human embryonic and induced pluripotent stem cells. *Nat Rev Cancer* **11,** 268–77 (2011).
31. Hentze, H., Graichen, R. & Colman, A. Cell therapy and the safety of embryonic stem cell-derived grafts. *Trends Biotechnol* **25,** 24–32 (2007).
32. Choo, A. B. *et al.* Selection against undifferentiated human embryonic stem cells by a cytotoxic antibody recognizing podocalyxin-like protein-1. *Stem Cells Dayt. Ohio* **26,** 1454–1463 (2008).
33. Lim, D. Y. X. *et al.* Cytotoxic antibody fragments for eliminating undifferentiated human embryonic stem cells. *J. Biotechnol.* **153,** 77–85 (2011).
34. Tan, H. L., Fong, W. J., Lee, E. H., Yap, M. & Choo, A. mAb 84, a cytotoxic antibody that kills undifferentiated human embryonic stem cells via oncosis. *Stem Cells Dayt. Ohio* **27,** 1792–1801 (2009).

35. Hyslop, L., Armstrong, L., Stojkovic, M. & Lako, M. Derivation of a human embryonic stem cell line, and differentiation strategies. *Mol. Med.* **7,** (2005).
36. Takahashi, K. & Yamanaka, S. Induction of Pluripotent Stem Cells from Mouse Embryonic and Adult Fibroblast Cultures by Defined Factors. *Cell* **126,** 663–676 (2006).
37. Nsair, A. & MacLellan, W. R. Induced pluripotent stem cells for regenerative cardiovascular therapies and biomedical discovery. *Adv. Drug Deliv. Rev.* **63,** 324–330 (2011).
38. Drukker, M. & Benvenisty, N. The immunogenicity of human embryonic stem-derived cells. *Trends Biotechnol* **22,** 136–41 (2004).
39. Baldwin, T. Morality and human embryo research. Introduction to the Talking Point on morality and human embryo research. *EMBO Rep.* **10,** 299–300 (2009).
40. Davila, J. C. *et al.* Use and Application of Stem Cells in Toxicology. *Toxicol. Sci.* **79,** 214–223 (2004).
41. *Asterias Biotherapeutics Announces First Patient Treated in Phase 1/2a Dose-Escalation Clinical Trial of AST-OPC1 for Complete Cervical Spinal Cord Injury*. at <http://asteriasbiotherapeutics.com/asterias-biotherapeutics-announces-first-patient-treated-in-phase-12a-dose-escalation-clinical-trial-of-ast-opc1-for-complete-cervical-spinal-cord-injury/>
42. Priest, C. A., Manley, N. C., Denham, J., Wirth, E. D. & Lebkowski, J. S. Preclinical safety of human embryonic stem cell-derived oligodendrocyte

progenitors supporting clinical trials in spinal cord injury. *Regen. Med.* (2015). doi:10.2217/rme.15.57

43. Schwartz, S. D. *et al.* Embryonic stem cell trials for macular degeneration: a preliminary report. *The Lancet* **379,** 713–720 (2012).
44. Zhang, W. Teratoma formation: A tool for monitoring pluripotency in stem cell research. *StemBook* (2014). doi:10.3824/stembook.1.53.1
45. Hentze, H. *et al.* Teratoma formation by human embryonic stem cells: evaluation of essential parameters for future safety studies. *Stem Cell Res* **2,** 198–210 (2009).
46. Arnhold, S., Klein, H., Semkova, I., Addicks, K. & Schraermeyer, U. Neurally selected embryonic stem cells induce tumor formation after long-term survival following engraftment into the subretinal space. *Invest Ophthalmol Vis Sci* **45,** 4251–5 (2004).
47. Fujikawa, T. *et al.* Teratoma Formation Leads to Failure of Treatment for Type I Diabetes Using Embryonic Stem Cell-Derived Insulin-Producing Cells. *Am. J. Pathol.* **166,** 1781–1791 (2005).
48. Prokhorova, T. A. *et al.* Teratoma formation by human embryonic stem cells is site dependent and enhanced by the presence of Matrigel. *Stem Cells Dev.* **18,** 47–54 (2009).
49. Shih, C. C., Forman, S. J., Chu, P. & Slovak, M. Human embryonic stem cells are prone to generate primitive, undifferentiated tumors in engrafted human fetal tissues in severe combined immunodeficient mice. *Stem Cells Dev* **16,** 893–902 (2007).

50. Werbowetski-Ogilvie, T. E. *et al.* Characterization of human embryonic stem cells with features of neoplastic progression. *Nat Biotechnol* **27,** 91–7 (2009).

51. Yang, S. *et al.* Tumor progression of culture-adapted human embryonic stem cells during long-term culture. *Genes. Chromosomes Cancer* **47,** 665–79 (2008).

52. Griscelli, F. *et al.* Malignant germ cell-like tumors, expressing Ki-1 antigen (CD30), are revealed during in vivo differentiation of partially reprogrammed human-induced pluripotent stem cells. *Am. J. Pathol.* **180,** 2084–2096 (2012).

53. Rao, M. Tumorigenesis and embryonic stem cell-derived therapy. *Stem Cells Dev* **16,** 903–4 (2007).

54. Tang, C. *et al.* An antibody against SSEA-5 glycan on human pluripotent stem cells enables removal of teratoma-forming cells. *Nat Biotechnol* **29,** 829–34 (2011).

55. Chung, S. *et al.* Genetic selection of sox1GFP-expressing neural precursors removes residual tumorigenic pluripotent stem cells and attenuates tumor formation after transplantation. *J Neurochem* **97,** 1467–80 (2006).

56. Fong, C. Y., Peh, G. S., Gauthaman, K. & Bongso, A. Separation of SSEA-4 and TRA-1-60 labelled undifferentiated human embryonic stem cells from a heterogeneous cell population using magnetic-activated cell sorting (MACS) and fluorescence-activated cell sorting (FACS). *Stem Cell Rev* **5,** 72–80 (2009).

57. Xu, C., Police, S., Rao, N. & Carpenter, M. K. Characterization and enrichment of cardiomyocytes derived from human embryonic stem cells. *Circ. Res.* **91,** 501–508 (2002).

58. Blum, B., Bar-Nur, O., Golan-Lev, T. & Benvenisty, N. The anti-apoptotic gene survivin contributes to teratoma formation by human embryonic stem cells. *Nat. Biotechnol.* **27,** 281–287 (2009).

59. Jung, J. *et al.* Ablation of tumor-derived stem cells transplanted to the central nervous system by genetic modification of embryonic stem cells with a suicide gene. *Hum Gene Ther* **18,** 1182–92 (2007).

60. Schuldiner, M., Itskovitz-Eldor, J. & Benvenisty, N. Selective ablation of human embryonic stem cells expressing a 'suicide' gene. *Stem Cells Dayt. Ohio* **21,** 257–265 (2003).

61. Tang, C., Weissman, I. L. & Drukker, M. The safety of embryonic stem cell therapy relies on teratoma removal. *Oncotarget* **3,** 7–8 (2012).

62. Ben-David, U. *et al.* Selective elimination of human pluripotent stem cells by an oleate synthesis inhibitor discovered in a high-throughput screen. *Cell Stem Cell* **12,** 167–79 (2013).

63. Lee, M.-O. *et al.* Inhibition of pluripotent stem cell-derived teratoma formation by small molecules. *Proc. Natl. Acad. Sci. U. S. A.* **110,** E3281–3290 (2013).

64. Parsons, X. H. *et al.* Efficient derivation of human neuronal progenitors and neurons from pluripotent human embryonic stem cells with small molecule induction. *J Vis Exp* e3273 (2011).

65. Gerrard, L., Zhao, D., Clark, A. J. & Cui, W. Stably transfected human embryonic stem cell clones express OCT4-specific green fluorescent

protein and maintain self-renewal and pluripotency. *Stem Cells* **23,** 124–33 (2005).

66. Kumashiro, Y. *et al.* Enrichment of Hepatocytes Differentiated from Mouse Embryonic Stem Cells as a Transplantable Source. *Transplantation* **79,** 550–557 (2005).
67. Bieberich, E., Silva, J., Wang, G., Krishnamurthy, K. & Condie, B. G. Selective apoptosis of pluripotent mouse and human stem cells by novel ceramide analogues prevents teratoma formation and enriches for neural precursors in ES cell-derived neural transplants. *J Cell Biol* **167,** 723–34 (2004).
68. Cao, F. *et al.* In vivo visualization of embryonic stem cell survival, proliferation, and migration after cardiac delivery. *Circulation* **113,** 1005–14 (2006).
69. Rong, Z., Fu, X., Wang, M. & Xu, Y. A scalable approach to prevent teratoma formation of human embryonic stem cells. *J Biol Chem* **287,** 32338–45 (2012).
70. Bazil, V., Brandt, J., Tsukamoto, A. & Hoffman, R. Apoptosis of human hematopoietic progenitor cells induced by crosslinking of surface CD43. *Blood 1995 Jul 15862502-11* **86,** 502–11 (1995).
71. Matsuoka, S. *et al.* a novel type of cell death of lymphocytes induced by a monoclonal antibody without participation of complement. *J Exp Med* **181,** 2007–2015 (1995).
72. Zhang, C., Xu, Y., Gu, J. & Schlossman, S. F. A cell surface receptor defined by a mAb mediates a unique type of cell death similar to oncosis. *Proc. Natl. Acad. Sci. U. S. A.* **95,** 6290–6295 (1998).

73. Zhang, N., Khawli, L. A., Hu, P. & Epstein, A. L. Generation of rituximab polymer may cause hyper-cross-linking-induced apoptosis in non-Hodgkin's lymphomas. *Clin Cancer Res* **11,** 5971–80 (2005).

74. Ivanov, A. *et al.* Monoclonal antibodies directed to CD20 and HLA-DR can elicit homotypic adhesion followed by lysosome-mediated cell death in human lymphoma and leukemia cells. *J. Clin. Invest.* **119,** 2143–2159 (2009).

75. Alduaij, W. *et al.* Novel type II anti-CD20 monoclonal antibody (GA101) evokes homotypic adhesion and actin-dependent, lysosome-mediated cell death in B-cell malignancies. *Blood* **117,** 4519–4529 (2011).

76. Honeychurch, J. *et al.* Antibody-induced nonapoptotic cell death in human lymphoma and leukemia cells is mediated through a novel reactive oxygen species-dependent pathway. *Blood* **119,** 3523–3533 (2012).

77. Loo, D. *et al.* The glycotope-specific RAV12 monoclonal antibody induces oncosis in vitro and has antitumor activity against gastrointestinal adenocarcinoma tumor xenografts in vivo. *Mol Cancer Ther* **6,** 856–65 (2007).

78. Hernandez, A. M. *et al.* Anti-NeuGcGM3 antibodies, actively elicited by idiotypic vaccination in nonsmall cell lung cancer patients, induce tumor cell death by an oncosis-like mechanism. *J Immunol* **186,** 3735–44 (2011).

79. Roque-Navarro, L. *et al.* Anti-ganglioside antibody-induced tumor cell death by loss of membrane integrity. *Mol. Cancer Ther.* **7,** 2033–2041 (2008).

80. Trump, B. F., Berezesky, I. K., Chang, S. H. & Phelps, P. C. The pathways of cell death: oncosis, apoptosis, and necrosis. *Toxicol. Pathol.* **25,** 82–88 (1997).

81. Duprez, L., Wirawan, E., Vanden Berghe, T. & Vandenabeele, P. Major cell death pathways at a glance. *Microbes Infect. Inst. Pasteur* **11,** 1050–1062 (2009).

82. Weerasinghe, P. & Buja, L. M. Oncosis: an important non-apoptotic mode of cell death. *Exp. Mol. Pathol.* **93,** 302–308 (2012).

83. Majno, G. & Joris, I. Apoptosis, oncosis, and necrosis. An overview of cell death. *Am. J. Pathol.* **146,** 3–15 (1995).

84. Kerr, J. F., Wyllie, A. H. & Currie, A. R. Apoptosis- A Basic Biological Phenomenon with Wide-ranging Implications in Tissue Kinetics. *Br J Cancer* **26,** 239–57 (1972).

85. Favaloro, B., Allocati, N., Graziano, V., Di, L. C. & De Laurenzi, V. Role of apoptosis in disease. *Aging* **4,** 330–49 (2012).

86. Takuma, K., Yan, S. S., Stern, D. M. & Yamada, K. Mitochondrial dysfunction, endoplasmic reticulum stress, and apoptosis in Alzheimer's disease. *J Pharmacol Sci* **97,** 312–6 (2005).

87. Van Cruchten, S. & Van Den Broeck, W. Morphological and biochemical aspects of apoptosis, oncosis and necrosis. *Anat. Histol. Embryol.* **31,** 214–223 (2002).

88. Fulda, S. & Debatin, K.-M. Extrinsic versus intrinsic apoptosis pathways in anticancer chemotherapy. *Oncogene* **25,** 4798–4811 (2006).

89. Elmore, S. Apoptosis: a review of programmed cell death. *Toxicol. Pathol.* **35,** 495–516 (2007).

90. Calvino-Fernández, M. & Parra-Cid, T. H. pylori y alteraciones mitocondriales en células epiteliales: Relación con estrés oxidativo. *Rev. Esp. Enfermedades Dig.* **102,** 41–50 (2010).
91. Hockenbery, D. Defining Apoptosis. *Am J Pathol* **146,** 16–9 (1995).
92. Weerasinghe, P., Hallock, S., Brown, R. E., Loose, D. S. & Buja, L. M. A model for cardiomyocyte cell death: Insights into mechanisms of oncosis. *Exp Mol Pathol* **94,** 289–300 (2013).
93. Buja, L. M. Myocardial ischemia and reperfusion injury. *Cardiovasc. Pathol. Off. J. Soc. Cardiovasc. Pathol.* **14,** 170–175 (2005).
94. Liu, B. *et al.* Induction of apoptosis and activation of the caspase cascade by anti-EGF receptor monoclonal antibodies in DiFi human colon cancer cells do not involve the c-jun N-terminal kinase activity. *Br. J. Cancer* **82,** 1991–1999 (2000).
95. Tortora, G. *et al.* Cooperative inhibitory effect of novel mixed backbone oligonucleotide targeting protein kinase A in combination with docetaxel and anti-epidermal growth factor-receptor antibody on human breast cancer cell growth. *Clin. Cancer Res. Off. J. Am. Assoc. Cancer Res.* **5,** 875–881 (1999).
96. Huang, S. M. & Harari, P. M. Modulation of radiation response after epidermal growth factor receptor blockade in squamous cell carcinomas: inhibition of damage repair, cell cycle kinetics, and tumor angiogenesis. *Clin. Cancer Res. Off. J. Am. Assoc. Cancer Res.* **6,** 2166–2174 (2000).
97. Milella, M. *et al.* Trastuzumab down-regulates Bcl-2 expression and potentiates apoptosis induction by Bcl-2/Bcl-XL bispecific antisense

oligonucleotides in HER-2 gene--amplified breast cancer cells. *Clin. Cancer Res. Off. J. Am. Assoc. Cancer Res.* **10,** 7747–7756 (2004).

98. Pedersen, I. M., Buhl, A. M., Klausen, P., Geisler, C. H. & Jurlander, J. The chimeric anti-CD20 antibody rituximab induces apoptosis in B-cell chronic lymphocytic leukemia cells through a p38 mitogen activated protein-kinase-dependent mechanism. *Blood* **99,** 1314–1319 (2002).
99. Ludwig, D. L., Pereira, D. S., Zhu, Z., Hicklin, D. J. & Bohlen, P. Monoclonal antibody therapeutics and apoptosis. *Oncogene* **22,** 9097–9106 (2003).
100. Trauth, B. C. *et al.* Monoclonal antibody-mediated tumor regression by induction of apoptosis. *Science* **245,** 301–305 (1989).
101. Ichikawa, K. *et al.* Tumoricidal activity of a novel anti-human DR5 monoclonal antibody without hepatocyte cytotoxicity. *Nat. Med.* **7,** 954–960 (2001).
102. R Safa, A. Roles of c-FLIP in Apoptosis, Necroptosis, and Autophagy. *J. Carcinog. Mutagen.* (2013). doi:10.4172/2157-2518.S6-003
103. Choo, A., Padmanabhan, J., Chin, A., Fong, W. J. & Oh, S. K. W. Immortalized feeders for the scale-up of human embryonic stem cells in feeder and feeder-free conditions. *J. Biotechnol.* **122,** 130–141 (2006).
104. Zhang, J. *et al.* Functional Cardiomyocytes Derived From Human Induced Pluripotent Stem Cells. *Circ. Res.* **104,** e30–e41 (2009).
105. Heins, N. *et al.* Clonal derivation and characterization of human embryonic stem cell lines. *J Biotechnol* **122,** 511–20 (2006).
106. Gramer, M. J., Goochee, C. F., Chock, V. Y., Brousseau, D. T. & Sliwkowski, M. B. Removal of Sialic Acid from a Glycoprotein in CHO

Cell Culture Supernatant by Action of an Extracellular CHO Cell Sialidase. *Nat. Biotechnol.* **13,** 692–698 (1995).

107. Sen, S., Jumaa, H. & Webster, N. J. G. Splicing factor SRSF3 is crucial for hepatocyte differentiation and metabolic function. *Nat. Commun.* **4,** 1336 (2013).

108. Kurosawa, H. Methods for inducing embryoid body formation: in vitro differentiation system of embryonic stem cells. *J. Biosci. Bioeng.* **103,** 389–398 (2007).

109. Klement, E., Lipinszki, Z., Kupihár, Z., Udvardy, A. & Medzihradszky, K. F. Enrichment of O-GlcNAc modified proteins by the periodate oxidation – hydrazide resin capture approach. *J. Proteome Res.* **9,** 2200–2206 (2010).

110. Schwarz, F. & Aebi, M. Mechanisms and principles of N-linked protein glycosylation. *Curr. Opin. Struct. Biol.* **21,** 576–582 (2011).

111. Van den Steen, P., Rudd, P. M., Dwek, R. A. & Opdenakker, G. Concepts and principles of O-linked glycosylation. *Crit. Rev. Biochem. Mol. Biol.* **33,** 151–208 (1998).

112. Varki, A. & Schauer, R. in *Essentials of Glycobiology* (eds. Varki, A. et al.) (Cold Spring Harbor Laboratory Press, 2009). at <http://www.ncbi.nlm.nih.gov/books/NBK1920/>

113. Schauer, R. in *Advances in Carbohydrate Chemistry and Biochemistry* (ed. Horton, R. S. T. and D.) **40,** 131–234 (Academic Press, 1982).

114. Stanley, P., Schachter, H. & Taniguchi, N. in *Essentials of Glycobiology* (eds. Varki, A. et al.) (Cold Spring Harbor Laboratory Press, 2009). at <http://www.ncbi.nlm.nih.gov/books/NBK1917/>

115. Morelle, W. & Michalski, J.-C. Analysis of protein glycosylation by mass spectrometry. *Nat. Protoc.* **2,** 1585–1602 (2007).

116. de Freitas Junior, J. C. M. *et al.* Inhibition of N-linked glycosylation by tunicamycin induces E-cadherin-mediated cell-cell adhesion and inhibits cell proliferation in undifferentiated human colon cancer cells. *Cancer Chemother. Pharmacol.* **68,** 227–238 (2011).

117. Rodgers, A. K., Nair, A., Binkley, P. A., Tekmal, R. & Schenken, R. S. Inhibition of CD44 N- and O-linked Glycosylation Decreases Endometrial Cell Lines Attachment to Peritoneal Mesothelial Cells. *Fertil. Steril.* **95,** 823–825 (2011).

118. Cummings, R. D. & Etzler, M. E. in *Essentials of Glycobiology* (eds. Varki, A. et al.) (Cold Spring Harbor Laboratory Press, 2009).

119. Natunen, S. *et al.* The binding specificity of the marker antibodies Tra-1-60 and Tra-1-81 reveals a novel pluripotency-associated type 1 lactosamine epitope. *Glycobiology* **21,** 1125–1130 (2011).

120. Kannagi, R. *et al.* Stage-specific embryonic antigens (SSEA-3 and -4) are epitopes of a unique globo-series ganglioside isolated from human teratocarcinoma cells. *EMBO J.* **2,** 2355–2361 (1983).

121. Stanley, P. & Cummings, R. D. in *Essentials of Glycobiology* (eds. Varki, A. et al.) (Cold Spring Harbor Laboratory Press, 2009). at <http://www.ncbi.nlm.nih.gov/books/NBK1892/>

122. Merchant, M. *et al.* Monovalent antibody design and mechanism of action of onartuzumab, a MET antagonist with anti-tumor activity as a therapeutic agent. *Proc. Natl. Acad. Sci.* 201302725 (2013). doi:10.1073/pnas.1302725110

123. Maynard, J. & Georgiou, G. Antibody engineering. *Annu. Rev. Biomed. Eng.* **2,** 339–376 (2000).

124. Won, J., Nam, P., Lee, Y. & Choe, M. Higher cytotoxicity of divalent antibody-toxins than monovalent antibody-toxins. *Biochem. Biophys. Res. Commun.* **382,** 15–20 (2009).

125. Koolwijk, P., Van de Winkel, J. G., Otten, I. & Bast, B. J. Human monocyte-mediated cytotoxicity towards erythrocytes induced by hybrid mouse monoclonal antibodies: effect of antibody binding valency on IgG-Fc gamma R interaction. *Immunology* **75,** 336–342 (1992).

126. Krawczyk, A. *et al.* Impact of Valency of a Glycoprotein B-Specific Monoclonal Antibody on Neutralization of Herpes Simplex Virus. *J. Virol.* **85,** 1793–1803 (2011).

127. Lim, D. Y. *et al.* Cytotoxic antibody fragments for eliminating undifferentiated human embryonic stem cells. *J Biotechnol* **153,** 77–85 (2011).

128. Cobbold, S. P. & Waldmann, H. Therapeutic potential of monovalent monoclonal antibodies. *Nature* **308,** 460–462 (1984).

129. Stackpole, C. W., Cremona, P., Leonard, C. & Stremmel, P. Antigenic modulation as a mechanism for tumor escape from immune destruction: identification of modulation-positive and modulation-negative mouse lymphomas with xenoantisera to murine leukemia virus gp70. *J. Immunol.* **125,** 1715–1723 (1980).

130. *Lehninger Principles Of Biochemistry 5th Fifth Edition 2008*. (W.H. Freeman and Company, 2008).

131. Charles A Janeway, J., Travers, P., Walport, M. & Shlomchik, M. J. The structure of a typical antibody molecule. (2001).

132. Coleman, L. & Mahler, S. M. Purification of Fab fragments from a monoclonal antibody papain digest by Gradiflow electrophoresis. *Protein Expr. Purif.* **32,** 246–251 (2003).

133. von Pawel-Rammingen, U., Johansson, B. P. & Björck, L. IdeS, a novel streptococcal cysteine proteinase with unique specificity for immunoglobulin G. *EMBO J.* **21,** 1607–1615 (2002).

134. Keizer, R. J., Huitema, A. D. R., Schellens, J. H. M. & Beijnen, J. H. Clinical Pharmacokinetics of Therapeutic Monoclonal Antibodies. *Clin. Pharmacokinet.* **49,** 493–507 (2012).

135. Tabrizi, M., Bornstein, G. G. & Suria, H. Biodistribution Mechanisms of Therapeutic Monoclonal Antibodies in Health and Disease. *AAPS J.* **12,** 33–43 (2009).

136. Jones, R. G. A. & Martino, A. Targeted localized use of therapeutic antibodies: a review of non-systemic, topical and oral applications. *Crit. Rev. Biotechnol.* 1–15 (2015). doi:10.3109/07388551.2014.992388

137. Yamada, H. & Ando, H. Orientation of apical and basal actin stress fibers in isolated and subconfluent endothelial cells as an early response to cyclic stretching. *Mol. Cell. Biomech. MCB* **4,** 1–12 (2007).

138. Millán, J. *et al.* Adherens junctions connect stress fibres between adjacent endothelial cells. *BMC Biol.* **8,** 11 (2010).

139. Chan, H. T. C. *et al.* CD20-induced Lymphoma Cell Death Is Independent of Both Caspases and Its Redistribution into Triton X-100 Insoluble Membrane Rafts. *Cancer Res.* **63,** 5480–5489 (2003).

140. Kansas, G. S. & Tedder, T. F. Transmembrane signals generated through MHC class II, CD19, CD20, CD39, and CD40 antigens induce LFA-1-dependent and independent adhesion in human B cells through a tyrosine kinase-dependent pathway. *J. Immunol.* **147,** 4094–4102 (1991).

141. Ng, V. Y., Ang, S. N., Chan, J. X. & Choo, A. B. H. Characterization of Epithelial Cell Adhesion Molecule as a Surface Marker on Undifferentiated Human Embryonic Stem Cells. *STEM CELLS* **28,** 29–35 (2010).

142. MacLean-Fletcher, S. & Pollard, T. D. Mechanism of action of cytochalasin B on actin. *Cell* **20,** 329–341 (1980).

143. Yarmola, E. G., Somasundaram, T., Boring, T. A., Spector, I. & Bubb, M. R. Actin-latrunculin A structure and function. Differential modulation of actin-binding protein function by latrunculin A. *J. Biol. Chem.* **275,** 28120–28127 (2000).

144. D'Autréaux, B. & Toledano, M. B. ROS as signalling molecules: mechanisms that generate specificity in ROS homeostasis. *Nat. Rev. Mol. Cell Biol.* **8,** 813–824 (2007).

145. Sauer, H., Wartenberg, M. & Hescheler, J. Reactive oxygen species as intracellular messengers during cell growth and differentiation. *Cell. Physiol. Biochem. Int. J. Exp. Cell. Physiol. Biochem. Pharmacol.* **11,** 173–186 (2001).

146. Clanton, T. L. Hypoxia-induced reactive oxygen species formation in skeletal muscle. *J. Appl. Physiol.* **102,** 2379–2388 (2007).

147. Lee, S. B. *et al.* Serum deprivation-induced reactive oxygen species production is mediated by Romo1. *Apoptosis Int. J. Program. Cell Death* **15,** 204–218 (2010).

148. Circu, M. L. & Aw, T. Y. REACTIVE OXYGEN SPECIES, CELLULAR REDOX SYSTEMS AND APOPTOSIS. *Free Radic. Biol. Med.* **48,** 749–762 (2010).

149. Hu, C.-T. *et al.* Reactive oxygen species-mediated PKC and integrin signaling promotes tumor progression of human hepatoma HepG2. *Clin. Exp. Metastasis* **28,** 851–863 (2011).

150. Cabiscol, E., Piulats, E., Echave, P., Herrero, E. & Ros, J. Oxidative Stress Promotes Specific Protein Damage inSaccharomyces cerevisiae. *J. Biol. Chem.* **275,** 27393–27398 (2000).

151. Cooke, M. S., Evans, M. D., Dizdaroglu, M. & Lunec, J. Oxidative DNA damage: mechanisms, mutation, and disease. *FASEB J.* **17,** 1195–1214 (2003).

152. Sharma, P., Jha, A. B., Dubey, R. S. & Pessarakli, M. Reactive Oxygen Species, Oxidative Damage, and Antioxidative Defense Mechanism in Plants under Stressful Conditions. *J. Bot.* **2012,** e217037 (2012).

153. Moungjaroen, J. *et al.* Reactive Oxygen Species Mediate Caspase Activation and Apoptosis Induced by Lipoic Acid in Human Lung Epithelial Cancer Cells through Bcl-2 Down-Regulation. *J. Pharmacol. Exp. Ther.* **319,** 1062–1069 (2006).

154. Kongara, S. & Karantza, V. The interplay between autophagy and ROS in tumorigenesis. *Front. Oncol.* **2,** 171 (2012).

155. Du, J.-H., Zhang, H.-D., Ma, Z.-J. & Ji, K.-M. Artesunate induces oncosis-like cell death in vitro and has antitumor activity against pancreatic cancer xenografts in vivo. *Cancer Chemother. Pharmacol.* **65,** 895–902 (2010).

156. Ma, L. *et al.* Fluopsin C induces oncosis of human breast adenocarcinoma cells. *Acta Pharmacol. Sin.* **34,** 1093–1100 (2013).

157. Mone, A. P. *et al.* Hu1D10 induces apoptosis concurrent with activation of the AKT survival pathway in human chronic lymphocytic leukemia cells. *Blood* **103,** 1846–1854 (2004).

158. Bras, M. *et al.* Drp1 mediates caspase-independent type III cell death in normal and leukemic cells. *Mol. Cell. Biol.* **27,** 7073–7088 (2007).

159. Alinari, L. *et al.* Combination anti-CD74 (milatuzumab) and anti-CD20 (rituximab) monoclonal antibody therapy has in vitro and in vivo activity in mantle cell lymphoma. *Blood* **117,** 4530–4541 (2011).

160. Bellosillo, B. *et al.* Complement-mediated cell death induced by rituximab in B-cell lymphoproliferative disorders is mediated in vitro by a caspase-independent mechanism involving the generation of reactive oxygen species. *Blood* **98,** 2771–2777 (2001).

161. Han, Y. H. & Park, W. H. Tiron, a ROS scavenger, protects human lung cancer Calu-6 cells against antimycin A-induced cell death. *Oncol. Rep.* **21,** 253–261 (2009).

162. Yamada, J. *et al.* Cell permeable ROS scavengers, Tiron and Tempol, rescue PC12 cell death caused by pyrogallol or hypoxia/reoxygenation. *Neurosci. Res.* **45,** 1–8 (2003).

163. Taiwo, F. A. Mechanism of tiron as scavenger of superoxide ions and free electrons. *J. Spectrosc.* **22,** 491–498 (2008).

164. Novo, E. & Parola, M. Redox mechanisms in hepatic chronic wound healing and fibrogenesis. *Fibrogenesis Tissue Repair* **1,** 5 (2008).

165. Miyazawa, M. *et al.* The role of mitochondrial superoxide anion (O2(-)) on physiological aging in C57BL/6J mice. *J. Radiat. Res. (Tokyo)* **50,** 73–83 (2009).

166. Alduaij, W. *et al.* Novel type II anti-CD20 monoclonal antibody (GA101) evokes homotypic adhesion and actin-dependent, lysosome-mediated cell death in B-cell malignancies. *Blood* **117,** 4519–29 (2011).

167. Landmesser, U. *et al.* Oxidation of tetrahydrobiopterin leads to uncoupling of endothelial cell nitric oxide synthase in hypertension. *J. Clin. Invest.* **111,** 1201–1209 (2003).

168. Bedard, K. & Krause, K.-H. The NOX Family of ROS-Generating NADPH Oxidases: Physiology and Pathophysiology. *Physiol. Rev.* **87,** 245–313 (2007).

169. Vignais, P. V. The superoxide-generating NADPH oxidase: structural aspects and activation mechanism. *Cell. Mol. Life Sci. CMLS* **59,** 1428–1459 (2002).

170. Hordijk, P. L. Regulation of NADPH Oxidases The Role of Rac Proteins. *Circ. Res.* **98,** 453–462 (2006).

171. Bokoch, G. M., Quilliam, L. A., Bohl, B. P., Jesaitis, A. J. & Quinn, M. T. Inhibition of Rap1A binding to cytochrome b558 of NADPH oxidase by phosphorylation of Rap1A. *Science* **254,** 1794–1796 (1991).

172. Brandes, R. P. & Kreuzer, J. Vascular NADPH oxidases: molecular mechanisms of activation. *Cardiovasc. Res.* **65,** 16–27 (2005).

173. Wientjes, F. B., Hsuan, J. J., Totty, N. F. & Segal, A. W. p40phox, a third cytosolic component of the activation complex of the NADPH oxidase to contain src homology 3 domains. *Biochem. J.* **296 (Pt 3),** 557–561 (1993).

174. Matute, J. D., Arias, A. A., Dinauer, M. C. & Patiño, P. J. p40phox: The last NADPH oxidase subunit. *Blood Cells. Mol. Dis.* **35,** 291–302 (2005).

175. O'Donnell, B. V., Tew, D. G., Jones, O. T. & England, P. J. Studies on the inhibitory mechanism of iodonium compounds with special reference to neutrophil NADPH oxidase. *Biochem. J.* **290,** 41–49 (1993).

176. Krötz, F. *et al.* Mycophenolate acid inhibits endothelial NAD(P)H oxidase activity and superoxide formation by a Rac1-dependent mechanism. *Hypertension* **49,** 201–208 (2007).

177. Stolk, J., Hiltermann, T. J., Dijkman, J. H. & Verhoeven, A. J. Characteristics of the inhibition of NADPH oxidase activation in neutrophils by apocynin, a methoxy-substituted catechol. *Am. J. Respir. Cell Mol. Biol.* **11,** 95–102 (1994).

178. Düssmann, H., Kögel, D., Rehm, M. & Prehn, J. H. M. Mitochondrial Membrane Permeabilization and Superoxide Production during Apoptosis A SINGLE-CELL ANALYSIS. *J. Biol. Chem.* **278,** 12645–12649 (2003).

179. Majstoravich, S. *et al.* Lymphocyte microvilli are dynamic, actin-dependent structures that do not require Wiskott-Aldrich syndrome protein (WASp) for their morphology. *Blood* **104,** 1396–1403 (2004).

180. Juang, S. H., Carvajal, M. E., Whitney, M., Liu, Y. & Carraway, C. A. Tyrosine phosphorylation at the membrane-microfilament interface: a p185neu-associated signal transduction particle containing Src, Abl and phosphorylated p58, a membrane- and microfilament-associated retroviral gag-like protein. *Oncogene* **12,** 1033–1042 (1996).

181. Menco, B. P. M. The fine-structural distribution of G-protein receptor kinase 3, beta-arrestin-2, Ca2+/calmodulin-dependent protein kinase II and phosphodiesterase PDE1C2, and a Cl(-)-cotransporter in rodent olfactory epithelia. *J. Neurocytol.* **34,** 11–36 (2005).

182. Greicius, G. *et al.* Microvilli structures on B lymphocytes: inducible functional domains? *Int. Immunol.* **16,** 353–364 (2004).

183. Momose, H. *et al.* Dual phosphorylation of phosphoinositide 3-kinase adaptor Grb2-associated binder 2 is responsible for superoxide formation synergistically stimulated by Fc gamma and formyl-methionyl-leucyl-phenylalanine receptors in differentiated THP-1 cells. *J. Immunol. Baltim. Md 1950* **171,** 4227–4234 (2003).

184. Schiffmann, E., Corcoran, B. A. & Wahl, S. M. N-formylmethionyl peptides as chemoattractants for leucocytes. *Proc. Natl. Acad. Sci.* **72,** 1059–1062 (1975).

185. Tian, W. *et al.* FcγR-stimulated activation of the NADPH oxidase: phosphoinositide-binding protein p40phox regulates NADPH oxidase activity after enzyme assembly on the phagosome. *Blood* **112,** 3867–3877 (2008).

186. Mijares, A., Lebesgue, D., Wallukat, G. & Hoebeke, J. From agonist to antagonist: Fab fragments of an agonist-like monoclonal anti-beta(2)-

adrenoceptor antibody behave as antagonists. *Mol. Pharmacol.* **58,** 373–379 (2000).

187. Spaargaren, M., Defize, L. H., Boonstra, J. & Laat, S. W. de. Antibody-induced dimerization activates the epidermal growth factor receptor tyrosine kinase. *J. Biol. Chem.* **266,** 1733–1739 (1991).

188. Niederfellner, G. *et al.* Epitope characterization and crystal structure of GA101 provide insights into the molecular basis for type I/II distinction of CD20 antibodies. *Blood* **118,** 358–367 (2011).

189. Smith, K. R., Klei, L. R. & Barchowsky, A. Arsenite stimulates plasma membrane NADPH oxidase in vascular endothelial cells. *Am. J. Physiol. Lung Cell. Mol. Physiol.* **280,** L442–449 (2001).

190. Fisher, A. B. Redox Signaling Across Cell Membranes. *Antioxid. Redox Signal.* **11,** 1349–1356 (2009).

191. Bao, J.-X. *et al.* Lysosome-membrane fusion mediated superoxide production in hyperglycaemia-induced endothelial dysfunction. *PloS One* **7,** e30387 (2012).

192. Bao, J.-X. *et al.* Activation of membrane NADPH oxidase associated with lysosome-targeted acid sphingomyelinase in coronary endothelial cells. *Antioxid. Redox Signal.* **12,** 703–712 (2010).

193. Nohl, H. & Gille, L. Lysosomal ROS formation. *Redox Rep. Commun. Free Radic. Res.* **10,** 199–205 (2005).

194. Desnick, R. J. & Schuchman, E. H. Enzyme replacement and enhancement therapies: lessons from lysosomal disorders. *Nat. Rev. Genet.* **3,** 954–966 (2002).

195. Jäättelä, M. Multiple cell death pathways as regulators of tumour initiation and progression. *Oncogene* **23,** 2746–2756 (2004).

196. Kubota, C. *et al.* Constitutive Reactive Oxygen Species Generation from Autophagosome/Lysosome in Neuronal Oxidative Toxicity. *J. Biol. Chem.* **285,** 667–674 (2010).

197. Boya, P. & Kroemer, G. Lysosomal membrane permeabilization in cell death. *Oncogene* **27,** 6434–6451 (2008).

9 **APPENDIX**

At the time of submission of the thesis, a patent application has been filed,

PCT Application No.: PCT/SG2014/000570

Title: Cytotoxic Antibody

Inventors: Andre CHOO; ZHENG Jiyun

Applicant: A*STAR

ETPL ref: BTI/P/08104/01/PCT.

A manuscript titled “Excess reactive oxygen species production mediates monoclonal antibody induced human pluripotent stem cell death via oncosis” has been submitted to Cell Report and currently it is undergoing review.